UNIVERSITY
OF OSLO

Jon Arthur Borgersen

Intrinsic defect dependent resistivity in semiconducting oxides

Thesis submitted in partial fulfilment of the requirements for the degree of Philosophiae Doctor

Department of Physics
Faculty of Mathematics and Natural Sciences

2023

Series of dissertations submitted to the
Faculty of Mathematics and Natural Sciences, University of Oslo
No. 2626

ISSN 1501-7710

Cover: UiO.
Print production: Graphic Center, University of Oslo.

Sammendrag

Halvledende oksider med brede båndgap er en materialklasse der materialene kan ha elektrisk konduktivitet på størrelsesorden $10^3\,\mathrm{S/cm}$ og samtidig være $\geq 80\,\%$ gjennomsiktige for synlig lys. Denne svært uvanlige kombinasjonen av egenskaper gjør disse materialene uunværlige i en rekke elektroniske anvendelser, slik som for eksempel flatskjermer. I slike skjermer har materialer basert på indiumoksid (In_2O_3) lenge vært industristandard. Andre alternativer, slik som sinkoksid (ZnO), har blitt utforsket men In_2O_3-baserte materialer er fremdeles ledende. Selv om elektronikkindustrien har opparbeidet en imponerende kompetanse på å finjustere egenskapene til de halvledende oksidene til det aktuelle bruksområdet mangler det fremdeles kunnskap om hvordan disse materialene oppfører seg på atomær skala. Det har lenge vært kjent at at intrinsiske defekter i atomstrukturen har stor innvirkning på de elektriske materialegenskapene, men eksakt hvilke defekter som gir signifikante bidrag, og hvordan de interagerer er fremdeles ikke fullstendig forstått.

Arbeidet som presenteres i denne avhandlingen er et bidrag til å fylle dette kunnskapshullet for halvledende oksider gjenerelt, med spesielt fokus på In_2O_3. Fremgangsmåten er eksperimentell, og baserer seg på ionebestråling for å modifisere defektkonsentrasjonen mens de elektriske egenskapene i hovedsak karakteriseres med strøm-spenningsmålinger og Hall effekt-målinger.

En tidlig oppdagelse var, som allerede antatt, at ulike materialer har svært ulik respons på ionebestråling. Som eksempel har resistiviteten til In_2O_3 en relativt kompleks, tre-trinns, relasjon til stråledosen. På de laveste dosene synker resistansen, før den øker brått når dosen blir høyere. På ennå høyere doser synker resistansen igjen, og den ser ikke ut til å stabilisere seg innenfor det målte doseområdet (opp til $10^{17}\,\mathrm{cm^{-2}}$). Dette er i sterk kontrast til, for eksempel, galliumoksid (Ga_2O_3) der resistansen øker proporsjonalt med dosen allerede fra den laveste bestrålingsdosen. Etter en dose på $3 \times 10^{13}\,\mathrm{cm^{-2}}$ overgår resistansen måleområdet til instrumenteringen, og den forblir umålbart høy gjennom resten av doseområdet. Sinkoksid viser seg å oppføre seg kvalitativt likt som In_2O_3 mens tinnoksid (SnO_2) oppfører seg mer som Ga_2O_3.

Til tross for disse meget ulike responsene har vi greid å utvikle en universell modell som kan forklare den doseavhengige resistansutviklingen. Kvalitativt består modellen av tre deler, en for hvert trinn av restistansutviklingen beskrevet for In_2O_3 over. Den initielle nedgangen i resistans kan forklares med modifikasjoner i materialoverflaten. En sammenligning mellom effektene av ionebestråling og bestråling med ultraviolett (UV) lys indikerer at ionebestrålingen forårsaker desorpsjon av adsorberte oksygenrelaterte urenheter. Dette fører til at energibåndene bøyes nedover i overflateregionen og resulterer i akkumulasjon av elektroner nær overflaten. Årsaken til at en lignende resistansreduksjon ikke

observeres i Ga_2O_3 antas å være at overflatetilstandene til dette materialet ikke gir en negativ båndbøying når overflaten er ren [1].

Når dosen økes vil signifikante konsentrasjoner av Frenkelpar dannes i både anion- og kationgitteret. Avhengig av netto ladningstilstand for Frenkelparene på det gjeldende Ferminivået kan dette øke eller minke resistiviteten, eller låse den på et Ferminivå som korresponderer med enkelte ladningsnivåer. Videre bestråling øker sannsynligheten for å danne en defekt i umiddelbar nærhet av en allerede eksisterende defekt. Dermed kan defektkomplekser dannes uten å kreve diffusjon av punktdefektene. Avhengig av netto ladningstilstand for kompleksene relativt til de individuelle punktdefektene kan dette igjen gjøre at resistiviteten øker eller minker inntil, Ferminivået igjen låses på et nytt energinivå.

For å vurdere den relative viktigheten av atomstruktur versus grunnstoffsammensetning på resistivitetens defektavhengighet ble Ga_2O_3 legert inn i In_2O_3 i konsentrasjoner opp til 17.8 %. Før bestråling hadde alle prøvene bixbyittstruktur som forventet for In_2O_3. Etter bestråling som beskrevet over ble det funnet at atomstrukturen var bevart, og elektrisk sett oppførte alle prøvene seg kvalitativt som ren In_2O_3. Dette indikerer at atomstrukturen har et signifikant bidrag, og oppfordrer til videre arbeid på legeringer med høyere Ga_2O_3-konsentrasjoner.

Det primære resultatet av dette arbeidet er en sammenhengende teori for de detaljerte mekanismene bak defektkonsentrasjonsavhengig resistivitet i In_2O_3. Videre er modellen generell, og kan anvendes på alle halvledere der energinivåene til de mest stabile defektene er kjent. Den utviklede teorien kan forhåpentligvis være av nytte for forskning og utvikling av materialer beregnet på strålingsintensive miljøer.

Abstract

The wide band gap semiconducting oxides is a class of materials which can exhibit electrical conductivities on the order of 10^3 S/cm while at the same time being $\geq 80\,\%$ transparent to visible light. This highly unusual combination of properties makes these materials indispensable for a multitude of electronic devices, perhaps most notably the flat panel displays. In such a display, indium oxide (In_2O_3) based materials have been, and continue to be, the industry standard, while other alternatives such as zinc oxide (ZnO) have also been explored. Although the electronics industry has great technological competence in tuning the properties of the semiconducting oxides to suit their particular needs, there is still a lack of knowledge regarding how these materials behave on the atomic scale. While it is well established that intrinsic defects in the atomic structure greatly affect the electrical material properties, exactly which defects are contributing, and how they interact, is still not fully understood.

The presented work serves as a step towards filling this knowledge gap for the semiconducting oxides in general, and for In_2O_3 in particular. The overarching topic encompasses the effect of intrinsic defects on the electrical properties of this class of materials. The approach is experimental, and relies on ion irradiation to control the defect concentration, while the impact on the electrical properties is characterized mainly by current-voltage- and Hall-effect measurements.

An early discovery was, as already anticipated, that different materials have vastly different responses to identical ion irradiation exposures. As an example, the resistivity of In_2O_3 shows a relatively complex, three-staged, relation with the irradiation dose. At the lowest doses, the measured resistance decreases, before increasing sharply as the dose is increased. At the highest doses, the resistance is again found to decrease, and does not seem to stabilize for the employed dose range (up to $10^{17}\,\mathrm{cm}^{-2}$). In contrast, gallium oxide (Ga_2O_3) appears to have a considerably simpler resistance variation with dose. In this material, the resistance is found to increase proportionally with the dose already from the first stage of the irradiation. After a dose of $3 \times 10^{13}\,\mathrm{cm}^{-2}$ the resistance is beyond the measurement range of our instrumentation, and it remains immeasurably high for the remainder of the dose range. During the material screening stage of the project, it was found that ZnO behaves qualitatively like In_2O_3, while tin oxide (SnO_2) behaves more like Ga_2O_3.

Despite the dramatically different responses, a universal model applicable to all the measured samples has been developed. Qualitatively the model is composed of three parts, one for each stage of the resistance evolution described for In_2O_3 above. Using this material as an example, it is found that the initial decrease in resistance can be explained by ion beam induced modifications of the sample surface. Comparative studies of ion irradiation and UV-light exposures

indicate that the ion beam cleans the sample surface from adsorbed oxygen related species. The electrical effect of this surface modification is to decrease the resistivity, correlating with a recovery of the native downward surface band bending and the surface electron accumulation layer of In_2O_3. The reason why no corresponding decrease in resistivity is observed at low doses in e.g. Ga_2O_3 is believed to be that the native surface states of this material do not cause a downward band bending [1].

As the dose is increased, appreciable concentrations of Frenkel pairs are generated at both the anion and cation sublattices. Depending on the net charge state of the Frenkel pairs at the current Fermi level, this can shift the resistivity up or down, or even pin it at Fermi levels corresponding to certain charge transition levels. Further irradiation increases the probability of forming a defect in the immediate vicinity of an already existing defect. Hence, complexes between the independent point defects can form without the need for diffusion. Depending then on the net charge state of the complexes relative to the individual point defects, the resistivity can be shifted up or down until the Fermi level is again ultimately pinned at some new charge transition level.

To assess the relative importance of elemental composition versus atomic structure on the defect dependent resistivity, Ga_2O_3 was alloyed into In_2O_3 in concentrations up to 17.8 % and the samples were exposed to ion irradiation as described above. As-grown, all samples had the bixbyite In_2O_3 structure, and no signs of phase changes were observed after irradiation. The electrical characterization showed that all the samples behaved qualitatively similar to pure In_2O_3, indicating that the structure indeed plays a significant role.

The primary outcome of this work is thus a compelling theory for the detailed mechanism behind the defect dependent resistivity in In_2O_3. Moreover, the model is general and can be applied to any semiconductor for which the charge transition levels of the most stable defects is available. As such, the presented theory may prove valuable for device technologies intended for radiation hard environments.

Acknowledgements

The work presented in this thesis has, of course, not been a one man project. Rather, it is the result of a collaboration with a group of people to which I am forever grateful.

First off I would like to express my sincere gratitude to my supervisors Prof. Andrej Kuznetsov, Dr. Klaus Magnus Johansen and Dr. Helge Kristiansen, and Prof. Lasse Vines who, more or less voluntarily, got pulled in along the way. In no way would this thesis have been completed if it was not for your combined experience, analytical skills and positive attitude. Other people instrumental to the completion of this work include the co-authors of the appended research papers, whom I would like thank collectively for their indispensable assistance with both theoretical calculations, experimental work and data analysis.

Further I would like to thank the MiNaLab engineering team, Viktor Bobal, Christoph Seiffert and Halvor Dolva, both for keeping the lab and all its equipment running smoothly, and for their experimental assistance. A special thanks goes to Viktor for always keeping cheerful during late evenings on the implanter. On the topic of cheerfulness, I would also like to thank all my past and present colleagues at the LENS group and center for materials science and nanotechnology for making both the office and the labs very enjoyable places to work and socialize.

During my PhD project I have had the pleasure of visiting Prof. Yicheng Lu's group at Rutgers University and Prof. Holger von Wenckstern's group at Universität Leipzig. I thoroughly enjoyed my stays at both of these institutions and would like to thank said professors and their group members for their generous hospitality.

From the world outside academia I would like to thank all my friends, in particular Mikal Gravdal and Geir Sørmoen, for pulling my mind off from work from time to time. It is indeed hugely appreciated.

Last but not least I would like to thank my family for their constant love, support and encouragement throughout all my years if studying. It would not have been possible without you!

Jon Arthur Borgersen
Oslo, February 2023

List of publications

Appended papers

The following papers constitute the foundation of this thesis and can be found in the appendix.

1. J. Borgersen, L. Vines, Y. K. Frodason, A. Kuznetsov, H. von Wenckstern, M. Grundmann, M. Allen, J. Zúñiga-Pérez, K. M. Johansen, *Experimental exploration of the amphoteric defect model by cryogenic ion irradiation of a range of wide band gap oxide materials*, Journal of Physics: Condensed Matter **22**, 415704 (2020)

2. J. Borgersen, K. M. Johansen, L. Vines, H. von Wenckstern, M. Grundmann, A. Yu. Kuznetsov, *Fermi level controlled point defect balance in ion irradiated indium oxide*, Journal of Applied Physics **130**, 085703 (2021)

3. J. Borgersen, R. Karsthof, V. Rønning, L. Vines, H. von Wenckstern, M. Grundmann, A. Yu. Kuznetsov, K. M. Johansen, *Origin of enhanced conductivity in low dose ion irradiated oxides*, AIP Advances **13**, 015211 (2023)

4. J. Borgersen, R. Karsthof, L. Vines, A. Yu. Kuznetsov, H. von Wenckstern, K. M. Johansen, *Effect of the Ga concentration on the defect concentration dependent resistivity in ion irradiated $(InGa)_2O_3$ alloys*, Manuscript under preparation

Papers not appended

In addition to the works above, contributions have also been made to the following papers but these will not be discussed in the following.

1. V. S. Olsen, V. Øversjøen, D. Gogova, B. Pécz, A. Galeckas, J. Borgersen, K. Karlsen, L. Vines, A. Kuznetsov, *$ZnSnN_2$ in real space and k-space: Lattice constants, dislocation density, and optical band gap*, Advanced Optical Materials, **9**, 2100015 (2021)

2. J. N. Kvalvik, J. Borgersen, P.-A. Hansen, O. Nilsen, *Area-selective atomic layer deposition of molybdenum oxide*, Journal of Vacuum Science & Technology A, **38**, 042406 (2020)

3. L.-P. Ho, M. Younas, J. Borgersen, R. T. A. Khan, S. J. Rezvani, S. Pallastri, M. J. Akhtar, M. Nadeem, D. Huang, Y.-L. Shi, A. Kuznetsov, F. C.-C. Ling, *Photoluminescence intensity of Cu-doped ZnO modulated via defect occupancy by applying electric bias*, Journal of Physics D: Applied Physics, **55**, 315102 (2022)

Contents

Chapter 1

Introduction

The wide band gap semiconducting oxides is a class of materials which allows simultaneous transparency to visible light and tunable electrical conductivity. Depending on the particular material, and its processing, achievable conductivities range from practically insulating up to as high as $\sim 10^4$ S/cm [2, p. 3]. Examples of materials from this class, which are either used in commercial applications today or intensively researched for future devices, include indium oxide (In_2O_3), tin oxide (SnO_2), gallium oxide (Ga_2O_3) and zinc oxide (ZnO). When these materials are processed to maximize their electrical conductivity they are often referred to as transparent conductive oxides (TCOs), whereas when their semiconducting properties are emphasized the term transparent semiconducting oxide (TSO) is used.

In a historical perspective, perhaps the first known practical application of TCOs was as resistive windshield defrosters in World War II airplanes [3]. The windshield could be coated with a TCO, typically SnO_2, through which a small electrical current was passed. The resulting Ohmic heating ensured that the windshield did not freeze when flying at high altitudes. Today tin doped In_2O_3 (ITO) is used instead of SnO_2 for this application, as the higher conductivity of ITO allows larger windows to be defrosted with a relatively low voltage. As a more mundane example, the same technology has also been used to avoid condensation of water vapour on the glass doors of e.g. supermarket freezers [4, p. 3].

Today's applications of the TCOs are critical in low-emissivity windows, transparent electrodes for liquid crystal displays (LCDs) and certain solar cell technologies [5, 6]. In low-emissivity windows the free electrons of the TCO reflect IR wavelengths from the sun, preventing them from heating the interior of the building and thereby reducing the need for air conditioning in warmer climates. At the same time, heat radiating from the interior is unable to escape out of the building, thus reducing the need for heating in colder environments [3]. In solar cell architectures such as silicon heterojunctions, CIGS, CdTe and perovskites, the use of TCO electrodes reduce or eliminate the need for metallic electrodes. By reducing the area covered by opaque metal electrodes, the illuminated fraction of the cell surface increases, thereby increasing the efficiency [6]. During the last couple of decades, the liquid crystal display market has exploded, with an incredible development of smartphones, televisions and computer screens, smart watches, etc. All LCDs require at least one, usually two, transparent electrodes to manipulate the liquid crystals and thereby generate the desired picture. ITO was for a long time the material of choice for this application due to its high conductivity and transparency. More recently, zinc doped In_2O_3 (IZO) has gained attraction due to its possibility for room temperature deposition,

easier patterning and improved thermal stability [4]. At the time of writing, organic light emitting diode (OLED) displays are competing with the LCDs for dominance in the flat panel display market. These displays also require a transparent electrode, and again doped In_2O_3 is the prime candidate [7]. Other applications of the TCO/TSO materials are in transparent and/or flexible electronics and displays, building integrated solar cells, various types of sensor systems, and high power electronics [8–11]. For the latter example, Ga_2O_3 is particularly interesting, as its wide band gap of $\sim 4.8\,\mathrm{eV}$ provides significantly higher breakdown field strength than that of the competing technologies [11]. The wide band gap also makes this material suitable for solar-blind ultraviolet radiation detectors, with applications in communication and detection systems. Further, Ga_2O_3 is both thermally and chemically stable making it interesting for use in harsh environments.

A single material being both transparent and electrically conductive is seemingly a paradox. The cause of this highly unusual combination of properties is the wide band gap which makes the material transparent to visible light, combined with a high concentration of defects in the crystal structure which provides the charge carriers necessary for the electrical conduction. Such defects can be intentionally or unintentionally introduced, and can be intrinsic or extrinsic to the semiconductor in question. It is well established that extrinsic doping on the cation sublattice is a viable way of altering the carrier concentration. Impurities of higher valence, e.g. tin in In_2O_3, will act as donors [12] while impurities of lower valence, e.g. magnesium in In_2O_3, will act as acceptors [13]. Extrinsic donor doping with tin or zinc, respectively, is the approach used when producing ITO and IZO electrodes and is well understood.

Despite decades of research, which defects are responsible for the conductivity in nominally undoped TSOs is, however, not universally determined. The oxygen vacancy is often presented as a likely contributor but, for example in ZnO, oxygen vacancies are deep donors which cannot explain the experimentally observed carrier concentrations [14]. Cation self interstitials represent another candidate, but may be excessively diffusive for appreciable contribution to the carrier concentration [15]. A related issue which has been under intense scrutiny for many years is the observed unipolar conduction of the wide band gap oxides. Most of these materials, of which ZnO is perhaps the prime example, are readily doped n-type, while achieving stable p-type conduction is seemingly impossible [16]. Other TSOs, e.g. NiO and Cu_2O are readily doped p-type but n-type doping has not been achieved to date [4, pp. 40–43] [17, 18]. Although still not universally understood, some criteria for n- or p-type dopability have been established [19]. This unipolar conduction is in strong contrast to other commonly used electronic materials like silicon and gallium arsenide, and is one of the main obstacles to overcome before fabrication of CMOS devices and homojunction photovoltaics in wide band gap oxides can be realized.

Research on the transparent oxides proceeds through both experimental and theoretical routes, each with their own set of intricacies. Some TSOs, e.g. In_2O_3, have complex crystal structures with many atoms in their unit cell which makes reliable theoretical predictions of their defect properties numerically

challenging. As an example, even qualitatively determining whether the oxygen vacancy in indium oxide is a deep or shallow donor, let alone quantitatively pinpointing its energy levels, is far from straightforward [20]. Recent hybrid calculations appears to have reached consensus that it is indeed shallow [21–23]. Other TSOs, e.g. Ga_2O_3, have several inequivalent lattice- and interstitial sites, significantly increasing the number of possible defect configurations and hence the computational cost.

On the experimental side, spectroscopic characterization of the defect levels may pose a challenge in the TSOs. Again using In_2O_3 as an example, its surface electron accumulation layer (SEAL) prevents the formation of rectifying contacts and thus capacitive techniques on undoped material are not available unless special measures are taken to mitigate the SEAL [24, 25]. Various luminescence techniques are possible, but tend to only yield wide bands which are difficult to deconvolute into distinct transition levels [26–28]. Hence, for In_2O_3 no comprehensive experimental verification of the theoretically calculated thermodynamic defect transition levels are available in the literature.

A frequently applied model for explaining defect behaviour in wide band gap semiconductors is the amphoteric defect model (ADM), described in Section 2.3. One of the objectives of the presented work was to test the predictions of the ADM for a range of wide band gap oxides. Several features of our experimental results were not predicted by the model, and an extended model was developed in Paper I to incorporate these features. Further, within the framework of this extended ADM the results presented in Paper II correlates well with recent theoretical defect charge state transition levels for point defects and antisites. In this paper we also extract the dynamic annealing rate, i.e. the rate at which defects anneal out of the atomic structure in-situ, for In_2O_3 under heavy ion irradiation at a temperature of 50 K. Paper III covers the use of ion irradiation for modifying the surface properties of In_2O_3, and the effect of the resulting downward surface band bending on the resistivity evolution. In Paper IV the effect of alloying Ga_2O_3 into bixbyite In_2O_3 is examined. In general, the presented results can serve as predictions of the radiation tolerance of various TSOs, with practical applications in device development for radiation hard environments.

In the following text, Chapters 2 and 3 establish the theoretical framework on which the thesis is based. Chapter 4 presents the experimental and theoretical methods utilized in the work, while Chapter 5 summarizes the obtained results and their interpretation. Further, in Chapter 6, conclusions and suggestions for further work are presented. The data are presented in more detail in the appended papers.

Chapter 2

Semiconductor physics

This chapter presents a brief summary of the key concepts of semiconductor physics forming the basis of this thesis. Section 2.1 covers the physical structure of materials while Section 2.2 introduces the electrical properties. These sections are largely based on the textbooks by Ashcroft and Mermin [29], Kittel [30], Streetman and Banerjee [31] and Tilley [32]. Concluding the chapter, Section 2.3 presents a widely used model for defects in semiconductors, namely the amphoteric defect model (ADM).

2.1 Structural properties

Consider assembling a group of individual atoms into a slab of solid matter. The preferred position of each atom relative to its neighbours is that which minimizes its potential energy, and is dictated by the chemical nature of the atoms, the temperature and the pressure [32, p. 152]. Under favourable synthesis conditions, this trend to minimize energy makes the atoms settle into well defined positions. Such materials, where the atomic structure exhibit long-range order, are called single crystals. In the opposite case, where the atoms are not allowed sufficient time to settle in their preferred positions during synthesis, they will occupy random positions in the solid and the material is called amorphous. An intermediate between these two extremes is the polycrystalline phase, were crystalline regions called grains are separated by grain boundaries. Due to the long range order of the crystalline materials, the relative positions of their atoms can be quantitatively determined, comprising the crystal lattice. For multicomponent materials it is common to define a separate sublattice for each element.

Thermodynamically, the perfect crystal with all the lattice sites occupied is not achievable due to entropy. In addition, perfect crystals without impurities are not achievable in practice. Empty lattice sites, occupied non-lattice sites and intentionally or unintentionally introduced foreign atoms are known as *point defects*, and can significantly affect the physical, optical, and electrical properties of the material. As illustrated in Figure 2.1 a lattice site where the associated atom is missing is called a vacancy. An atom located in-between lattice sites is called an interstitial, and if this atom is native to the material it is called a self-interstitial. Impurities in the crystal can occupy either interstitial, or substitutional positions with respect to the lattice sites. An important term which will be extensively used throughout this thesis is the Frenkel pair, referring to a combination of one vacancy and one interstitial from the same sublattice. It should be noted that while the term defect usually has negative connotations in

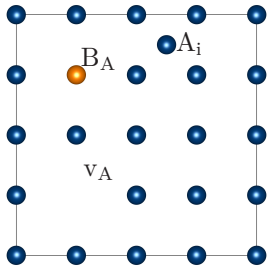

Figure 2.1: Point defects in a two dimensional crystalline material consisting of atoms A. V_A is a vacancy, A_i an interstitial and B_A a substitutional impurity of element B. Illustration prepared using the VESTA software [33].

everyday speech, defects in semiconductors can equally well be desirable features [34]. Indeed, intentionally introducing impurities is the most common way of tuning the electrical properties of a semiconductor, and is referred to as doping.

If two or more primary defects exist in close proximity to each other, they can form complexes or extended defects. An example of a complex is the divacancy formed when two vacancies occupy neighbouring lattice sites. Common extended defects include screw- and edge dislocations where planes of atoms are partially displaced with respect to each other [32, pp. 79–85]. The grain boundaries in polycrystalline materials and even the outer surfaces of a material sample can also be considered as extended defects.

2.2 Electrical properties

Let us now return to the thought experiment from the start of Section 2.1 where a crystalline solid was assembled from individual atoms, but this time focusing on the electronic properties of the material and assuming that the temperature is 0 K. It is well known from quantum mechanics that the electrons of a single atom only can occupy discrete energy levels [35, p. 214]. When two atoms combine into a molecule, each energy level of the individual atoms splits into two new levels, one with a lower energy than the original level and one with a higher energy. If a third atom is added, the levels split again, and now three levels are available for each of the original levels. Continuing this process until a solid of N atoms is created causes each of the original energy levels have split into N levels for the solid [31, p. 66]. For certain energy ranges these levels are so tightly grouped that they form a virtual continuum of states called an energy band, while at other energies no states are available. The electrons of the solid preferentially occupy the lowest available energy band hence the lowest energy bands will be filled with electrons, while the bands at higher energies will be empty.

On an energy scale, the two bands of importance for the electrical properties are the highest fully occupied band and the band next higher in energy. For the semiconductors these bands are referred to as the valence band (VB) and conduction band (CB), respectively. At $T = 0\,\mathrm{K}$ there are no electrons in the conduction band and no free states in the valence band, hence no charge can be transported by an electric field and the material is electrically insulating. As the temperature is increased, electrons can be excited to the CB from the VB (if the band gap is sufficiently narrow) or from defect or dopant states in the vicinity of the CB edge, and the material becomes electrically conductive.

For completeness it should be noted that the state left empty in the valence band when an electron transitions to the conduction band is called a hole. Materials which have been doped in such a way that the concentration of holes exceeds that of electrons are called p-type semiconductors, while ones where the electron concentration is greater are called n-type. Following this naming convention it is common to simply refer to the electron concentration as n and the hole concentration as p. The work presented in this thesis has been performed on n-type materials, hence hole conduction will be neglected in the following. The following subsections introduces the physics governing electrical conduction in semiconductors.

2.2.1 Density of states

Returning once again to the slab of solid material assembled from single atoms, assume now that the material is a crystalline, n-type, semiconductor. In order to determine the electrical properties of this material it is necessary to know how many states are available for electrons in the conduction band per unit volume in the material, the so called density of states. From here on, only electrons in the conduction band will be considered, while the valence electrons will be neglected. Due to the regular arrangement of the atoms, electrons experience a periodic potential as they move through the material. Under the simplification that the electrons do not interact with each other, it can be shown that the wavefunction $\psi_{\mathbf{k}}(r)$ of each electron can be represented by a plane wave multiplied with a periodic function

$$\psi_{\mathbf{k}}(r) = e^{i\mathbf{k}\cdot\mathbf{r}} u_{\mathbf{k}}(\mathbf{r}) \tag{2.1}$$

where $\mathbf{r}$ and $\mathbf{k}$ are the electron's position in real-space and its propagation constant, respectively [29, p. 133]. It follows that the magnitude of the momentum p of an electron is given by

$$p = \hbar k \tag{2.2}$$

where $\hbar$ is the reduced Planck's constant [31, p. 77]. Further, the energy of an electron is given by

$$E = E_c + \frac{p}{2m^*} = E_c + \frac{\hbar^2 k^2}{2m^*} \tag{2.3}$$

with E_c being the energy of the conduction band minimum (CBM) and m^* the effective mass of the electron in the conduction band. The effective mass is a scaling factor to the electron rest mass, which accounts for the electron's interactions with the material. By replacing the rest mass with the effective mass, the electrons can be treated as free particles. From Equation (2.3)

$$m^* = \frac{\hbar^2}{d^2E/dk^2} \tag{2.4}$$

showing that the effective mass is inversely proportional to the curvature of the conduction band. From Equation (2.3) it is also seen that the electron energy is parabolic in k, implying that m^* is constant. This typically holds for energies close to E_c, but at higher energies electron-electron interactions may become sufficiently strong to break the parabolicity.

One way of describing a non-parabolic conduction band is by relating the electron momentum to its velocity (v) [36]

$$p = \hbar k = m^* v \tag{2.5}$$

where

$$v = dE/dp = \frac{1}{\hbar}\frac{dE}{dk} \tag{2.6}$$

from which it follows that the effective mass can be expressed as

$$m^* = \frac{\hbar^2 k}{dE/dk}. \tag{2.7}$$

Here it should be noted that inserting the energy from Equation (2.3) into Equation (2.7) reproduces the constant effective mass of Equation (2.4).

Following Kane [37], the energy of an electron in a non-parabolic conduction band is given by

$$\frac{\hbar^2 k^2}{2m_0^*} = E + CE^2, \tag{2.8}$$

where m_0^* is the effective mass at the bottom of the conduction band and C is a constant describing the degree of non-parabolicity of the band. From this relation, the effective mass can be expressed explicitly as a function of the carrier concentration

$$m^*(n) = \sqrt{{m_0^*}^2 + 2C\hbar^2 m_0^* (3\pi^2 n)^{2/3}} \tag{2.9}$$

as shown in detail in [38]. For In_2O_3, $m_0^* = 0.18\,m_e$ and $C = 0.5\,eV^{-1}$ have been found to give a good correlation with experimental data [39], hence these values have been adopted in the present work.

Assuming the effective mass is known, applying Equation (2.3) for 3 dimensional materials it can be shown that the density of states is given by

$$g(E) = \frac{\sqrt{2}}{\pi^2} \left(\frac{m^*}{\hbar^2} \right)^{3/2} \sqrt{E}. \tag{2.10}$$

Another parameter needed to quantify the electron concentration, and subsequently the electrical properties, is the occupation probability of the available states. This is the topic of the next subsection.

2.2.2 The Fermi level

Being fermions, electrons occupy the states available to them with probabilities given by the Fermi-Dirac distribution function

$$f(E,T) = \frac{1}{e^{\frac{E-E_F}{kT}} + 1} \tag{2.11}$$

where E, E_F, k and T are the energy, the Fermi level, Boltzmann's constant and the temperature, respectively [31, pp. 86–88]. At $T = 0\,\mathrm{K}$ the Fermi-Dirac distribution is a step-like function, while at finite temperatures the step turns into a gradient with a slope inversely proportional to T. The Fermi level refers to the energy where $f(E,T) = 1/2$, i.e. the occupation probability is 50%.

2.2.3 Carrier concentrations

Using the density of states and the Fermi-Dirac distribution, the electron concentration can be calculated as

$$n = \int_0^\infty g(E) f(E,T) dE, \tag{2.12}$$

where the energies are referred to the bottom of the conduction band [31, p. 89]. Strictly speaking the upper limit of the integral should be the top of the conduction band. However, this energy is generally not known, and the Fermi-Dirac distribution becomes negligibly small at high energies so integrating to infinity is a common simplification. In practice, the exact solution of Equation (2.12) may be complicated, but a multitude of approximations are available, see for instance [31, p. 90][40, 41]

With today's computers solving Equation (2.12) numerically without approximations is, however, straightforward [42] and this approach has been used throughout the presented work.

2.2.4 Other electrical properties

The mobility (μ) of charge carriers in a material is a measure of their ability to drift in an electric field. Common limiting factors of the mobility include carrier collision events with ionized impurities, phonons and grain boundaries. The mobility can be expressed in different ways, e.g. in terms of the mean free time, τ, between the corresponding collisions. In these terms

$$\mu = q\tau/m^*. \tag{2.13}$$

Knowing the mobility and the carrier concentration, the conductivity is in general given by

$$\sigma = qn\mu_n + qp\mu_p \tag{2.14}$$

where the subscripts on the mobilities denote the corresponding type of charge carrier. In materials where the concentration of one carrier type is significantly higher than that of the other, only the respective half of the equation is relevant.

In this work, the ability of a material to conduct current will be represented by its resistivity $\rho = 1/\sigma$. The resistivity along with the sample dimensions dictates the resistance, R, of the sample

$$R = \rho L/A \tag{2.15}$$

where L and A are the length and the cross sectional area of the conducting layer, respectively.

From Ohm's law

$$R = \frac{V}{I}, \tag{2.16}$$

hence the resistance can also be calculated from the experimentally measurable voltage V and current I.

2.2.5 Defect charge states

The explanation above with allowed energy states comprising energy bands and no states in the band gap is only valid for a perfect crystal. As mentioned in Section 2.1, perfect crystals are not achievable in practice and, due to entropy, some concentration of unintentional intrinsic and extrinsic defects is always present. Consider forming a Frenkel pair from an atom (A) on a lattice site (A_A). If the atom brings all its valence electrons to an interstitial site both the interstitial, A_i, and the resulting vacancy, V_A, have the same electrical charge as in the perfect crystal and are said to be in a neutral charge state. In addition, the vacancy and interstitial generally have the possibility to donate or accept additional electrons to/from the conduction/valence band, resulting in the existence of several possible charge states for each defect. Which of these charge states has the lowest formation energy, and consequently is most widely adopted by the defect population, depends on the Fermi level of the material. At low Fermi levels it is favourable to donate electrons, giving the defect a positive charge. As the Fermi level increases this is less favourable and the defect is neutral. At even higher Fermi levels it is favourable to accept more electrons than in the neutral configuration, and the defect may take a negative charge state.

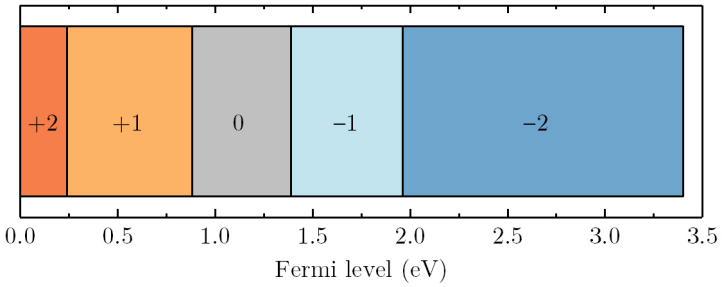

Figure 2.2: Schematic illustration of the charge states of the zinc vacancy in ZnO as a function of Fermi level. The energy scale starts at the VBM and the charge states were sourced from [43].

As an example, the charge states and their charge transition levels (CTLs) of the zinc vacancy in ZnO, as calculated in [43], are illustrated schematically in Figure 2.2. It is seen that several transition levels exist in the band gap and depending on the position of the Fermi level relative to these CTLs, the defect can act either as a donor or an acceptor. Defect species exhibiting this bipolar ability are called amphoteric defects. In addition to the intrinsic defects, intentional and unintentional impurities can also introduce discrete states in the band gap.

2.3 The amphoteric defect model

The amphoteric defect model (ADM) introduced by Walukiewicz in the 1980s [44–46] is based on the description of defects given in the previous subsection, and is a widely employed model of defect behaviour in semiconductors. Its key prediction is that a material specific energy level called the Fermi stabilization energy or charge neutrality level (CNL) can be determined for all semiconductors. This level lies at the energy where the formation energy of the most prominent donor(s) equals that of the most prominent acceptor(s), and thus has the property that it determines the net polarity of the preferentially forming defect species. If the Fermi level of the material lies below the CNL donor-like defects preferentially form, whereas if the Fermi level is above the CNL acceptor formation tend to be favoured. This implies that if defects are formed, the Fermi level will be shifted towards the CNL and ultimately be pinned at this value. From then on, further introduction of intrinsic defects will not cause any change in the Fermi level. In most semiconductors (e.g. Si, Ge and most of the III–Vs) the CNL is located close to the middle of the fundamental band gap. For such materials, n-type samples will favour acceptor generation while p-type samples favour donor generation. For either polarity, such defect generation will therefore shift the Fermi level towards midgap, resulting in a decreased carrier concentration and increased resistivity. This situation is illustrated in Figure 2.3 (a). A strongly contrasting situation is found in other materials such as e.g. InN, In_2O_3, SnO_2 and ZnO. Here, the CNL is located above the conduction band minimum as

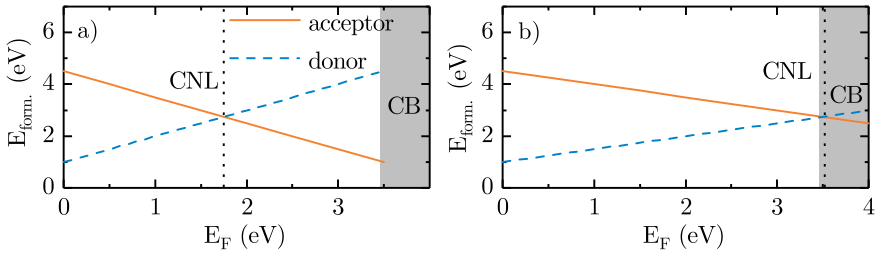

Figure 2.3: (a) The most prominent donor and acceptor in a conventional semiconductor (such as e.g. silicon) pins the charge neutrality level close to midgap. (b) In some materials the defect states pin the charge neutrality level above the CBM. The legend applies to both panels.

shown schematically in Figure 2.3 (b). In this case generated defects will tend to be donors, even for Fermi levels high in the band gap, enabling very high carrier concentrations and low resistivities to be reached.

A complementary view of the CNL is that CNL $= (\overline{E}_c + \overline{E}_v)/2$ where $\overline{E}_c$ and $\overline{E}_v$ are the conduction and valence band edges averaged over the Brillouin zone, respectively, i.e. the CNL lies at the Brillouin zone averaged midgap energy [47]. A good introduction to this interpretation is given in [48]. This perspective shows that materials with relatively flat valence and conduction bands will have the CNL close to the middle of the fundamental band gap, whereas materials with a flat valence band and dispersive conduction band can have the CNL above the CBM.

The CNL has been used to explain a multitude of experimentally observed and theoretically calculated phenomena such as defect generation [45], band alignment and Schottky barrier formation [48–50], doping limits [19, 51], the energy of the hydrogen $(+/-)$ charge transition level [52, 53] and the accumulation or depletion of electrons at material surfaces [54]. The CNL has also been used to explain experimentally observed changes in the electrical properties of semiconductors caused by ion irradiation [45]. Other studies, however, finds results conflicting with the predictions of the ADM [55, 56] and it appears that the model may not be complete. In the presented work, the ADM has thus been used as a basis for analysing the experimental results, and adaptations have been made to the model to improve its ability to describe the experimentally observed behaviour under ion irradiation.

Chapter 3

Wide band gap oxide materials

This chapter introduces the materials relevant to the presented work. The opening section gives a high level overview of all the studied materials, while Section 3.2 covers the prime subject, In_2O_3, in more detail.

3.1 Short history of certain oxides

The wide band gap oxides is a subclass of the wide band gap compound materials, where the cation(s) usually come from group(s) IIB or IIIA of the periodic table, and the anion is oxygen. The materials studied in this work include CdO, Ga_2O_3, In_2O_3, SnO_2 and ZnO. Their history started with CdO in 1907 when Bädeker discovered that an oxidized cadmium film turned transparent [57], but research was rather sparse until the latter half of the century. In the 1970s, ternary Cd oxides were investigated, but high deposition temperatures or post deposition treatments were required for high quality films and limited the enthusiasm for this material system. Indium doped CdO with very low resistivity ($\rho \sim 6 \times 10^{-5}\,\Omega\,\mathrm{cm}$) has been demonstrated, but due to the toxicity of Cd, CdO is not widely researched for commercial applications today. Its high mobility does, however, give the material scientific interest [58–60].

SnO_2 is a semiconductor with a band gap of 3.6 eV crystallizing in the rutile structure under ambient conditions [61]. Research on SnO_2 was reported at least as early as the 1930s [62] with the key applications being antistatic coatings and aircraft windshield heaters [58, 63]. Modern day applications include gas sensors [61] and as catalysts for chemical reactions [64].

ZnO crystallizes in the wurtzite structure [65], and has a band gap of 3.37 eV [66]. Like SnO_2, ZnO was also researched structurally in the 1930s [67], and was found to have promising TCO properties by 1971 [68]. Issues with thermal stability of the films did dampen the enthusiasm somewhat but a wide range of dopants and deposition processes were examined through the 1980s. In the 1990s ZnO-containing ternary oxides were investigated, and in 2000 a $ZnO/SrCu_2O_2$ all-oxide pn-junction was demonstrated [58]. For several decades considerable attention has been directed towards lowering the resistivity of ZnO by doping with e.g. aluminium or gallium, and a resistivity as low as $8.1 \times 10^{-5}\,\Omega\,\mathrm{cm}$ has been achieved in Ga-doped ZnO [69]. This is on par with the industry standard In_2O_3:Sn (ITO) (record $\rho = 7.2 \times 10^{-5}\,\Omega\,\mathrm{cm}$ [70]) but achieving sufficiently low resistivities with high deposition rates uniformly over large areas and with consistent quality has proven challenging. Hence, ZnO is still not as common as ITO for transparent electrodes.

Ga_2O_3 was first characterized in the 1950s [71], and a fairly modest amount of work was conducted from then and until the early 2000s. The material

crystallizes in a range of polymorphs, of which the β-phase is the most stable under standard conditions [11]. This structure is monoclinic and has a band gap of 4.8 eV [11]. From the turn of the millennium Ga_2O_3 research has largely been fueled by its very promising properties for high power electronics. Specifically, the breakdown field strength estimated as high as 9 MV/cm [72] far exceeds that of silicon (0.3 MV/cm), and is also considerably higher than competing wide band gap materials such as GaN (5 MV/cm) and 4H-SiC (3 MV/cm) [73].

3.2 Indium oxide

A patent by Zunick [74] shows that transparent conductors based on indium had been discovered already in the 1940s. At the time the researchers did, however, not know the composition of the material, but suggested oxygen as a probable constituent. Like many of the other TCOs, more systematic research on In_2O_3 started in the 1950s [75], and the very low resistivity of heavily tin doped material (ITO) makes In_2O_3 the most widely used TCO to date. Already in 1972 a resistivity of $\rho = 1.77 \times 10^{-4}\,\Omega\,\mathrm{cm}$ was reached, while maintaining an optical transmittance of 85% in the visible range [76]. Throughout the 1980s ITO saw widespread use in liquid crystal displays, electroluminescent lamps etc. Throughout the 1990s the research activity really began to pick up, but no major improvements in resistivity of ITO could be achieved. Although some samples with resistivities on the order of $10^{-5}\,\Omega\,\mathrm{cm}$ were produced [70], most samples had, and still have to this day, $\rho \sim 1 \times 10^{-4}\,\Omega\,\mathrm{cm}$ i.e. in the same range as doped ZnO. Nevertheless, due to the availability of large area, high throughput deposition of high quality films, ITO is still the most commonly used material for transparent conductive coatings with applications in solar panels, flat panel displays, smart windows, etc. [5].

Under atmospheric pressure, In_2O_3 takes the cubic bixbyite structure. This can be seen as a variation of the fluorite structure with 1/4 of the oxygen atoms missing [78] and is shown in Figure 3.1 (a). The indium atoms occupy two inequivalent sites, whereas all the oxygens are on equivalent sites of the structure. The bixbyite structure is relatively complex, with 80 (40) atoms in the conventional (primitive) unit cell [78], making this a challenging system to study computationally.

The fundamental band gap of In_2O_3 is direct and has a width of ~ 2.9 eV [79]. However, only weak optical absorption is observed at this energy, and for decades the band gap was believed to be indirect [80, 81]. Through combined experimental and theoretical efforts it has later been found that the band gap is in fact direct, and that the cause of the weak absorption is that VBM $\rightarrow$ CBM transitions are dipole forbidden [79]. Strong photon absorption does not set in before $h\nu \sim 3.7$ eV, corresponding to excitation to the CBM from a valence band 0.81 eV below the VBM [79, 82].

In_2O_3 exhibits a flat valence band and dispersive conduction band with a pronounced dip at the Γ-point significantly lower than the average CB [77], as

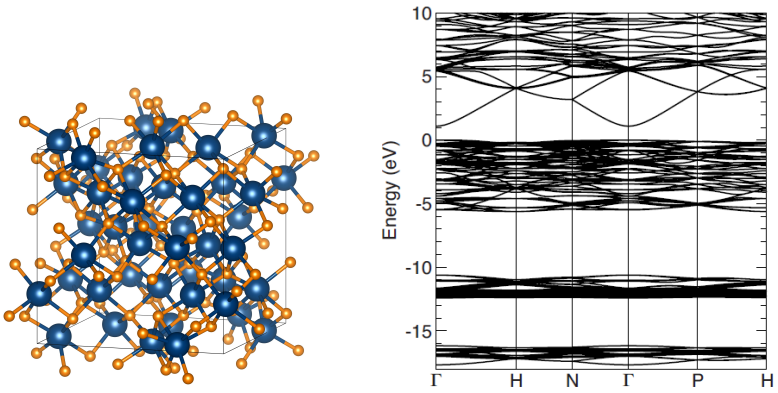

(a) (b)

Figure 3.1: (a) The unit cell of bixbyite In_2O_3 with indium atoms shown in blue and oxygen atoms in orange. The illustration was created using the VESTA software [33]. (b) The band structure of In_2O_3 showing the flat valence bands and dispersive conduction band [77]. The energy scale is defined relative to the valence band maximum.

shown in Figure 3.1 (b). This band structure positions the charge neutrality level 0.65 eV above the Γ-point CBM [79] and, consequently, In_2O_3 allows a very high carrier concentration before compensating defects are formed. $n = 2 \times 10^{21}\,\mathrm{cm}^{-3}$ has been achieved with $\sim 7\,\%$ Sn doping [83], and even nominally undoped samples frequently have n on the order of $10^{19}\,\mathrm{cm}^{-3}$. Another consequence of the high CNL is accumulation of electrons at the surface [79]. This accumulation layer facilitates the formation of Ohmic contacts, but makes rectifying contacts and -devices very challenging to realize [24].

Chapter 4

Methodology

In this chapter, the experimental and theoretical techniques employed in the current work are presented. Sections 4.1 and 4.2 cover sample synthesis and -modification, namely through physical vapor deposition (PVD) and ion irradiation. The following two sections cover electrical characterization, followed by Section 4.5 on structural characterization via x-ray diffractometry (XRD). Optical characterization techniques are outlined in Sections 4.6 and 4.7 before the chapter is concluded with an introduction to the theoretical framework of density functional theory (DFT) in Section 4.8.

4.1 Physical vapor deposition

This section outlines methods for growing thin films of semiconductor material on top of some kind of substrate. The choice of substrate material depends both on the material to be grown, the final application of the device and the growth technique being used. To achieve the best possible crystal quality, materials should ideally be grown on a substrate of the same crystal structure and a similar lattice constant as the film. If the growing film is able to adopt the crystal structure of the substrate, the growth is said to be epitaxial. Growth on too dissimilar of a substrate will tend to strain the film and can result in the formation of extended defects [84, p. 49].

In certain applications, e.g. where some property of the film should be isotropic, amorphous films may in fact be desirable and the substrate does thus not need to be lattice matched to the film. In this case amorphous substrates like glass or plastics can be viable, given that they meet the other requirements of the deposition and device application. Constraints originating from the deposition technique can include thermal and chemical stability, while the application of the film may dictate properties such as optical transparency, physical stability, flexibility, electrical- and thermal conductivities etc.

For the presented work depositions have been performed using pulsed laser deposition and molecular beam epitaxy by collaborating research groups at Universität Leipzig, University of Canterbury, and Université Côte d'Azur. The following two sections provide brief introductions to these techniques.

4.1.1 Pulsed laser deposition

During pulsed laser deposition (PLD) atoms are ejected from a target by an incoming energetic laser beam. This use of photons as the primary beam in place of the ions used in the alternative technique sputtering is one of the key advantages of PLD. The photons will not change or contaminate the target,

resulting in a better transfer of the target stoichiometry to the deposited film [85, 86]. Laser wavelengths from UV to IR can be used, depending on the absorption of the material to be deposited. As the focused laser beam strikes the target, the localized heating ablates the target material. The resulting vapour deposits on the substrate, which is typically located some centimeters away from the target. Substrate heating increases the energy of the adsorbed atoms, thereby increasing their probability of settling into a lattice position and consequently improving the film quality.

In more advanced applications of PLD multiple targets can be ablated in the same process, allowing multi-target alloys or stacks of different materials to be produced. The ability to focus the laser beam to a small spot also gives exciting possibilities for novel films to be produced. If a single target where the material composition varies either in segments or radially is used, and the target and/or substrate is moved in a coordinated manner relative to the laser spot during deposition, films with vertical, lateral, radial or segmented compositional gradients can be deposited [87]. Using analysis techniques such as reflection high-energy electron diffraction (RHEED) during deposition, the film thickness can be controlled with monolayer resolution.

4.1.2 Molecular beam epitaxy

Perhaps the most advanced of the PVD techniques is molecular beam epitaxy (MBE) [88, pp. 229–230]. As the name implies this technique produces epitaxial thin films from a beam of molecules or atoms, which is generated by radiatively heating a charge of the desired material in a Knudsen cell. The key advantage of MBE over the other PVD techniques is the extremely low concentration of defects and impurities [89, pp. 438–449]. In order to deposit high quality films extreme cleanliness of the entire process is required. This includes operation in ultra high vacuum (UHV), with base pressures typically around 10^{-10} torr. Further, the substrate must be cleaned and heated in situ prior to deposition. By monitoring the temperature of the charge, the deposition rate can be adjusted, and is typically maintained at around 1 µm/hr. Like for PLD, RHEED can be used to achieve monolayer control over the film thickness.

4.2 Ion irradiation

Ion irradiation is strongly related to ion implantation, which is an essential process in the semiconductor industry, where the fundamental difference lies in the desired outcome of the experiment. In implantation the goal is to introduce a controlled concentration of atoms into a material by way of an energetic ion beam. An unwanted byproduct of this process is defects in the atomic structure of the sample, and post-implantation annealing is often necessary to recover an acceptable crystal quality. In ion irradiation the roles are switched, the defects are the desired features and any incident ions trapped in the sample is the unwanted byproduct.

In both cases an electric field accelerates ions of the desired element towards the sample at a well defined energy. The energies used are so high that the incoming ions penetrate into the sample where they lose energy through interactions with nuclei and electrons along their path of travel. During each ion-nucleus interaction there is a finite probability that the transferred momentum will permanently displace the nucleus from its lattice site, resulting in a Frenkel defect pair. After undergoing a series of ion-nucleus and ion-electron interactions, the ion comes to rest. The ion concentration plotted as a function of depth follows an approximately gaussian curve, where the depth of the peak is termed the *projected range*, R_p, determined by the sample material along with the ion species and its incident energy.

In this section, a short overview of ion irradiation is presented. First, the key components of the experimental setup is described, before the various ways in which ions can interact with the target is explained.

4.2.1 Instrumentation

The key components of an ion implanter include (i) an ion source, (ii) a mass analyser, (iii) an accelerator, (iv) beam shaping/scanning lenses and (v) a target chamber [90, Ch. 4]. In the ion source the element to be implanted is injected into a plasma chamber. Gaseous elements can be introduced simply by supplying the gas to the chamber at a suitable pressure, while solid elements can be introduced either by thermal evaporation or by sputtering. In the plasma, electrons are boiled off a cathode filament by resistive heating and electrostatically accelerated towards an anode. Before reaching the anode some of the electrons collide with, and thereby ionise, the gaseous element to be implanted. The ions are extracted from the plasma by an extraction electrode and directed towards a mass analyser. The purpose of the mass analyser is to "clean" the ion beam from all unwanted species, such that only the desired element continues towards the target. This mass separation is accomplished using a magnetic field of magnitude B to guide the beam through a bend in the beam line. The curve taken by a particle of mass m and charge q accelerated by a potential $V_\mathrm{ext.}$ is given by [89, Ch. 5]

$$r = \frac{1}{B}\sqrt{2\frac{m}{q}V_\mathrm{ext.}}. \tag{4.1}$$

For a fixed $V_\mathrm{ext.}$ the magnetic field is then tuned such that only ions with the desired mass-to-charge ratio successfully navigate the curve in the beam line. Heavier (or less charged) ions will not be sufficiently affected by the B-field and hit the outside wall of the beam line. Lighter (or more highly charged) ions will turn too sharply and hit the inside wall of the beam line. Modern mass analysers can be made sufficiently sensitive to select only a single isotope from the ion beam.

Following the mass separation, the ions enter an acceleration tube where they are electrostatically accelerated by a potential in the range from a few kV upwards to hundreds of MV, depending on the purpose of the experiment and the capability of the instrument. For doping purposes in the semiconductor

industry, energies on the order of tens or hundreds of kV are typically used [90, p. 488]. Depending on the layout of the implanter the acceleration can also be performed prior to the mass separation, but this necessitates the use of stronger magnets in the mass analyser.

In the target chamber, the ion beam is focused on the target surface, and scanned across the desired area to be implanted by a raster scanner. Depending on the particular experiment, cooling or heating of the sample can be implemented in situ.

4.2.2 Ion-Matter Interactions

The rate of energy loss of an ion traveling through a solid slab of material can be expressed as

$$dE/dx = (dE/dx)_{\text{nuclear}} + (dE/dx)_{\text{electronic}} + (dE/dx)_{\text{radiation}} \tag{4.2}$$

where the radiative component is so weak that it will be neglected in the following [91, p. 48].

During electronic stopping the primary ion excites or ionizes the sample atoms, and the deposited energy is transferred to the lattice through electron-phonon interactions. This process dominates at high energies, typically $> 100\,\text{keV/amu}$, and the energy loss rate can range from a few eV/nm to tens of keV/nm depending on the mass and energy of the primary ion [91, pp. 48–49].

Nuclear energy loss is an elastic scattering process where energy is transmitted from the incident ion to the scattering atom as a whole, and dominates at energies below about 10 keV/amu. This type of scattering ejects atoms from their lattice sites and creates Frenkel pairs. If sufficiently energetic, the ejected atoms can eject further atoms resulting in a cascade of scattering events where the incident ion can dramatically change direction with each interaction. Energy loss rates can be from a few eV/nm upwards to a few keV/nm, again depending on the mass and energy of the primary ion.

From this it follows that an ion entering a sample will initially lose its energy by electronic stopping, while the relative strength of nuclear stopping increases as the ion penetrates further into the sample. The damage profile (concentration of defects versus depth) is thus not uniform, but rather increases from the surface to a peak, sightly shallower than R_p [92]. This complicates ion irradiation experiments, where high defect concentrations are often wanted far away from R_p.

During irradiation a cascade of ions and ejected atoms are chaotically moving around in the lattice. During this process some proportion of the ejected atoms find their way back to an empty lattice site, and thus do not end up as a defect. This process is called dynamic annealing, and it has been found that as many as 99% of the ejected atoms return to lattice sites rather than settling in interstitial positions [93–95]. As much as dynamic annealing is a benefit during implantation, it is a challenge for irradiation, causing correspondingly higher doses to be required for achieving the desired defect concentration. In order to

limit both dynamic annealing and defect diffusion ion irradiation experiments can be conducted at cryogenic temperatures.

4.3 Current–voltage measurements

The current-voltage (IV) measurement is one of the fundamental experiments for electrical characterization, both on device level and in materials science. For this discussion it will be assumed that the device under test is a homogeneous semiconductor thin film contacted by two metal probes. In principle an IV measurement involves supplying a known bias voltage (V) between the probes and measuring the current (I). From such a measurement one can calculate the resistance (R) through Ohm's law, $R = V/I$, and, if the geometry of the sample is known, the resistivity (ρ) can be obtained via the equation

$$\rho = RA/l \tag{4.3}$$

where A and l are the cross sectional area through which the current flows and l is the distance between the probes.

One of the assumptions of Ohm's law is that the contacts between the probes and the sample are Ohmic (i.e. non-rectifying). If this requirement is not met, the current will have a non-linear dependence on the applied voltage. As a consequence, the resistance of the circuit is voltage dependent and calculating the resistivity of the sample becomes impossible. A test for Ohmic behaviour is to repeat the IV measurement at a range of bias voltages and verify that the current varies linearly with the voltage.

According to the Schottky-Mott rule, whether a metal-semiconductor junction is Ohmic or rectifying depends only on the work function of the metal ($q\Phi_\mathrm{m} = E_\mathrm{vac} - E_\mathrm{F}$) and the electron affinity ($q\chi = E_\mathrm{vac} - E_\mathrm{c}$) of the semiconductor (assuming n-type), where E_vac is the vacuum level, as shown in Figure 4.1 [96].

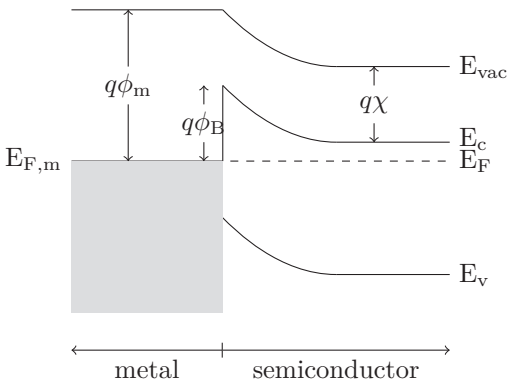

Figure 4.1: Band diagram of a metal-semiconductor junction.

As it can also be seen from the figure, the interface barrier height between the metal and semiconductor is given by

$$\Phi_{\mathrm{B}} = \Phi_{\mathrm{m}} - \chi. \tag{4.4}$$

Thus, low work function metals, such as aluminium, titanium, silver or indium, along with semiconductors with high electron affinities should yield Ohmic contacts.

In practice it has been found that the presence of native oxides or contaminants at the metal-semiconductor interface, and semiconductor surface states, can make fabrication of an Ohmic contact considerably more challenging than simply picking the correct metal [97, p. 136].

4.4 The Hall effect

The Hall effect measurement is a more advanced electrical characterization technique than the IV measurements described above. From such a measurement one can extract the resistivity (ρ), mobility (μ) as well as the majority carrier concentration (n) and polarity of a sample. This is achieved by direct measurements of the resistivity and carrier concentration, from which the mobility can be calculated and the polarity inferred.

Hall effect measurements can be performed both on purpose made structures, so called Hall bars, or on samples of arbitrary shape through the use of the van der Pauw approach. Although the latter requires the sample to be flat, homogeneous, and without holes it is far more flexible and will be the topic of this section

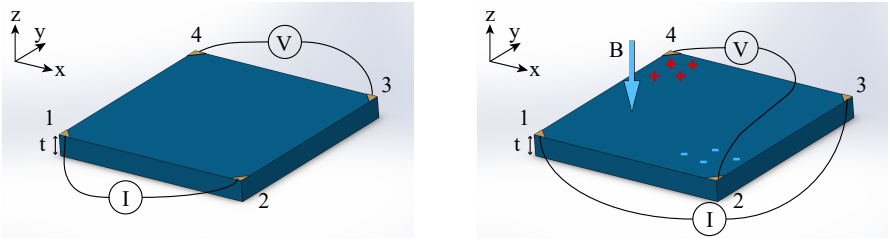

Figure 4.2: (a) Illustration of a Hall sample connected for resistivity measurement. (b) Hall sample connected for measuring the carrier concentration. Passing a current between contacts 1 and 3 while applying a magnetic field (B) normal to the plane of the sample causes accumulation of electrons closer to contact 2.

4.4.1 Measuring resistivity

Assume a square sample of thickness t, with electrical contacts of negligible size in each corner labelled $1-4$, as shown in Figure 4.2 (a). If a current, I_{12} is passed between contacts 1 and 2, while measuring the voltage drop between contacts 3 and 4, $V_4 - V_3$, the resistance will be

$$R_{12,34} = \frac{V_4 - V_3}{I_{12}}. \tag{4.5}$$

Equivalently, if a current is passed between contacts 2 and 3, while the voltage drop is measured between 1 and 4, the measured resistance is

$$R_{23,14} = \frac{V_4 - V_1}{I_{23}}. \tag{4.6}$$

The van der Pauw theorem [98] states that in this situation

$$\exp\left(-\frac{\pi t}{\rho}R_{12,34}\right) + \exp\left(-\frac{\pi t}{\rho}R_{23,14}\right) = 1, \tag{4.7}$$

from which the resistivity can be determined as

$$\rho = \frac{\pi t}{\ln(2)}\frac{R_{12,34} + R_{23,14}}{2}F, \tag{4.8}$$

where F is a transcendental equation which depends on the sample geometry.

4.4.2 Measuring carrier concentration

Consider again the sample in Figure 4.2 (a), and let a current, I_{13}, run between contacts 1 and 3. In the absence of any additional external influence, the charge carriers constituting the current will travel in a straight line between the two contacts with an average velocity v, determined by

$$v = \frac{I_{13}}{nAq} \tag{4.9}$$

where A is the cross sectional area of the sample and q the elementary charge. This, and the following equations can be found in introductory semiconductor physics texts, e.g. Streetman's Solid state electronic devices [99, pp. 83–90].

If a magnetic field B is applied in the negative z-direction, as indicated in Figure 4.2 (b), the Lorenz force $F_L = qvB$ caused by the field pushes the charge carriers perpendicularly to both the current and the B-field, with the direction given by the carrier polarity. The Lorenz force thus causes an accumulation of majority carriers on one side of the sample, and a depletion on the other. This separation of charge continues until the force, F_E, of the resulting electric field, E, exactly balances the Lorenz force. In that case,

$$F_E = F_L \tag{4.10}$$
$$qE = qvB \tag{4.11}$$
$$qE = q\frac{I}{nAq}B \tag{4.12}$$
$$E = \frac{IB}{qnA}. \tag{4.13}$$

The voltage set up by this field is called the *Hall voltage*,

$$V_H = \frac{IB}{qnt}, \tag{4.14}$$

from which the *Hall coefficient*, R_H, is defined as

$$R_H = \frac{V_H t}{BI}, \tag{4.15}$$

and the carrier concentration is then given by

$$n = \frac{1}{q|R_H|}. \tag{4.16}$$

With both the resistivity and carrier concentration known, the mobility can be calculated from

$$\mu = \frac{1}{qn\rho}. \tag{4.17}$$

The sign of the Hall coefficient indicates the polarity of the majority carriers, negative for electrons and positive for holes.

This discussion has tacitly assumed that the scattering mechanisms limiting the mobility are energy independent. If this is not the case, a correction can be made by multiplying Equation (4.16) by an appropriately defined Hall scattering factor, r. A detailed treatment of the Hall scattering factor can be found in Chapter 8 of [100].

4.4.3 Temperature dependent measurements

By repeating the above mentioned measurements over a range of temperatures additional information can be extracted. By examining the temperature dependence of the carrier concentration it is possible to identify the donor or acceptor levels from which the majority charge carriers originate.

The temperature dependence of the mobility can reveal the nature of the most important scattering mechanisms of the sample. For many semiconductors ionized impurities or acoustic phonons are the main scatterers. In non-degenerate samples, mobility limited by these two mechanisms will follow

$$\mu_{\mathrm{ii}} \propto T^{3/2}, \text{for ionized impurities or} \tag{4.18}$$
$$\mu_{\mathrm{ph}} \propto T^{-3/2}, \text{for phonons [99, p. 86].} \tag{4.19}$$

For degenerately doped samples ionized impurity scattering temperature independent [101].

4.5 X-ray diffractometry (XRD)

X-ray diffraction spectroscopy (XRD) is a technique used for characterizing the atomic structure and crystal quality of (poly)crystalline materials. Diffraction effects occur when an electromagnetic wave interacts with objects of size similar to its wavelength. Hence, as typical interatomic spacings in solids are on the order of angstroms, x-rays of similar wavelengths will diffract from ordered planes of atoms when incident on a solid sample.

Figure 4.3 illustrates two planes of atoms of a crystal. It can be identified that electromagnetic waves reflected from these layers will be in phase (interfere constructively) when the condition

$$n\lambda = 2d\sin(\theta) \tag{4.20}$$

is fulfilled. In this equation, n is an integer, λ is the x-ray wavelength, d is the atomic interplanar spacing and θ is the angle between the incident x-ray and the sample surface normal [102, pp. 1–38]. By irradiating the sample with monochromatic x-rays of wavelength λ over a range of angles (θ), a diffractogram is produced. Peaks in the diffractogram appear at angles which fulfil Equation (4.20), and thus allows calculation of the interplanar spacing d of the sample. The interplanar spacing is in turn a fingerprint of the material, and by comparing the measurement result with a database of known diffractograms the sample material and its structure can be determined.

In addition to the crystal structure of the sample, the peaks of the diffractogram also contains information about the crystal *quality*, i.e. the grain size. Scherrer found that, for a peak centered at θ with a full width at half maximum (FWHM) of B, the mean size of the crystallite domains giving rise to the peak is given by

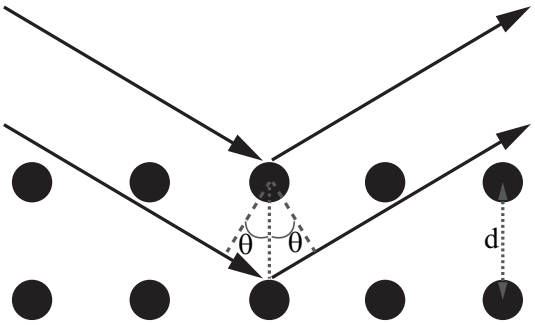

Figure 4.3: Bragg diffraction of x-rays from atomic planes.

$$L = \frac{K\lambda}{B\cos(\theta)}, \tag{4.21}$$

where K is a numerical constant close to unity [103].

4.6 Cathodoluminescence spectroscopy (CL)

Cathodoluminescence (CL) spectroscopy is an optical characterization technique where an electron beam is used to excite electrons out of their ground state. The photons emitted as the excited electrons subsequently relax are detected as a function of wavelength (or equivalently, energy) and allows determination of the energy levels involved in the transition [100, pp. 651–652]. As illustrated schematically in Figure 4.4 a variety of levels can support photon emitting transitions. Examples of such transitions include recombination from the conduction band or a donor level to the valence band or an acceptor level, as well as recombination of excitons [104].

In principle CL yields much the same information as the more widely known technique photoluminescence spectroscopy (PL), where the same recombination mechanisms are studied but electrons are excited by a laser rather than an electron beam. A few notable differences between these techniques include that the CL instrumentation is usually integrated in a scanning electron microscope (SEM), allowing simultaneous recording of surface topography and the luminescence spectrum which can be valuable for inhomogeneous samples. SEM integration also provides an improved spatial resolution over what is available in PL instruments, and the ability to tune the probe volume via the electron acceleration voltage. Further, the electron beam used in CL carries greater energy and momentum than the laser photons employed in PL, hence different selection rules govern the electron excitation in the two techniques [105]. In CL, the high energy of the primary electrons enables excitation through several steps [105], e.g. a primary

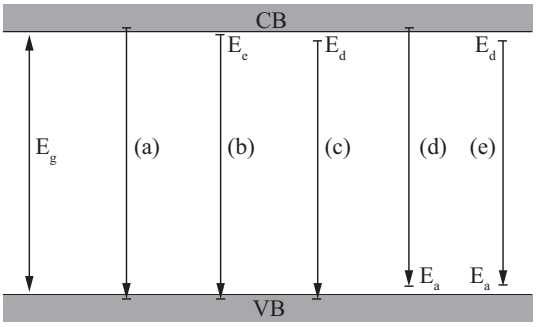

Figure 4.4: Radiative recombination mechanisms for an excited electron. Illustrated are recombination from CB to VB (a), exciton to VB (b), donor to VB (c), CB to acceptor (d), donor to acceptor (e). After [104].

electron can excite a plasmon which in turn generates one or more electron-hole pairs [106].

In order to extract the emitted photons, a parabolic mirror is used. The mirror collects the emitted light and directs it onto a grating spectrograph where wavelengths can be separated with a spectral resolution down to 0.1 nm in the visible region [105]. The intensity of the light reflected from the grating is measured by a silicon photodetector for the UV to NIR ranges, or an InGaAs detector for wavelengths up to about 2 µm. With high resolution optics the spectral resolution of a CL spectrum can be limited by thermal broadening which is on the order of $k_B T \sim 26$ meV at room temperature. To improve the resolution, and at the same time improve intensity by limiting thermalization of the excited electrons CL experiments are frequently performed at cryogenic temperatures.

4.7 Optical transmittance spectroscopy

As the name suggests, transmittance spectroscopy measures the optical transmittance of a sample over a wavelength range of interest. For thin film semiconductor applications this range is typically found somewhere between the ultraviolet and the infrared. The transmittance T of a sample can be expressed as a function of the absorption and reflection coefficients α and R, respectively, the refractive index, n, and the sample thickness t by

$$T = \frac{(1-R)^2 e^{-\alpha t}}{1 + R^2 e^{-\alpha t} - 2Re^{-\alpha t}\cos(\phi)}, \tag{4.22}$$

where $\phi = 4\pi nt/\lambda$ for light of normal incidence on a sample with equal front and back reflection.

The most prominent feature in a transmittance spectrum for a semiconductor material is the onset of absorption due to excitation of electrons across the band gap. Other commonly observed phenomena include exciton absorption at energies slightly below the band gap [107] and intraband free carrier absorption (FCA) at energies corresponding to IR or microwave wavelengths [108]. Phonon assisted absorption [109] and defect transitions also limit the transmittance at energies lower than the band gap.

Transmittance data are frequently used for estimating optical band gaps through the use of of Tauc plots [110]. A Tauc plot shows the relation between the absorption coefficient α and the band gap

$$(\alpha h\nu)^x = A(h\nu - E_g) \tag{4.23}$$

where $h\nu$ is the photon energy, and $x = 2$ or $x = 1/2$ for direct or indirect band gaps, respectively. By plotting the left hand side of Equation (4.23) as function of $h\nu$, the band gap can be estimated from a linear extrapolation of the absorption edge to the $h\nu$-axis.

4.8 Density functional theory (DFT)

In principle, all physical and chemical properties of a material follows from its Schrödinger equation. The Schrödinger equation for a piece of material with multiple nuclei and electrons, can be expressed as

$$\left[-\frac{\hbar^2}{2m}\sum_{i=1}^{N}\nabla_i^2+\sum_{i=1}^{N}V(\mathbf{r}_i)+\sum_{i=1}^{N}\sum_{j<i}U(\mathbf{r}_i,\mathbf{r}_j)\right]\psi=E\psi \tag{4.24}$$

with m being the electron mass, ψ the electron wave function, and E the ground state energy of the collection of electrons [111]. On the left hand side of the equality, the first term describes the electron kinetic energy, the second describes electron-nuclei interactions, and the last term describes electron-electron interactions. Unfortunately, as the electron wave function depends on the spatial position of every electron in the system, solving this equation has a prohibitively high computational cost. In order to theoretically predict chemical and physical properties of a material from a quantum mechanical description some other approach must thus be devised.

One such approach is density functional theory (DFT). DFT is based on two theorems by Hohenberg and Kohn which, in common terms, state that (i) all properties of a material in its ground state can be calculated from the ground state electron density $n(\mathbf{r})$, where $\mathbf{r}$ defines positions in space, and (ii) in the ground state the electrons distribute themselves in such a way that the total energy of the system is minimised. Statement (i) is directly linked to Equation (4.24) by the fact that

$$n(\mathbf{r})=2\sum\psi_i^*(\mathbf{r})\psi_i(\mathbf{r}) \tag{4.25}$$

where the asterisk denotes the complex conjugate, the factor 2 accounts for spin and the sum runs over all the single electron wave functions. The single electron wave functions can in turn be found from the Kohn-Sham equations

$$\left[-\frac{\hbar^2}{2m}\nabla^2+V(\mathbf{r})+V_H(\mathbf{r})+\mathbf{V_{XC}}(\mathbf{r})\right]\psi_i(\mathbf{r})=\epsilon_i(\mathbf{r})\psi_i(\mathbf{r}), \tag{4.26}$$

where the terms in the bracket describe the electron kinetic energy and the potentials arising due to electron-nucleus interactions, electron-electron interactions and electron exchange and correlation, respectively. Using Equation (4.26) the electron density is found through an iterative procedure of first defining a trial electron density, calculating the single electron wave functions and the resulting electron density, updating the electron density with the new value and calculating the single electron wave functions until convergence.

A key challenge in this procedure is that the exchange-correlation potential V_{XC} is generally not known. The only case for which an exact V_{XC} has been found is the uniformly distributed electron gas, where $n(\mathbf{r})=$ constant. The use of this exchange-correlation potential is termed the local density approximation (LDA). Although enabling the determination of the electron density and in turn

any other material property of interest via Equation (4.26), this approximation is unfortunately rather crude, and the results based on the LDA are often inaccurate.

A logical improvement of the LDA is to allow for spatial variations in the electron density by including its gradients in the exchange-correlation potential. A variety of such approaches exist and they are collectively referred to as generalized gradient approximations (GGAs). Of these, the PBE functional [112], named after its developers Perdew, Burke and Ernzerhof, is particularly popular for semiconductor materials.

4.8.1 The Hartree-Fock (HF) method

A slightly different way of modeling the behaviour of electrons in a solid was developed by Hartree and Fock. In their approach, the eigenfunctions are spin orbitals $\xi_j(\mathbf{x}) = \sum_{i=1}^{N} a_{i,j}\phi_i(\mathbf{x})$, where both the position and spin of electron j are defined by $\mathbf{x}$, and the ϕs are functions which are weighted by the coefficients $a_{i,j}$ [111, pp. 19–23]. Being considerably heavier than the electrons, the atomic nuclei are assumed stationary and the Schrödinger equation for the system reads

$$\left[-\frac{\hbar^2}{2m}\nabla^2 + V(\mathbf{r}) + V_H(\mathbf{r})\right]\xi_j = E_j\xi_j \tag{4.27}$$

where the terms have the same meanings as in Equation (4.26). The algorithm for solving this equation follows a similar procedure to that for solving Equation (4.26). First, the ξs are estimated by qualified guesses on the weights $a_{i,j}$. The electron density is calculated from ξ before the Schrödinger equation is solved. The ξs are updated, and the procedure is repeated until convergence.

4.8.2 Hybrid functional DFT

Although an improvement over the local density approximation, the predictions of the GGA techniques are still known to have systematic uncertainties, evidenced e.g. by underestimation of band gaps. Including an HF component in the DFT exchange-correlation functional to form a so-called hybrid functional has been found to improve the predictions, but a drawback is a dramatically increased computational cost.

The screened hybrid HSE functional of Heyd, Scuseria and Ernzerhof strikes a balance between the pure GGA approaches and the full hybrid functional. The HSE functional incorporates HF exchange, but with an increased spatial decay rate. The Coulomb potential for exchange is split into a long (LR) and a short range (SR) component giving the exchange-correlation functional

$$E_{\mathrm{XC}}^{\mathrm{HSE}} = \alpha E_{\mathrm{X}}^{\mathrm{HF,\ SR}}(\omega) + (1-\alpha)E_{\mathrm{X}}^{\mathrm{PBE,\ SR}}(\omega) + E_{\mathrm{X}}^{\mathrm{PBE,\ LR}}(\omega) + E_{\mathrm{C}}^{\mathrm{PBE}} \tag{4.28}$$

where the components are the short range HF exchange, short- and long range PBE exchange, and the PBE correlation functionals, respectively [113]. The

amount of HF exchange to include is determined by the value of the parameter α, and the screening parameter ω defines where the separation between long- and short range is to occur. The standard value of α in the HSE functional is 0.25. In practical applications the parameters can be tuned such that one of the predicted material properties, e.g. the band gap, matches the experimental value, and this has been found to greatly improve the predicted values of other material properties over the LDA and GGA functionals [114].

Chapter 5

Results

The primary focus of this project has been to examine the effect of intrinsic defects on the electrical properties of oxide semiconductors in general, and In_2O_3 in particular. The obtained results can be divided into four key areas, (i) material screening, (ii) the influence of the Fermi level, (iii) surface effects and (iv) the effect of the semiconductor composition. A summary of the main results from each of the key areas is presented in the following sections, while more detailed treatments are given in the corresponding papers.

5.1 Material screening

The recently published Ref. 55 revealed that the effect of the defect concentration on the electrical resistivity of In_2O_3 appeared to contradict the predictions of the amphoteric defect model. Specifically, while the ADM predicts a monotonic change in resistivity with defect concentration, a richer three-staged behaviour was experimentally observed under low-dose ion irradiation. From this finding, two new questions arose (i) does this apparent conflict with theory extend also to higher defect concentrations, and (ii) does this occur also in other materials? These questions were the topics of Paper I.

Thin films of CdO, Ga_2O_3, In_2O_3, SnO_2 and ZnO were deposited on electrically insulating sapphire substrates by PLD or MBE, and defects were introduced by irradiating the samples with silicon ions at an energy of 3 MeV. This energy is sufficient to propel the ions through the film and well into the substrate, enabling electrical examination of the generated cascade of intrinsic defects without interference from the primary ions. To limit dynamic annealing and defect diffusion, the experiments were carried out at a temperature of about 50 K. The samples were irradiated to a maximum accumulated dose of $10^{17}\,cm^{-2}$, and at selected doses the ion beam was blanked and the electrical resistance across the surface diagonal of the samples was measured by current-voltage (IV) sweeps.

Both qualitatively and quantitatively, the irradiation dose dependence of the resistance was found to vary greatly between the samples, as shown in Figure 5.1. Qualitatively the different materials can be grouped into three classes. In Ga_2O_3 and SnO_2 a dramatic increase in resistance was observed at doses of 10^{12} and $10^{13}\,cm^{-2}$, respectively, and their resistances exceeded the measurement range of our instrument throughout the remaining dose range. In CdO the resistance was virtually independent of dose throughout the range, whereas In_2O_3 and ZnO showed intermediate behaviours where the resistance increased to a peak and then subsequently decreased. For these latter two materials, irradiation to the highest doses turned the samples less resistive than in their corresponding

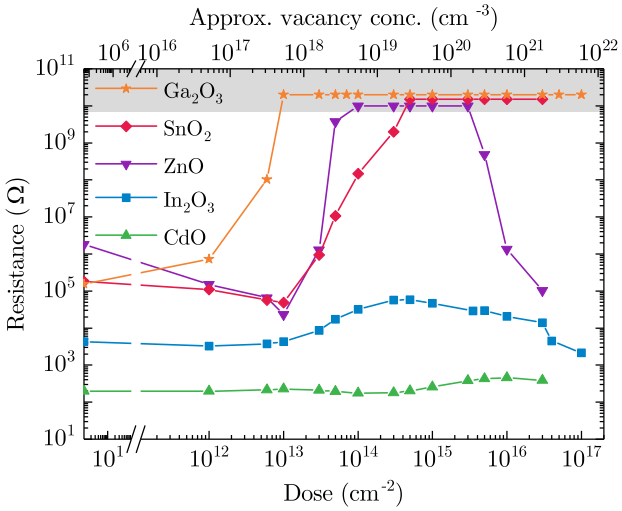

Figure 5.1: Resistance as function of irradiation dose for CdO, Ga_2O_3, In_2O_3, SnO_2 and ZnO as presented in Paper I.

as-grown state.

Considering solely the as-grown and fully irradiated data points for Ga_2O_3, In_2O_3 and ZnO, the defect concentration dependence of their resistance follows what would be expected from the amphoteric defect model [115, 116] with In_2O_3 and ZnO becoming less resistive, and Ga_2O_3 becoming more resistive, than in their as-grown states. However, the model does not predict the resistance peak at intermediate doses for In_2O_3 and ZnO. Moreover, following the predictions of the ADM, both CdO and SnO_2 would be expected to have a lower resistance after irradiation than in the as-grown state, in contradiction with our experimental data.

Applying the ADM to the resistance measurements is complicated by the fact that the resistivity depends not only on the carrier concentration, but the mobility as well. To separate the effects of these two contributions temperature dependent Hall effect measurements were performed on all of the as-grown samples, and on CdO, In_2O_3 and ZnO after the final irradiation. Measurements were attempted also on Ga_2O_3 and SnO_2 after irradiation, but these samples were found to be too resistive to measure in our Hall effect instrument. The results showed that the irradiation to a dose of $10^{17}\,\mathrm{cm}^{-2}$ increased the carrier concentration of all of the former three samples. Interestingly, while the mobility of CdO and ZnO decreased after irradiation, which one might intuitively expect due to additional scattering from the increased defect concentration, the mobility of In_2O_3 was found to increase. It is also noteworthy that for CdO, the increase in carrier concentration was of the same order of magnitude as the decrease in mobility. It thus seems reasonable to propose that this inverse relationship is the cause of the observed dose independence of the resistance of this sample.

To examine the effect of the irradiation on the crystal structure of the samples, x-ray diffractometry experiments were carried out. Prior to irradiation, the CdO sample was in the cubic phase, the In_2O_3 sample in the bixbyite phase, ZnO in the wurtzite phase, Ga_2O_3 in the beta phase and SnO_2 in the rutile phase, as expected from the growth parameters. It was found that the irradiation did not deteriorate the crystallinity of any of the samples, and no phase changes were observed.

The optical properties of all samples were studied by cathodoluminescence spectroscopy, and all samples except CdO were also studied by transmittance spectroscopy[1]. For Ga_2O_3, SnO_2 and ZnO the transmittance was found to change only weakly with irradiation. In In_2O_3, on the other hand, a pronounced decrease in transmittance was found at all wavelengths, particularly in the infrared region. At a wavelength of 2400 nm the transmittance dropped from about 70 % in the as-grown sample to $\sim$ 35 % after irradiation, attributed to increased free carrier absorption [117]. Tauc plots of the transmittance data indicated no change in optical band gap with irradiation, but a minor increase of the Urbach tail width was observed, correlating well with the increased defect concentration [118].

Wile the transmittance in general changed only very weakly with irradiation, the situation for cathodoluminescence emission was quite the opposite. With the exception of CdO, all the samples went from showing a broad luminescence peak in the visible and into the IR in the as-grown state to exhibiting virtually no radiative recombination at all after the ion irradiation. The reason for this lack of emission is believed to be the introduction of a large number of defect states through which the excited electrons can recombine non-radiatively [119, p. 99]. The CdO sample showed virtually no emission neither before nor after irradiation.

Comparing the resistance evolution with charge transition levels calculated by DFT, we propose that the resistance increase observed in ZnO and In_2O_3 is caused by the introduction of isolated Frenkel pairs. Specifically, in ZnO the deep 0/++ charge transition level of the oxygen vacancy (V_O) means that introducing a Frenkel pair on the oxygen sublattice in n-type material will lower the Fermi level and thus increase the resistance. In In_2O_3 the V_O donor transition level lies too close to the CBM to cause the resistance peak, but here the indium vacancy is triply negative and is expected to contribute. By further correlations with charge transition levels from DFT, the subsequent decrease in resistance at higher doses was found to be explainable by the formation of divacancies (ZnO) and antisites (In_2O_3) from the individual point defects.

[1]The CdO sample was not transparent due to a layer of molybdenum applied to the back side of the substrate to improve heating during film deposition, hence transmittance spectroscopy was not possible.

5.2 The effect of the initial Fermi level

During the material screening part of the project it was found that the peak of the dose dependent resistance curve for ZnO was significantly higher than that of In_2O_3, as shown in Figure 5.1. Hall effect measurements of the respective samples revealed an inverse relationship between the peak height and the as-grown Fermi level. The question of whether the difference in peak height was primarily a result of the material's atomic composition, or whether the initial Fermi level played the dominant role then arose, and this is the topic of Paper II.

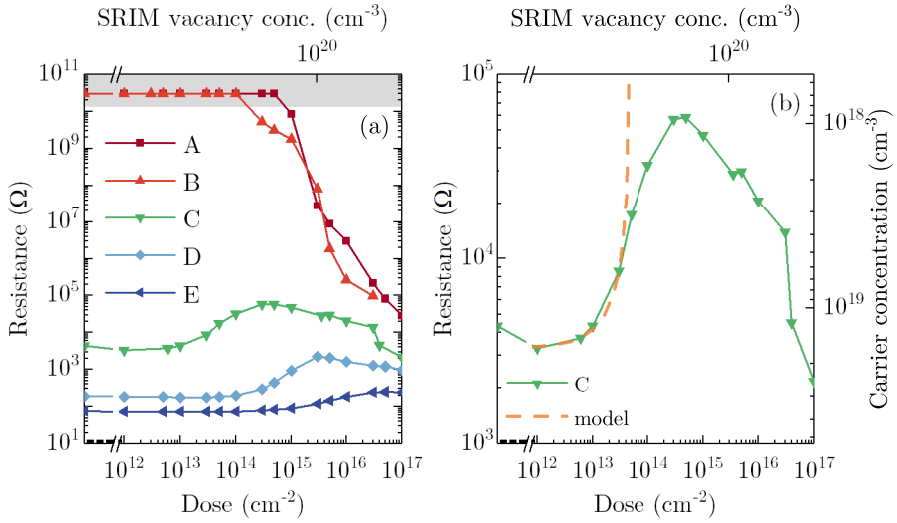

Figure 5.2: (a) Resistance as function of irradiation dose for In_2O_3 samples with various dopants and dopant concentrations. Samples A and B were doped with 1 % and 0.5 % Mg, respectively. Sample C was nominally undoped, while samples D and E were doped with 1 % and 10 % Sn, respectively. (b) Magnified view of the undoped sample C, with a linear defect generation model superimposed.

A set of In_2O_3 samples with varying dopant elements and -concentrations was deposited to study the effect of changing the initial E_F on the defect concentration dependent resistivity, while keeping the host material virtually constant. Two samples were acceptor doped with 1 % (A) and 0.5 % Mg (B), respectively, to compensate the unintentionally introduced donors, one sample was nominally undoped (C), while two other samples were donor doped with respectively 1 % (D) and 10 % (E) Sn. Subjected to the same alternating irradiation and IV-measurement routine as employed in Paper I, a clear trend in the behaviour of the samples arose. As shown in Figure 5.2, while the two Mg doped samples were initially too resistive to measure with our instrumentation, their resistance dropped within the measurement range after doses of 3×10^{14} and 10^{15} cm^{-2} for samples B and A, respectively. I.e., the most heavily compensated

sample required generation of a higher defect concentration before a measurable resistance was obtained. This finding agrees perfectly with the theory from Paper I which suggests that donor-like complexes, in this case indium- and oxygen antisites, are expected to be present at these doses.

Comparing the two Sn doped samples (D and E) with the unintentionally doped (UID) sample (C), it was found that increasing the as-grown Fermi level has three effects on the resistance-vs-dose curve. (i) As expected, the as-grown resistance is inversely proportional to the Sn concentration. (ii) Increasing the Sn concentration pushes the resistance peak to higher doses, and (iii) lowers the peak height relative to the as-grown value.

Through a comparison with a recent theoretical study of defects in In_2O_3 [23] a quantitative theory explaining the peak in the dose dependent resistance was formulated. The theory considers the defects, V_O, $O_{i,\,split}$, V_{In}^{b}, and In_i^{a}, as these constitute the most energetically favourable Frenkel pairs for the majority of the explored dose range. The ion irradiation generates Frenkel pairs at both sublattices, and at low doses the Frenkel pairs are considered as non-interacting species. With the considered set of point defects it is found that an oxygen Frenkel pair in the as-grown UID sample has a net charge state of zero, i.e. no effect on the carrier concentration. On the indium sublattice, In_i^{a} is in charge state $+1$ while V_{In} has a charge of -3, yielding a net charge state of -2. Thus, generating Frenkel pairs on both sublattices will trap electrons from the conduction band and thereby increase the resistivity of the sample.

As-grown, the UID sample had a carrier concentration of $1.3 \times 10^{19}\,\mathrm{cm}^{-2}$, corresponding to a Fermi level of $E_c + 110\,\mathrm{meV}$. According to the theoretical charge transition levels the resistance should increase until the Fermi level drops to $E_c + 60\,\mathrm{meV}$, where the charge states of In_i^{a} and V_O change from neutral and singly positive, respectively, to doubly and singly positive, making the net charge of one indium- and one oxygen Frenkel pair neutral. Our results show that the resistance increases further, until the corresponding Fermi level is $E_c + 20\,\mathrm{meV}$, which is thus adopted as a lower limit of the experimental pinning level.

Under the assumption of non-interacting defects in the low dose regime the survival rate of Frenkel pairs can be estimated. For this estimation, the rising flank of the resistance peak was linearly curve fit to defect generation rates simulated using the SRIM code [120]. A survival rate of 1.4 % was extracted, corresponding to a dynamic annealing rate of 98.6 %. This value is similar to e.g. silicon and zinc oxide and shows that In_2O_3 is a viable material for applications in radiation hard environments.

As the dose is increased, the probability of forming a defect in the vicinity of an already existing defect also increases. Reactions between neighbouring defects can thus occur without requiring significant diffusion, if energetically favourable for the overall system. Studying the charge states of the indium and oxygen antisites [23] it is found that both these complexes can contribute in shifting the resistance down from its peak value, hence the peak can be explained by a combination of isolated point defects pulling the resistance up at low doses and antisites pushing the resistance down at higher doses. Under our experimental conditions, the antisites are capable of shifting the Fermi level

at least up to $E_c + 210\,\text{meV}$. Unfortunately, no theoretical data exists for the charge states above this energy, but assuming the defects to remain in their $E_c + 210\,\text{meV}$-state this model successfully describes the resistance decrease to the ultimate dose point. Reversing the argument, our results could also be interpreted as experimental evidence of the antisites remaining net donors at least until $E_F = E_c + 300\,\text{meV}$.

5.3 Surface conduction

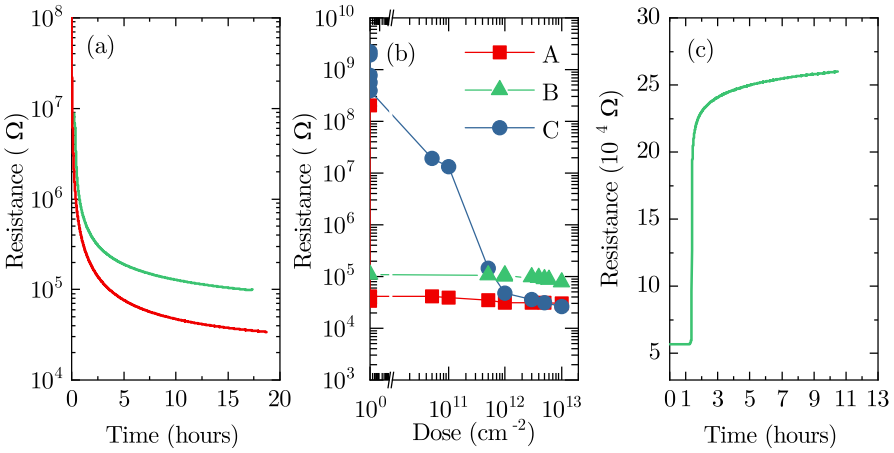

Figure 5.3: (a) Resistance versus time during UV illumination of $(In_{1-x}Ga_x)_2O_3$:Mg (A) and In_2O_3:Mg (B). (b) Resistance as a function of accumulated ion dose for samples with (A and B) and without (C) pre-irradiation UV exposure. (c) Resistance of sample B as function of time during post-irradiation exposure to O_2 gas. The legend in panel (b) applies to all panels.

A peculiar feature of the dose dependent resistance of SnO_2, ZnO and In_2O_3-based materials is a significant drop in resistance already at the lowest ion doses, as seen e.g. in Figure 5.1. This drop does not seem to be explainable by bulk defects as (i) the magnitude of the drop is far greater than what the concentration of introduced defects is expected to produce, and (ii) the defects generated at low doses in these materials are acceptors and should lead to an increase, rather than a decrease, of the resistance. With bulk defects considered unlikely, the sample surface emerges as a plausible contributor to the observed resistance drop. From research on the gas sensing properties of semiconductors it has been established that atoms or molecules adsorbed on the surface can influence the sample resistivity, and that such adsorbates can be removed by exposing the surface to ultraviolet light [10, 121]. To examine whether the same effect could be the cause of the decreasing resistivity during low-dose ion irradiation, a combined UV-illumination and ion irradiation experiment was conducted.

The three samples used for this experiment were all PLD grown on electrically non-conductive sapphire substrates. Two samples had compositions $(In_{1-x}Ga_x)_2O_3$:Mg, where $x = 17\,\%$ and the Mg concentration was $0.5\,\%$. These were grown on a single substrate in the same deposition run, and subsequently separated in nominally identical pieces labelled A and C. In addition, an In_2O_3:Mg sample with $0.5\,\%$ Mg, deposited in a separate run, is referred to as sample B. Prior to ion irradiation, samples A and B were exposed to 250 nm UV light overnight in high vacuum in the implantation chamber and, as shown in Figure 5.3 (a), their respective resistances were found to drop by approximately 4 and 3 orders of magnitude during the course of the UV exposure. Sample C was not subjected to the UV exposure or other pre-treatments and was irradiated in its as grown state.

Upon irradiating the samples with 3 MeV Si^{2+} ions, a clear difference was observed between samples A and B on one side, and sample C on the other. While the resistances of the illuminated samples were virtually unaffected by the irradiation, the resistance of sample C was seen to drop by ~ 4 orders of magnitude after an accumulated ion dose of $10^{13}\,cm^{-2}$, as plotted in Figure 5.3 (b).

To investigate the effect of oxygen adsorbates on the ion irradiated samples, the resistance of sample B was monitored during exposure to $99.999\,\%$ pure O_2 gas. Figure 5.3 (c) shows an abrupt increase in resistance when the gas is introduced between the 1 and 3 hour marks. Following the sharp initial increase, the rate of change decreases as the resistance approaches a value of $\sim 2.5 \times 10^5\,\Omega$, i.e. a factor ~ 5 higher than before the gas was introduced.

Comparing panels (a) and (b) of Figure 5.3 the similarity of the responses to UV illumination (samples A and B) and ion irradiation (sample C) is striking. Both UV light exposure and ion irradiation to a dose of $10^{13}\,cm^{-2}$ decreases the resistivity of the nominally identical samples A and C by about 4 orders of magnitude. This finding, along with the comparatively weak effect of post-illumination ion irradiation on samples A and B, is interpreted as a strong indication that a common mechanism may be responsible for the resistance drop under both UV illumination and ion irradiation. As UV-illumination mediated desorption of surface species is well established in the literature, (see e.g. [10, 121]) we propose that a similar surface modification can be caused by low dose ion irradiation. Desorption of surface species recovers the native surface states of the sample, causing a downward band bending and establishing a surface electron accumulation layer. This theory is further strengthened by the strong response of the resistance of sample B to oxygen gas, which is attributed to oxygen adsorbates reducing the magnitude of the downward band bending and thus weakening the SEAL. The fact that the resistance does not fully return to its pre-irradiated value can be explained by either (a) that the oxygen adsorbates are less efficient electron traps than the species present on the surface before the experiment, or (b) that the ion irradiation has introduced bulk donors. While the latter explanation appears to contradict the findings from Papers I and II where acceptors were formed in pure In_2O_3 at these doses, it is possible that the Mg doping of sample B makes donor formation energetically favorable already

at this low dose.

In summary, the developed model of irradiation induced changes in resistivity then comprises three parts. At doses below $10^{13}\,\mathrm{cm}^{-2}$ changes in the resistivity correlate with modifications of the adsorbate concentration at the surface. At doses in the range 10^{13}–$5 \times 10^{14}\,\mathrm{cm}^{-2}$ generation of primary defects dominate the resistivity evolution, while at higher doses defect complexes can take over the dominant role.

5.4 The effect of composition

As mentioned in Section 5.1 and shown in Figure 5.1 the material screening revealed a striking difference in the dose dependent resistance between In_2O_3 and Ga_2O_3. A natural question to ask is then whether this difference is predominantly caused by the different cation in the two materials, or whether their atomic structure is the more important parameter. A set of $(In_{1-x}Ga_x)_2O_3$ samples with the bixbyite structure and Ga concentrations varying from 0 to 17.8 % was therefore prepared, and subjected to the same ion irradiation experiment as the pure In_2O_3 and Ga_2O_3 during screening. It was found that all the samples qualitatively behaved similar to In_2O_3, and x-ray diffractometry showed that the irradiation did not change their bixbyite structure. This indicates that the crystal structure plays an important role for the defect concentration dependent resistivity, but to conclude on the relative importance of structure versus composition additional experiments on a broader range of Ga alloy compositions would be necessary.

During this work it was, surprisingly, found that the resistivity of the samples was inversely proportional with the concentration of Ga dopants. Hall effect measurements showed that the reason is twofold, with both the carrier concentration and mobility varying proportionally with the Ga concentration. As Ga is iso-valent with In, no change in carrier concentration should be expected. Also, introducing a high concentration of a foreign element would intuitively be expected to decrease, rather than increase, the mobility, hence this finding also warrants further study.

Chapter 6

Conclusions and further work

This chapter is divided in two sections. The former summarizes the conclusions drawn from the appended papers, while the latter presents suggestions for extending the current work.

6.1 Conclusions

From the material screening experiments it is apparent that both qualitative and quantitative differences exist between wide band gap oxide materials in terms of their dose dependent resistivity. Certain materials, e.g. In_2O_3, exhibits a three-staged resistivity evolution while others, such as Ga_2O_3, displays a less complex behaviour where the resistance increases monotonically with dose. Despite the differences, the behaviour of all the studied materials can be explained by a common model. At doses below $\sim 10^{13}\,\mathrm{cm}^{-2}$ the irradiation induced defect concentration is fairly modest, and will in many cases have only an insignificant effect on the bulk carrier concentration. Dose dependent resistivity changes in this region are attributed to desorption of oxygen related species from the surface, resulting in a recovery of the material's native surface states. At doses between 10^{13} and $\sim 5 \times 10^{14}\,\mathrm{cm}^{-2}$ the increasing resistance is attributed to a buildup of Frenkel pairs with net acceptor-like behaviour, while at even higher doses the change in resistance is caused by the formation of complexes from the individual point defects, e.g. divacancies or antisites. In this model, the observation that certain materials, e.g. SnO_2 and Ga_2O_3, do not show a decreasing resistance at the highest doses is explained by that the complexes forming in these samples are not (sufficiently) donor-like, and hence do not liberate electrons captured by the acceptor-like point defects. The carrier concentration of these samples thus remains low and, consequently, the resistance high.

In In_2O_3, the as-grown Fermi level has two key effects on the dose dependent resistivity. A higher Fermi level in otherwise identical samples will tend to (i) lower the magnitude of the resistance peak and (ii) shift the peak towards higher doses. The lower magnitude is caused by the increased background concentration of electrons which the irradiation induced defects is unable to compensate. The shift along the dose axis arises as a higher concentration of defects must be introduced in order to appreciably influence the carrier concentration. Comparing the change in carrier concentration with simulated corresponding defect concentrations in In_2O_3 the dynamic annealing rate at a temperature of 50 K was estimated as 98.6 %.

In addition to the well established methods of UV-illumination and thermal annealing in vacuum, ion irradiation was found to be an efficient way of removing adsorbed atoms and molecules from the surface of In_2O_3. Irradiation with 3 MeV

Si^{2+} primary ions to an accumulated dose of $10^{13}\,cm^{-2}$ produces a 4 order of magnitude decrease in resistivity, similar to the effect of a 12 hour exposure to 250 nm UV light. Post-irradiation exposure to O_2 gas rapidly increases the resistivity by a factor 5, showing that adsorbed oxygen species do contribute to the electron capture. After the O_2 exposure the resistance is, however, still lower than before the irradiation. Two plausible explanations are that the pure oxygen adsorbates can be weaker electron traps than the species present prior to the irradiation, or that the irradiation has introduced bulk acceptors.

Alloying isovalent Ga_2O_3 into In_2O_3 surprisingly increases both the carrier concentration and mobility of the as-grown samples. This effect persists during irradiation throughout the entirety of the explored dose range. Qualitatively, the dose dependence of the resistivity is similar to that of pure In_2O_3 for Ga concentrations up to at least 17.8 %, and no Ga_2O_3-like behavior was observed.

6.2 Further work

During the course of the presented work, several interesting areas for further investigation were revealed.

Firstly, expanding the material screening presented in Paper I with additional materials would immediately yield further knowledge about the radiation tolerance of the examined materials' electrical properties. Over time such results could be compiled into a database of suitable materials for use when designing radiation tolerant devices.

Further, in order to understand the formation of complexes from individual Frenkel pairs, examining the dose dependent resistivity for a single material as a function of temperature would be interesting. For this experiment, a set of identical samples should be subjected to identical irradiation conditions, with the exception of a different temperature for each sample. Correlating the position of the resistance peak with the temperature, the activation energy for complex formation could possibly be extracted.

Further examination of the relative importance of material structure and composition could be performed by continuing the irradiation experiments on bixbyite $(In_{1-x}Ga_x)_2O_3$ with Ga concentrations $> 17.8\,\%$. Repeating the same experiment with the opposite alloy, i.e. with In introduced into β-Ga_2O_3, would also be highly interesting.

Spectroscopic investigations, by e.g. deep level transient spectroscopy, as a function of irradiation dose on samples supporting the formation of Schottky contacts could potentially identify the relevant defects, thereby serving as an experimental test of the presented model. Formation of reliable rectifying contacts on In_2O_3 has, unfortunately, proven to be a challenge but recent developments have shown that it is indeed possible with the aid of careful surface treatment prior to contact deposition [122].

An open question from Paper III is why the resistivity does not increase to its as-grown value upon post-irradiation exposure to oxygen gas. One hypothesis is that other adsorbates are needed in addition to oxygen, in order to achieve

the as-grown resistivity. A screening of the effect of various gases on the sample resistivity would thus be interesting, and could also be extended to include other semiconductors. A study of the change in surface chemistry before and after various stages of ion irradiation, e.g. by x-ray photoelectron spectroscopy (XPS), would be very valuable in this respect, but should be conducted in situ. Alternatively the sample would have to be transferred inertly between the irradiation chamber and the analysis instrument. For ZnO, a correlation has been found between the surface polarity and the ability to thermally desorb adsorbed hydrogen species [123]. Repeating the cited experiments with ion irradiation as a means of adsorbate removal could deepen the understanding of the effect of the ion beam on surface adsorbates. Further, determining the effect of the primary ion species and -energy on the surface adsorbates could be important for materials intended for use in radiation hard environments.

Bibliography

[1] T. C. Lovejoy, R. Chen, X. Zheng, E. G. Villora, K. Shimamura, H. Yoshikawa, Y. Yamashita, S. Ueda, K. Kobayashi, S. T. Dunham, F. S. Ohuchi, and M. A. Olmstead, "Band bending and surface defects in β-Ga_2O_3," *Applied Physics Letters*, vol. 100, no. 18, p. 181602, 2012.

[2] J. F. Wager, D. A. Keszler, and R. E. Presley, *Transparent Electronics*. Springer Science+Business Media New York, 2008.

[3] R. G. Gordon, "Criteria for Choosing Transparent Conductors," *MRS Bulletin*, vol. 25, pp. 52–57, Aug. 2000.

[4] D. S. Ginley and J. D. Perkins, "Transparent Conductors," in *Handbook of Transparent Conductors* (D. S. Ginley, ed.), pp. 1–25, Springer US, 2011. DOI: 10.1007/978-1-4419-1638-9_1.

[5] R. A. Afre, N. Sharma, M. Sharon, and M. Sharon, "Transparent conducting oxide films for various applications: A review," *Reviews on advanced materials science*, vol. 53, no. 1, pp. 79 – 89, 2018.

[6] M. Morales-Masis, S. De Wolf, R. Woods-Robinson, J. W. Ager, and C. Ballif, "Transparent electrodes for efficient optoelectronics," *Advanced Electronic Materials*, vol. 3, no. 5, p. 1600529, 2017.

[7] T. Tsujimura, *OLED Display Structure*, ch. 2, pp. 5–35. John Wiley & Sons, Ltd, 2012.

[8] P. Barquinha, R. Martins, L. Pereira, and E. Fortunato, *Transparent Oxide Electronics: From Materials to Devices*. Chichester, UK: John Wiley & Sons, Ltd, 2012.

[9] W.-C. Hong, C.-J. Ku, R. Li, S. Abbaslou, P. Reyes, S.-Y. Wang, G. Li, M. Lu, K. Sheng, and Y. Lu, "MgZnO High Voltage Thin Film Transistors on Glass for Inverters in Building Integrated Photovoltaics," *Scientific Reports*, vol. 6, p. 34169, Oct. 2016.

[10] J. Rombach, A. Papadogianni, M. Mischo, V. Cimalla, L. Kirste, O. Ambacher, T. Berthold, S. Krischok, M. Himmerlich, S. Selve, and O. Bierwagen, "The role of surface electron accumulation and bulk doping for gas-sensing explored with single-crystalline In_2O_3 thin films," *Sensors and Actuators B: Chemical*, vol. 236, pp. 909 – 916, 2016.

[11] S. J. Pearton, F. Ren, M. Tadjer, and J. Kim, "Perspective: Ga_2O_3 for ultra-high power rectifiers and MOSFETS," *Journal of Applied Physics*, vol. 124, no. 22, p. 220901, 2018.

[12] Y. Kanai, "Electrical properties of indium- tin-oxide single crystals," *Japanese journal of applied physics*, vol. 23, pp. L12–L14, jan 1984.

[13] Y. Kanai, "Electronic conduction in Mg doped In_2O_3 single crystals," *Japanese journal of applied physics*, vol. 24, pp. L361–L363, may 1985.

[14] Y. K. Frodason, K. M. Johansen, A. Alkauskas, and L. Vines, "Negative-U and polaronic behavior of the Zn-O divacancy in ZnO," *Phys. Rev. B*, vol. 99, p. 174106, May 2019.

[15] P. Erhart and K. Albe, "Diffusion of zinc vacancies and interstitials in zinc oxide," *Applied Physics Letters*, vol. 88, no. 20, p. 201918, 2006.

[16] J. Fan, K. Sreekanth, Z. Xie, S. Chang, and K. Rao, "P-type ZnO materials: Theory, growth, properties and devices," *Progress in Materials Science*, vol. 58, no. 6, pp. 874–985, 2013.

[17] S. Lany, J. Osorio-Guillén, and A. Zunger, "Origins of the doping asymmetry in oxides: Hole doping in NiO versus electron doping in ZnO," *Physical Review B*, vol. 75, p. 241203, June 2007.

[18] Y. Tsur and I. Riess, "Self-compensation in semiconductors," *Physical Review B*, vol. 60, pp. 8138–8146, Sept. 1999.

[19] A. Zunger, "Practical doping principles," *Applied Physics Letters*, vol. 83, pp. 57–59, June 2003.

[20] P. Reunchan, X. Zhou, S. Limpijumnong, A. Janotti, and C. G. Van de Walle, "Vacancy defects in indium oxide: An ab-initio study," *Current Applied Physics*, vol. 11, pp. S296–S300, May 2011.

[21] P. Ágoston, K. Albe, R. M. Nieminen, and M. J. Puska, "Intrinsic *n*-type behavior in transparent conducting oxides: A comparative hybrid-functional study of In_2O_3, SnO_2, and ZnO," *Phys. Rev. Lett.*, vol. 103, p. 245501, Dec 2009.

[22] J. Buckeridge, C. R. A. Catlow, M. R. Farrow, A. J. Logsdail, D. O. Scanlon, T. W. Keal, P. Sherwood, S. M. Woodley, A. A. Sokol, and A. Walsh, "Deep vs shallow nature of oxygen vacancies and consequent *n*-type carrier concentrations in transparent conducting oxides," *Phys. Rev. Materials*, vol. 2, p. 054604, May 2018.

[23] I. Chatratin, F. P. Sabino, P. Reunchan, S. Limpijumnong, J. B. Varley, C. G. Van de Walle, and A. Janotti, "Role of point defects in the electrical and optical properties of In_2O_3," *Phys. Rev. Materials*, vol. 3, p. 074604, July 2019.

[24] H. von Wenckstern, D. Splith, F. Schmidt, M. Grundmann, O. Bierwagen, and J. S. Speck, "Schottky contacts to In_2O_3," *APL Materials*, vol. 2, p. 046104, Apr. 2014.

[25] H. von Wenckstern, "Group-III sesquioxides: Growth, physical properties and devices," *Advanced Electronic Materials*, vol. 3, no. 9, p. 1600350, 2017.

[26] M.-S. Lee, Won Chel Choi, Eun Kyu Kim, Chun Keun Kim, and S.-K. Min, "Characterization of the oxidized indium thin films with thermal oxidation," *Thin Solid Films*, vol. 279, no. 1, pp. 1–3, 1996.

[27] G. Korotcenkov, M. Nazarov, M. V. Zamoryanskaya, and M. Ivanov, "Cathodoluminescence emission study of nanocrystalline indium oxide films deposited by spray pyrolysis," *Thin Solid Films*, vol. 515, pp. 8065–8071, July 2007.

[28] A. El Hichou, M. Addou, M. Mansori, and J. Ebothé, "Structural, optical and luminescent characteristics of sprayed fluorine-doped In_2O_3 thin films for solar cells," *Solar Energy Materials and Solar Cells*, vol. 93, pp. 609–612, May 2009.

[29] N. W. Ashcroft and N. D. Mermin, *Solid state physics*. Saunders college publishing, 1976.

[30] C. Kittel, *Introduction to solid state physics*. Wiley, 8th ed., 2005.

[31] B. G. Streetman and S. K. Banerjee, *Solid state electronic devices*. Pearson Prentice-Hall, sixth ed., 2006.

[32] R. J. D. Tilley, *Understanding solids: the science of materials*. John Wiley & Sons Ltd, 2004.

[33] K. Momma and F. Izumi, "*VESTA3* for three-dimensional visualization of crystal, volumetric and morphology data," *Journal of Applied Crystallography*, vol. 44, pp. 1272–1276, Dec 2011.

[34] E. G. Seebauer and K. W. Noh, "Trends in semiconductor defect engineering at the nanoscale," *Materials Science and Engineering: R: Reports*, vol. 70, no. 3, pp. 151–168, 2010. 3rd IEEE International NanoElectronics Conference (INEC).

[35] D. J. Griffiths, *Introduction to Quantum Mechanics*. Pearson Prentice Hall, second ed., 2005.

[36] L. D. Whalley, J. M. Frost, B. J. Morgan, and A. Walsh, "Impact of nonparabolic electronic band structure on the optical and transport properties of photovoltaic materials," *Phys. Rev. B*, vol. 99, p. 085207, Feb 2019.

[37] E. O. Kane, "Band structure of indium antimonide," *Journal of Physics and Chemistry of Solids*, vol. 1, pp. 249–261, Jan. 1957.

[38] T. Pisarkiewicz and A. Kolodziej, "Nonparabolicity of the conduction band structure in degenerate tin dioxide," *physica status solidi (b)*, vol. 158, no. 1, pp. K5–K8, 1990.

[39] M. Feneberg, J. Nixdorf, C. Lidig, R. Goldhahn, Z. Galazka, O. Bierwagen, and J. S. Speck, "Many-electron effects on the dielectric function of cubic In_2O_3: Effective electron mass, band nonparabolicity, band gap renormalization, and Burstein-Moss shift," *Phys. Rev. B*, vol. 93, p. 045203, Jan 2016.

[40] N. G. Nilsson, "An accurate approximation of the generalized einstein relation for degenerate semiconductors," *physica status solidi (a)*, vol. 19, pp. K75–K78, Sept. 1973.

[41] W. B. Joyce and R. W. Dixon, "Analytic approximations for the Fermi energy of an ideal Fermi gas," *Applied Physics Letters*, vol. 31, p. 354, 1977.

[42] R. Kim and M. Lundstrom, "Notes on Fermi-Dirac integrals 3rd edition." https://arxiv.org/abs/0811.0116v4, 2011.

[43] Y. K. Frodason, K. M. Johansen, T. S. Bjørheim, B. G. Svensson, and A. Alkauskas, "Zn vacancy as a polaronic hole trap in ZnO," *Phys. Rev. B*, vol. 95, p. 094105, Mar 2017.

[44] W. Walukiewicz, "Mechanism of Schottky barrier formation: The role of amphoteric native defects," *Journal of Vacuum Science & Technology B: Microelectronics Processing and Phenomena*, vol. 5, no. 4, pp. 1062–1067, 1987.

[45] W. Walukiewicz, "Mechanism of Fermi-level stabilization in semiconductors," *Physical Review B*, vol. 37, pp. 4760–4763, Mar. 1988.

[46] W. Walukiewicz, "Fermi level dependent native defect formation: Consequences for metal–semiconductor and semiconductor–semiconductor interfaces," *Journal of Vacuum Science & Technology B: Microelectronics Processing and Phenomena*, vol. 6, no. 4, pp. 1257–1262, 1988.

[47] J. Tersoff, "Theory of semiconductor heterojunctions: The role of quantum dipoles," *Phys. Rev. B*, vol. 30, pp. 4874–4877, Oct 1984.

[48] A. Schleife, F. Fuchs, C. Rödl, J. Furthmüller, and F. Bechstedt, "Branch-point energies and band discontinuities of III-nitrides and III-/II-oxides from quasiparticle band-structure calculations," *Applied Physics Letters*, vol. 94, p. 012104, Jan. 2009.

[49] W. Mönch, "On the band structure lineup of ZnO heterostructures," *Applied Physics Letters*, vol. 86, p. 162101, Apr. 2005.

[50] J. Robertson, "Interface states model for III–V oxide interfaces," *Microelectronic Engineering*, vol. 86, pp. 1558–1560, July 2009.

[51] B. Falabretti and J. Robertson, "Electronic structures and doping of SnO_2, $CuAlO_2$, and $CuInO_2$," *Journal of Applied Physics*, vol. 102, p. 123703, Dec. 2007.

[52] C. G. Van de Walle and J. Neugebauer, "Universal alignment of hydrogen levels in semiconductors, insulators and solutions," *Nature*, vol. 423, pp. 626–628, June 2003.

[53] J. Robertson, K. Xiong, and S. J. Clark, "Band gaps and defect levels in functional oxides," *Thin Solid Films*, vol. 496, pp. 1–7, Feb. 2006.

[54] P. D. C. King, T. D. Veal, D. J. Payne, A. Bourlange, R. G. Egdell, and C. F. McConville, "Surface Electron Accumulation and the Charge Neutrality Level in In_2O_3," *Physical Review Letters*, vol. 101, p. 116808, Sept. 2008.

[55] L. Vines, C. Bhoodoo, H. von Wenckstern, and M. Grundmann, "Electrical conductivity of In_2O_3 and Ga_2O_3 after low temperature ion irradiation; implications for instrinsic defect formation and charge neutrality level," *Journal of Physics: Condensed Matter*, vol. 30, no. 2, p. 025502, 2018.

[56] S. O. Kucheyev, P. N. K. Deenapanray, C. Jagadish, J. S. Williams, M. Yano, K. Koike, S. Sasa, M. Inoue, and K.-i. Ogata, "Electrical isolation of ZnO by ion bombardment," *Applied Physics Letters*, vol. 81, pp. 3350–3352, Oct. 2002.

[57] K. Bädeker, "Über die elektrische Leitfähigkeit und die thermoelektrische kraft einiger schwermetallverbindungen," *Annalen der Physik (Leipzig)*, 1907.

[58] C. I. Bright, "Review of transparent conductive oxides (TCO)," in *50 Years of Vacuum Coating Technology and the Growth of the Society of Vacuum Coaters* (D. M. Mattox and V. H. Mattox, eds.), ch. 7, Society of Vacuum Coaters, 2007.

[59] S. K. Vasheghani Farahani, T. D. Veal, P. D. C. King, J. Zúñiga-Pérez, V. Muñoz-Sanjosé, and C. F. McConville, "Electron mobility in CdO films," *Journal of Applied Physics*, vol. 109, no. 7, p. 073712, 2011.

[60] M. Yan, M. Lane, C. R. Kannewurf, and R. P. H. Chang, "Highly conductive epitaxial CdO thin films prepared by pulsed laser deposition," *Applied Physics Letters*, vol. 78, no. 16, pp. 2342–2344, 2001.

[61] S. Das and V. Jayaraman, "SnO_2: A comprehensive review on structures and gas sensors," *Progress in Materials Science*, vol. 66, pp. 112 – 255, 2014.

[62] E. R. Caley, "The action of hydriodic acid on stannic oxide," *Journal of the American Chemical Society*, vol. 54, no. 8, pp. 3240–3243, 1932.

[63] H. A. McMaster, "Conductive coating for glass and method of application," US Patent No: 2429420, Oct. 1942.

[64] K. Bejtka, J. Zeng, A. Sacco, M. Castellino, S. Hernández, M. A. Farkhondehfal, U. Savino, S. Ansaloni, C. F. Pirri, and A. Chiodoni, "Chainlike mesoporous SnO_2 as a well-performing catalyst for electrochemical CO_2 reduction," *ACS Applied Energy Materials*, vol. 2, no. 5, pp. 3081–3091, 2019.

[65] U. Özgür, Y. I. Alivov, C. Liu, A. Teke, M. A. Reshchikov, S. Doğan, V. Avrutin, S.-J. Cho, and H. Morkoc, "A comprehensive review of ZnO materials and devices," *Journal of Applied Physics*, vol. 98, no. 4, p. 041301, 2005.

[66] N. Kamarulzaman, M. F. Kasim, and R. Rusdi, "Band gap narrowing and widening of ZnO nanostructures and doped materials," *Nanoscale Research Letters*, vol. 10, p. 346, Aug. 2015.

[67] C. W. Bunn, "The lattice-dimensions of zinc oxide," *Proceedings of the Physical Society*, vol. 47, pp. 835–842, sep 1935.

[68] K. Wasa, S. Hayakawa, and T. Hada, "Electrical and optical properties of sputtered n-pZnO-Si heterojunctions," *Japanese Journal of Applied Physics*, vol. 10, pp. 1732–1732, dec 1971.

[69] S.-M. Park, T. Ikegami, and K. Ebihara, "Effects of substrate temperature on the properties of Ga-doped ZnO by pulsed laser deposition," *Thin Solid Films*, vol. 513, no. 1, pp. 90–94, 2006.

[70] A. Suzuki, T. Matsushita, T. Aoki, Y. Yoneyama, and M. Okuda, "Pulsed laser deposition of transparent conducting indium tin oxide films in magnetic field perpendicular to plume," *Japanese Journal of Applied Physics*, vol. 40, no. Part 2, No. 4B, pp. L401–L403, 2001.

[71] R. Roy, V. G. Hill, and E. F. Osborn, "Polymorphism of Ga_2O_3 and the system Ga_2O_3–H_2O," *J. Am. Chem. Soc.*, vol. 74, pp. 719–722, Feb. 1952.

[72] M. Higashiwaki and G. H. Jessen, "Guest editorial: The dawn of gallium oxide microelectronics," *Appl. Phys. Lett.*, vol. 112, p. 060401, May 2018.

[73] C. Buttay, D. Planson, B. Allard, D. Bergogne, P. Bevilacqua, C. Joubert, M. Lazar, C. Martin, H. Morel, D. Tournier, and C. Raynaud, "State of the art of high temperature power electronics," *Materials Science and Engineering: B*, vol. 176, pp. 283–288, Mar. 2011.

[74] M. J. Zunick, "Conductive coating on glass," US Patent No: 2516663, Sept. 1947.

[75] G. Rupprecht, "Untersuchungen der elektrischen und lichtelektrischen Leitfähigkeit dünner Indiumoxydschichten," *Zeitschrift für Physik*, vol. 139, pp. 504–517, Oct. 1954.

[76] D. B. Fraser and H. D. Cook, "Highly conductive, transparent films of sputtered $In_{2-x}Sn_xO_{3-y}$," *Journal of The Electrochemical Society*, vol. 119, no. 10, p. 1368, 1972.

[77] F. Fuchs and F. Bechstedt, "Indium-oxide polymorphs from first principles: Quasiparticle electronic states," *Physical Review B*, vol. 77, p. 155107, Apr. 2008.

[78] O. Bierwagen, "Indium oxide–a transparent, wide-band gap semiconductor for (opto)electronic applications," *Semiconductor Science and Technology*, vol. 30, no. 2, p. 024001, 2015.

[79] P. D. C. King, T. D. Veal, F. Fuchs, C. Y. Wang, D. J. Payne, A. Bourlange, H. Zhang, G. R. Bell, V. Cimalla, O. Ambacher, R. G. Egdell, F. Bechstedt, and C. F. McConville, "Band gap, electronic structure, and surface electron accumulation of cubic and rhombohedral In_2O_3," *Physical Review B*, vol. 79, p. 205211, May 2009.

[80] R. L. Weiher and R. P. Ley, "Optical properties of indium oxide," *Journal of Applied Physics*, vol. 37, pp. 299–302, May 1966.

[81] F. Matino, L. Persano, V. Arima, D. Pisignano, R. I. R. Blyth, R. Cingolani, and R. Rinaldi, "Electronic structure of indium-tin-oxide films fabricated by reactive electron-beam deposition," *Phys. Rev. B*, vol. 72, p. 085437, Aug 2005.

[82] P. Erhart, A. Klein, R. G. Egdell, and K. Albe, "Band structure of indium oxide: Indirect versus direct band gap," *Phys. Rev. B*, vol. 75, p. 153205, Apr 2007.

[83] O. Bierwagen and J. S. Speck, "Plasma-assisted molecular beam epitaxy of Sn-doped In_2O_3: Sn incorporation, structural changes, doping limits, and compensation," *Phys. Status Solidi A*, vol. 211, pp. 48–53, May 2014.

[84] H. L. Kwok, *Electronic materials*. PWS publishing company, 1997.

[85] U. Bruno, "Employment of pulsed-laser deposition for optoelectronic device fabrication," in *Optoelectronic Devices and Properties* (O. Sergiyenko, ed.), ch. 26, Rijeka: IntechOpen, 2011.

[86] S. N. Ogugua, O. M. Ntwaeaborwa, and H. C. Swart, "Latest development on pulsed laser deposited thin films for advanced luminescence applications," *Coatings*, vol. 10, no. 11, 2020.

[87] H. von Wenckstern, M. Kneiß, A. Hassa, P. Storm, D. Splith, and M. Grundmann, "A review of the segmented-target approach to combinatorial material synthesis by pulsed-laser deposition," *physica status solidi (b)*, vol. 257, no. 7, p. 1900626, 2020.

[88] D. M. Mattox, *Handbook of physical vapor deposition (PVD) processing*. Elsevier, second ed., 2010.

[89] S. A. Campbell, *Fabrication engineering at the micro- and nanoscale*. Oxford university press, fourth ed., 2008.

[90] G. Dearnaley, J. H. Freeman, R. S. Nelson, and J. Stephen, *Ion implantation*. Defects in crystalline solids, North-Holland publishing company, 1973.

[91] D. K. Avasthi and G. K. Mehta, *Swift Heavy Ions for Materials Engineering and Nanostructuring*, vol. 145 of *Springer Series in Materials Science*. Dordrecht: Springer Netherlands, 2011.

[92] Y. Zhang, I.-T. Bae, K. Sun, C. Wang, M. Ishimaru, Z. Zhu, W. Jiang, and W. J. Weber, "Damage profile and ion distribution of slow heavy ions in compounds," *Journal of Applied Physics*, vol. 105, no. 10, p. 104901, 2009.

[93] A. Hupfer, C. Bhoodoo, L. Vines, and B. G. Svensson, "Formation and annihilation of E4 centers in ZnO: Influence of hydrogen," *Journal of Applied Physics*, vol. 119, no. 18, p. 181506, 2016.

[94] S. O. Kucheyev, J. S. Williams, C. Jagadish, J. Zou, C. Evans, A. J. Nelson, and A. V. Hamza, "Ion-beam-produced structural defects in ZnO," *Physical Review B*, vol. 67, p. 094115, Mar. 2003.

[95] B. G. Svensson, C. Jagadish, and J. S. Williams, "Generation rate of point defects in silicon irradiated by MeV ions," *Nuclear Instruments and Methods in Physics Research Section B: Beam Interactions with Materials and Atoms*, vol. 80-81, pp. 583–586, 1993.

[96] N. F. Mott, "The theory of crystal rectifiers," *Proceedings of the Royal Society of London. Series A. Mathematical and Physical Sciences*, vol. 171, no. 944, pp. 27–38, 1939.

[97] S. M. Sze and K. K. Ng, *Physics of semiconductor devices*. Wiley Interscience, 3rd ed., 2007.

[98] L. J. van der Pauw, "A method of measuring the resistivity and Hall coefficient of lamellae of arbitrary shape," *Philips technical review*, vol. 20, p. 220, 1958.

[99] B. G. Streetman, *Solid state electronic devices*. Prentice Hall, second ed., 1980.

[100] D. K. Schroder, *Semiconductor material and device characterization*. IEEE Press Wiley, third ed., 2006.

[101] K. Ellmer, "Resistivity of polycrystalline zinc oxide films: current status and physical limit," *Journal of Physics D: Applied Physics*, vol. 34, pp. 3097–3108, oct 2001.

[102] M. Birkholz, *Thin film analysis by x-ray scanning*. Wiley-VCH, 2006.

[103] A. L. Patterson, "The Scherrer formula for x-ray particle size determination," *Phys. Rev.*, vol. 56, pp. 978–982, Nov 1939.

[104] B. G. Yacobi and D. B. Holt, "Cathodoluminescence scanning electron microscopy of semiconductors," *Journal of Applied Physics*, vol. 59, no. 4, pp. R1–R24, 1986.

[105] T. Coenen and N. M. Haegel, "Cathodoluminescence for the 21st century: Learning more from light," *Applied Physics Reviews*, vol. 4, no. 3, p. 031103, 2017.

[106] A. Rothwarf, "Plasmon theory of electron-hole pair production: efficiency of cathode ray phosphors," *Journal of Applied Physics*, vol. 44, no. 2, pp. 752–756, 1973.

[107] P. K. Basu, "Excitonic absorption," in *Theory of optical processes in semiconductors: Bulk and microstructures*, ch. 9, Oxford university press, 2003.

[108] P. K. Basu, "Free-carrier processes," in *Theory of optical processes in semiconductors: Bulk and microstructures*, ch. 6, Oxford university press, 2003.

[109] J. F. Muth, J. H. Lee, I. K. Shmagin, R. M. Kolbas, H. C. Casey, B. P. Keller, U. K. Mishra, and S. P. DenBaars, "Absorption coefficient, energy gap, exciton binding energy, and recombination lifetime of GaN obtained from transmission measurements," *Applied Physics Letters*, vol. 71, no. 18, pp. 2572–2574, 1997.

[110] B. D. Viezbicke, S. Patel, B. E. Davis, and D. P. Birnie, "Evaluation of the Tauc method for optical absorption edge determination: ZnO thin films as a model system," *physica status solidi (b)*, vol. 252, pp. 1700–1710, Aug. 2015.

[111] D. S. Sholl and J. A. Steckel, *Density Functional Theory: A Practical Introduction*. John Wiley & Sons, 2009.

[112] J. P. Perdew, K. Burke, and M. Ernzerhof, "Generalized gradient approximation made simple," *Physical Review Letters*, vol. 77, pp. 3865–3868, Oct 1996.

[113] A. V. Krukau, O. A. Vydrov, A. F. Izmaylov, and G. E. Scuseria, "Influence of the exchange screening parameter on the performance of screened hybrid functionals," *The Journal of Chemical Physics*, vol. 125, no. 22, p. 224106, 2006.

[114] F. Oba, A. Togo, I. Tanaka, J. Paier, and G. Kresse, "Defect energetics in ZnO: A hybrid Hartree-Fock density functional study," *Phys. Rev. B*, vol. 77, p. 245202, Jun 2008.

[115] P. D. C. King, R. L. Lichti, Y. G. Celebi, J. M. Gil, R. C. Vilão, H. V. Alberto, J. Piroto Duarte, D. J. Payne, R. G. Egdell, I. McKenzie, C. F. McConville, S. F. J. Cox, and T. D. Veal, "Shallow donor state of hydrogen in In_2O_3 and SnO_2: Implications for conductivity in transparent conducting oxides," *Phys. Rev. B*, vol. 80, p. 081201, Aug 2009.

[116] J. E. N. Swallow, J. B. Varley, L. A. H. Jones, J. T. Gibbon, L. F. J. Piper, V. R. Dhanak, and T. D. Veal, "Transition from electron accumulation to depletion at β-Ga_2O_3 surfaces: The role of hydrogen and the charge neutrality level," *APL Materials*, vol. 7, no. 2, p. 022528, 2019.

[117] D. K. Schroder, R. N. Thomas, and J. C. Swartz, "Free carrier absorption in silicon," *IEEE Journal of Solid-state Circuits*, vol. SC-13, no. 1, p. 180, 1978.

[118] J. Olley, "Structural disorder and the Urbach edge," *Solid State Communications*, vol. 13, no. 9, pp. 1437 – 1440, 1973.

[119] J. Nelson, *The Physics of Solar Cells*. Imperial College Press, 2003.

[120] J. F. Ziegler, J. P. Biersack, and U. Littmark, *The stopping and range of ions in solids*. Pergamon Press, New York, 1985.

[121] M. Bender, N. Katsarakis, E. Gagaoudakis, E. Hourdakis, E. Douloufakis, V. Cimalla, and G. Kiriakidis, "Dependence of the photoreduction and oxidation behavior of indium oxide films on substrate temperature and film thickness," *Journal of Applied Physics*, vol. 90, no. 10, pp. 5382–5387, 2001.

[122] J. Michel, D. Splith, J. Rombach, A. Papadogianni, T. Berthold, S. Krischok, M. Grundmann, O. Bierwagen, H. von Wenckstern, and M. Himmerlich, "Processing strategies for high-performance Schottky contacts on n-type oxide semiconductors: Insights from In_2O_3," *ACS Appl. Mater. Interfaces*, vol. 11, no. 30, pp. 27073–27087, 2019.

[123] R. Heinhold, G. T. Williams, S. P. Cooil, D. A. Evans, and M. W. Allen, "Influence of polarity and hydroxyl termination on the band bending at ZnO surfaces," *Phys. Rev. B*, vol. 88, p. 235315, Dec 2013.

Papers

Paper I

Experimental exploration of the amphoteric defect model by cryogenic irradiation of a range of wide band gap oxide materials

OPEN ACCESS
IOP Publishing
Journal of Physics: Condensed Matter
J. Phys.: Condens. Matter **32** (2020) 415704 (12pp)
https://doi.org/10.1088/1361-648X/abac8b

Experimental exploration of the amphoteric defect model by cryogenic ion irradiation of a range of wide band gap oxide materials

J Borgersen[1,2,6], L Vines[1,2], Y K Frodason[1,2], A Kuznetsov[1,2], H von Wenckstern[3], M Grundmann[3], M Allen[4], J Zúñiga-Pérez[5] and K M Johansen[1,2]

[1] Department of Physics, University of Oslo, Norway
[2] Centre for Materials Science and Nanotechnology, University of Oslo, Norway
[3] Felix Bloch institute for Solid State Physics, Fakultät für Physik und Geowissenschaften, Universität Leipzig, Germany
[4] Department of Electrical and Computer Engineering, University of Canterbury, New Zealand
[5] Centre de Recherche sur l'Hétéro-Epitaxie et ses Applications (CRHEA), CNRS, Université Côte d'Azur, France

E-mail: jonborg@fys.uio.no

Received 5 May 2020, revised 9 July 2020
Accepted for publication 5 August 2020
Published 21 September 2020

Abstract

The evolution of electrical resistance as function of defect concentration is examined for the unipolar *n*-conducting oxides CdO, β-Ga_2O_3, In_2O_3, SnO_2 and ZnO in order to explore the predictions of the amphoteric defect model. Intrinsic defects are introduced by ion irradiation at cryogenic temperatures, and the resistance is measured in-situ by current–voltage sweeps as a function of irradiation dose. Temperature dependent Hall effect measurements are performed to determine the carrier concentration and mobility of the samples before and after irradiation. After the ultimate irradiation step, the Ga_2O_3 and SnO_2 samples have both turned highly resistive. In contrast, the In_2O_3 and ZnO samples are ultimately found to be less resistive than prior to irradiation, however, they both show an increased resistance at intermediate doses. Based on thermodynamic defect charge state transitions computed by hybrid density functional theory, a model expanding on the current amphoteric defect model is proposed.

Keywords: Ga_2O_3, In_2O_3, defect, irradiation, amphoteric defect model

Supplementary material for this article is available online

(Some figures may appear in colour only in the online journal)

1. Introduction

The wide band gap semiconducting oxide materials exhibit a plethora of interesting properties, including optical transparency, high electrical conductivity and breakdown field strength, piezoelectricity etc., making them highly desirable in a range of devices [1–5]. Several electrical properties of these materials, e.g. the maximum achievable carrier concentration, surface accumulation/depletion of electrons and propensity for either *p*- or *n*-type doping are related to their intrinsic and extrinsic defects [6]. Fundamental knowledge of the defects and their behaviour is thus of scientific interest, and also paramount for device fabrication.

A model frequently used for describing the formation of intrinsic defects in semiconductors is the amphoteric defect

[6] Author to whom any correspondence should be addressed.

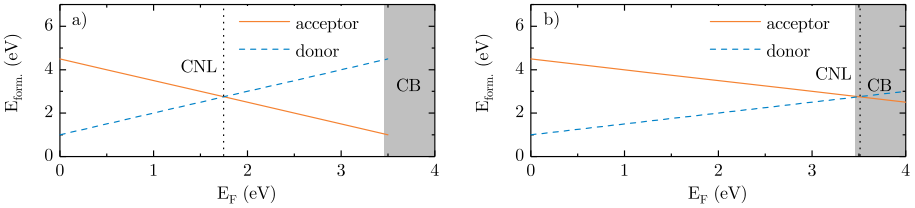

Figure 1. Generic formation energies for an intrinsic donor and acceptor as function of Fermi level relative to the valence band. The shaded bar on the right illustrates the conduction band. The charge neutrality level (CNL) lies at the intersection between the donor and the acceptor formation energies and is shown as a dotted line. Two cases are illustrated, (a) a conventional semiconductor with the CNL close to midgap, and (b) a material with the CNL within the conduction band.

model (ADM) [7]. One of the main assumptions of the model is that a native defect generally can exist in several charge states, and may act either as a donor or as an acceptor (amphoteric behaviour). Furthermore, the charge state of a defect is governed by the Fermi level (E_F) and its probability of formation is determined by the formation energy. For donor states, the formation energy increases with E_F while the converse is true for acceptors. As the electrical effect of a donor (acceptor) is to increase (decrease) the Fermi level, introduction of intrinsic defects tends to shift E_F towards a level referred to as the charge neutrality level (CNL). In other words, if $E_F <$ CNL donor like states will preferentially form, whereas if $E_F >$ CNL acceptor like states will be favoured. On an energy scale, the CNL is located at the point where the formation energy of the most stable intrinsic donor equals that of the most stable intrinsic acceptor, as shown for a typical wide band gap material in figure 1(a). For illustrative purposes, the figure shows a single donor and acceptor pair having the lowest formation energies throughout the band gap. In practice this need not be the case and several defects may dominate in various regions of the gap. If a sufficiently high defect concentration is introduced, the Fermi level is pinned at the CNL and further generation of defects will not yield any net change in the carrier concentration.

The CNL of a material can be estimated by several theoretical approaches, and quantitatively the predicted position will depend on the details of the computation. One approach is to calculate the formation energies of all relevant intrinsic defects and, in line with the above reasoning, estimate the CNL as lying at the intersection of the formation energies of the dominant donor and acceptor states [8]. The defect states tend to be highly localized in real space and thus have an extended character in *k*-space. Consequently, a different route to obtaining the CNL is to calculate the energies of the valence and conduction band edges at all points of the Brillouin zone (BZ). From the band edges the local band gap at all points of the BZ can be determined, and by averaging the midgap value across the BZ an estimate of the CNL is obtained [9–11]. In practical calculations a choice of the relevant *k*-points at which to evaluate the band edges must be made. Several schemes are discussed in [12] and references therein. As a side note, it has been found that the donor/acceptor transition level of hydrogen can also be used as an estimate of the CNL in many materials [13].

For materials where both the valence and conduction band have low dispersion throughout the Brillouin zone the averaged midgap energy discussed above is close to the middle of the fundamental band gap, E_g, defined as the energy difference between the conduction band minimum (CBM) and valence band maximum (VBM). Most conventional semiconductors, including Si, Ge, and most binary III-Vs fit this description, and consequently their CNLs are found to lie well within the band gap as illustrated in figure 1(a) [7, 11, 13–15].

Interestingly, density functional theory (DFT) computations have predicted that certain more ionic materials, e.g. CdO, InN, In_2O_3, SnO_2 and ZnO should, due to significant dispersion of their conduction bands, have CNLs above their respective conduction band minima, as illustrated in figure 1(b). This would allow the existence of high carrier concentrations before the introduced defects begin to self compensate the material, thereby partly explaining their surprisingly high conductivities [12, 16, 17]. For CdO and In_2O_3 these predictions have found experimental support by x-ray photoelectron spectroscopy, infrared reflectivity and Hall effect measurements of doped or room temperature ion irradiated samples, indicating that the intrinsic defects are donors even when the samples are heavily *n*-type [9, 10, 18].

A recent report [19] on the electrical properties of low temperature ion irradiated In_2O_3, however, shows indications of a more complex defect evolution than what was found earlier [10]. Also, a range of elements implanted in ZnO at room temperature or above have all been found to considerably increase the resistivity of the samples, in contrast to the predicted behaviour for a material with the charge neutrality level positioned within the conduction band [20, 21].

These discrepancies merit further studies of the defect evolution in semiconducting oxide materials and in this work we investigate and compare the influence of defect concentration on the electrical properties of CdO, β-Ga_2O_3, In_2O_3, SnO_2 and ZnO thin films. Controlled defect concentrations are introduced by low temperature ion irradiation, i.e. ion implantation at energies sufficient for allowing the incident ions to travel through the film of interest and into the substrate. This leaves a cascade of controllable concentration of intrinsic defects in the thin-film material of interest. At select doses, the resistivity of the sample is probed by *in situ* current–voltage (*IV*) measurements. Correlating these measurements with defect

Table 1. Deposition technique, nominal film thickness, substrate material, dimensions, dopant as well as room temperature carrier concentration before ($n_{\text{as dep.}}$) and after ($n_{\text{irr.}}$) irradiation for all the examined samples. For the deposition techniques, MBE refers to molecular beam epitaxy, while PLD refers to pulsed laser deposition.

Material	Deposition	Thickness (nm)	Substrate	Size (mm)	Dopant	$n_{\text{as dep.}}$ (cm^{-3})	$n_{\text{irr.}}$ (cm^{-3})
CdO	MBE	150	r-Al_2O_3	5×5	none	1.5×10^{19}	1.6×10^{20}
Ga_2O_3	PLD	600	c-Al_2O_3	10×10	1% Si	9.5×10^{18}	—
In_2O_3	PLD	800	c-Al_2O_3	10×10	none	1.1×10^{19}	6.0×10^{19}
SnO_2	MBE	150	r-Al_2O_3	5×5	Sb	2.0×10^{18}	—
ZnO	MBE	180	c-Al_2O_3	5×5	none	1.6×10^{17}	4.6×10^{18}

charge states and transition levels calculated by hybrid density functional theory we propose a defect generation model which expands on the previously introduced amphoteric defect model.

2. Experiments

Semiconducting CdO, Ga_2O_3, In_2O_3, SnO_2 and ZnO films of thickness in the range of 150–800 nm were grown on c- or r-plane sapphire substrates by pulsed laser deposition (PLD) or molecular beam epitaxy (MBE), as summarized in table 1. The CdO, In_2O_3 and ZnO films were nominally undoped, while the Ga_2O_3 and SnO_2 samples were doped with Si or Sb, respectively. 100 nm thick aluminium contacts were deposited on top of 10 nm titanium adhesion layers in each corner of the samples. The depositions were made by electron beam evaporation in an Angstrom Engineering EvoVac loaded with metal pellets of at least 99.99% purity. The base pressure before starting the evaporation was 2×10^{-6} torr, and the Ti and Al were deposited sequentially without breaking vacuum.

Prior to irradiation, temperature dependent Hall effect measurements were conducted in the van der Pauw geometry using a Lakeshore 7604 Hall measurement system. The applied magnetic field was 10 kG, and all samples were measured over a temperature range from 20 to 300 K in steps of 10 K. The Hall scattering factor was assumed to be unity for all measurements.

For the ion irradiation, Si^{2+} ions were accelerated to an energy of 3 MeV in an NEC Tandem ion implanter. The implantation chamber was evacuated to $<5 \times 10^{-7}$ torr and, in order to limit defect diffusion and dynamic annealing, the samples were cooled to 50 K (Ga_2O_3 and In_2O_3) or 70 K (CdO, SnO_2 and ZnO) using a closed cycle helium cryostat. From Monte Carlo simulations using the SRIM code [22], the ions are predicted to have a projected range of approximately 1.5 μm, i.e. well within the substrate for all samples, and this was verified using secondary ion mass spectrometry. Any observed changes in the films should thus be caused only by the intrinsic defects induced by the ion beam, and not by the silicon ions. *IV* measurements were performed across the surface diagonal of the samples at a range of irradiation doses up to 3×10^{16} cm^{-2} (CdO, SnO_2, ZnO) or 10^{17} cm^{-2} (Ga_2O_3, In_2O_3) with a Keithley 6487 voltage source/picoammeter using bias voltages in the range $(+/-)$ 2 V.

Following the final irradiation, the samples were heated to room temperature before a temperature dependent Hall effect measurement was performed using the same parameters as described above.

To evaluate the electrical behaviour of native defects in ZnO, defect calculations were performed using the Heyd–Scuseria–Ernzerhof (HSE) [23] screened hybrid functional and the projector augmented wave method [24], as implemented in the VASP code [25]. The fraction of screened Hartree–Fock exchange, α, was set to 37.5%, which results in an accurate description of the experimental band gap and lattice parameters of ZnO [26]. Thermodynamic charge-state transition levels of defects were calculated by following the standard formalism described in [27].

For charged defects we applied the anisotropic [28] Freysoldt-Neugebauer-Van de Walle correction [27]. Defect calculations were performed using a 96-atom supercell, a plane-wave basis set with an energy cutoff of 500 eV, and a special k-point at $\left(\frac{1}{4}, \frac{1}{4}, \frac{1}{4}\right)$. For defects involving V_O, however, a larger 192-atom supercell was required to ensure converged energy levels, as discussed in more detail elsewhere [29, 30]. Ionic relaxations were performed until the forces were reduced to less than 20 meV Å^{-1}, and spin-polarization was included.

3. Results and discussion

The results from the temperature dependent Hall effect measurements conducted before and after irradiation are presented in figure 2. Before irradiation all the studied samples have carrier concentrations (n) varying only very weakly with temperature with no sign of carrier freeze out. The strong positive temperature (T) dependence of the mobilities (μ) of SnO_2 and in particular ZnO indicate that these films are non-degenerate and that their carrier transport is limited by ionized impurity scattering [31]. The mobility of the In_2O_3 sample is seen to follow $\mu(T) \propto T$, indicating that the sample is degenerate with transport limited by grain boundary scattering [32]. For the lowest temperatures, the carrier concentration of both SnO_2 and ZnO seems to increase slightly. This is attributed to some form of parallel conduction either at the surface, or at the TCO/substrate interface [33, 34]. For CdO the negative temperature dependence of the mobility indicates that phonons are the dominant scattering mechanism, but also here a parallel conduction pathway could be present [35]. For Ga_2O_3 the mobility is seen to increase slowly with temperature, but at a lower rate than the $\mu \propto T^{3/2}$, which is expected for purely ionized impurity scattering in a non-degenerate material. A possible explanation for this temperature dependence could be that both ionized impurities and phonons together limit the carrier transport, possibly also aided by grain boundary scattering.

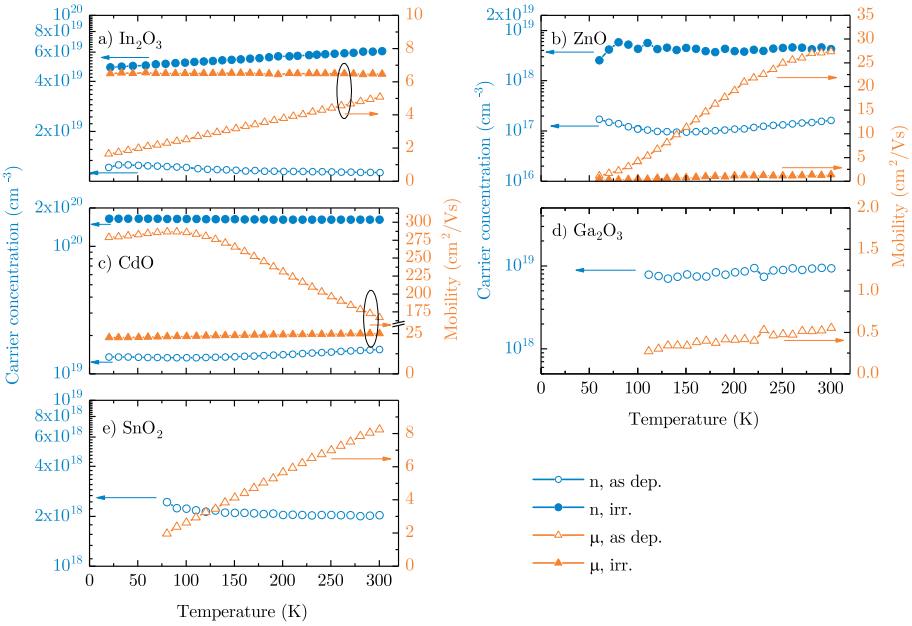

Figure 2. Temperature dependent Hall effect measurements before (open symbols) and after (filled symbols) irradiation of CdO, In_2O_3 and ZnO, as well as before irradiation of Ga_2O_3 and SnO_2. The carrier concentrations (n, blue) and mobilities (μ, orange) are plotted against the left and right vertical axis, respectively, and the legend applies to all the panels.

After irradiation to the maximum dose available in our setup, the carrier concentrations of CdO, In_2O_3 and ZnO have all increased compared to their as-deposited values. The strongest relative change is found in ZnO which increases from $n = 1.6 \times 10^{17}$ cm^{-3} to 4.3×10^{18} cm^{-3} at room temperature, while the carrier concentrations of CdO and In_2O_3 increase from 1.6×10^{19} and 1.1×10^{19} cm^{-3} to 1.6×10^{20} and 6×10^{19} cm^{-3}, respectively. Due to their high resistivities, Hall effect measurements on the Ga_2O_3 and SnO_2 samples were, unfortunately, not possible after irradiation.

For CdO and ZnO, the irradiation causes a considerably reduced mobility with a weak positive temperature dependence, suggesting that grain boundary scattering and/or other structural defects are the dominant scattering mechanisms. This is consistent with earlier work on the mobility of CdO [36]. The mobility of In_2O_3 on the other hand is, interestingly, found to increase after the irradiation. The increased carrier concentration and a temperature independent mobility, maintaining a value of 6.5 cm^2 (V s)$^{-1}$ throughout the measured temperature range, indicates that the irradiation has rendered the material degenerate. Furthermore, the increase in mobility could imply a decreased concentration of compensating defects.

To relate the carrier concentrations found from the Hall effect measurements to the defect charge state transition levels and predicted CNLs we calculate the Fermi level of each material in its as-deposited state by iteratively solving the Fermi–Dirac integral numerically [37]. The effective masses used in the calculations along with the band gaps of the materials and their calculated Fermi levels are presented in table 2. This shows that the CdO, Ga_2O_3 and In_2O_3 samples are degenerate, while the SnO_2 and ZnO are not. Due to the relatively low carrier concentrations in the as deposited samples, the conduction bands of the samples are assumed parabolic [42].

Table 2. Band gaps (E_g), effective masses (m^*), and Fermi levels (E_F) relative to the VBM. The Fermi levels were calculated from the room temperature Hall effect carrier concentrations by iterative numerical integrations of the Fermi–Dirac integral [37]. The band gaps are taken from [1, 5, 32, 38, 39] and the effective masses from [1, 32, 39–41].

	CdO	Ga_2O_3	In_2O_3	SnO_2	ZnO
E_g (eV)	2.31	4.80	2.79	3.35	3.37
m^* (m_e)	0.26	0.28	0.18	0.30	0.30
E_F (eV)	2.39	4.85	2.88	3.34	3.29

Figure 3 shows the resistances calculated from the *IV*-measurements as functions of displacement damage dose (D_d) for all the investigated samples. The top horizontal axis shows an approximate vacancy concentration for ZnO. This was calculated from the accumulated ion dose and vacancy profiles simulated using SRIM [22], where the displacement energies of zinc and oxygen were set to 34 and 44 eV, respectively [43]. The strong dynamic annealing of ZnO [21] was accounted for by assuming that only 1% of the generated vacancies survived immediate recombination [44]. The displacement damage dose shown on the bottom x-axis is the product of the

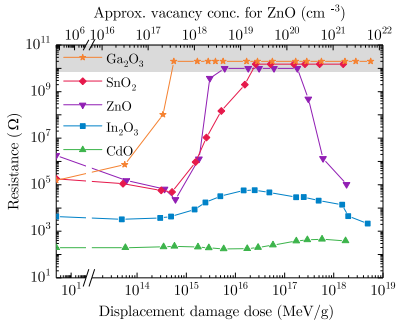

Figure 3. Resistance as function of accumulated displacement damage dose (D_d) measured at low temperature *in situ* between each irradiation step with the ion beam blanked. The datapoints plotted in the grey shaded region are outside the measurement range of our instrument.

ion dose and the non-ionizing energy loss (NIEL), which was calculated from SRIM simulations according to the procedure described in [45]. For these calculations, the displacement energies of zinc and oxygen in ZnO were set to 34 and 44 eV, as before. As reliable values are not readily available for all the studied materials, the displacement energies for both cations and oxygen in all the other samples were set to 15 eV, a common value for semiconductors [19, 46, 47]. The SRIM simulations were run for 20 000 primary ions and to avoid surface effects the 10 data points closest to the surface were discarded. The resulting NIEL values were 57.2, 56.2, 49.1, 51.7 and 60.6 MeV cm^2 g^{-1} for CdO, Ga_2O_3, In_2O_3, SnO_2 and ZnO, respectively. Recalculating the NIEL for ZnO with 15 eV displacement energies for both Zn and O gives a value of 65.6 MeV cm^2 g^{-1}.

As the dimensions of the samples do not change between measurements, and assuming that the resistance of the contacts remains constant, any observed change in resistance is necessarily caused by a change in resistivity, i.e. a change in carrier concentration and/or mobility of the samples. The resistivity of In_2O_3 follows the same trend as observed in a recent paper by Vines *et al* [19]. At displacement damage doses below $\sim 5 \times 10^{13}$ MeV g^{-1}, the resistivity shows a minor decrease, followed by a stronger increase between $\sim 5 \times 10^{13}$ and 2.5×10^{16} MeV g^{-1}. At even higher displacement damage doses the resistivity again starts to decrease, and does not seem to stabilize at any ultimate value within the studied dose range. At the last datapoint, corresponding to a displacement damage dose of 4.9×10^{18} MeV g^{-1}, the sample has a lower resistivity than in its as-deposited state.

For Ga_2O_3 the resistivity increases monotonically, and for displacement damage doses greater than 3.4×10^{14} MeV g^{-1} the resistance is beyond the measurement range of our setup, indicated by the shaded region along the top of figure 3. The immeasurably high resistance is retained until at least a displacement damage dose of 5.6×10^{18} MeV g^{-1}, confirming and extending the findings in [19], where the same behaviour was observed but the irradiation was aborted after an ion dose of 10^{14} cm^{-2}, corresponding to $D_d \sim 5.6 \times 10^{15}$ MeV g^{-1}. In a recent report, proton irradiation of Ga_2O_3 to doses $\geqslant 2 \times 10^{13}$ cm^{-2} has also been shown to decrease the carrier concentration dramatically, to the point that no response is obtained in capacitance-voltage measurements [48]. Subsequent heat treatment at temperatures of ∼180–380 °C were found to greatly recover the carrier concentration, and the required temperature for recovery correlated positively with the irradiation dose. For our Ga_2O_3 sample irradiated to a displacement damage dose of 5.6×10^{18} MeV g^{-1}, no sign of electrical recovery was observed after annealing at temperatures up to 900 °C in air. We attribute this to the higher defect concentration introduced in our experiment.

The SnO_2 and ZnO samples qualitatively exhibit an intermediate behaviour compared to Ga_2O_3 and In_2O_3. Both display an initial, slow decrease in resistivity for displacement damage doses below 5×10^{14} MeV g^{-1}, followed by a rapid increase for doses up to at least 1.8×10^{16} MeV g^{-1} (ZnO) or 2.6×10^{16} MeV g^{-1} (SnO_2). Like Ga_2O_3, the SnO_2 sample remains highly resistive throughout the remainder of the dose range, whereas the ZnO sample behaves more like In_2O_3, showing a monotonically decreasing resistivity after a displacement damage dose of 1.8×10^{17} MeV g^{-1}. Kucheyev *et al* have previously observed a similar behavior for ZnO [20, 49]. They attributed the decreasing resistivity at high doses to the onset of hopping conduction [50], but this was not discussed in further detail in their work. Using Arrhenius plots of the measured resistivities before and after irradiation (not shown) we examined whether conduction by pure- or phonon-assisted hopping is likely to take place in our samples. No evidence of such conduction mechanisms was found for any sample, however the temperature dependences of the resistivities were too weak for the analysis to be conclusive.

The CdO sample exhibits a remarkably dose independent resistivity throughout the range. A minor drop in resistivity can be observed after a displacement damage dose of about 5.8×10^{15} MeV g^{-1} followed by a slight increase to a peak at 5.8×10^{17} MeV g^{-1} and at the last data point the resistivity again seems to decrease. Room temperature ion irradiation experiments on CdO have previously shown monotonic increases in the carrier concentration with increasing dose until saturating at 2.2×10^{20} cm^{-3} or 5×10^{20} cm^{-3} [9, 18]. This was interpreted as a consequence of the charge neutrality level being located above the conduction band minimum in CdO, and that the irradiation induced defects pushes the Fermi level towards the CNL. For CdO specifically, such an explanation could well fit our results presented in figures 2 and 3. The results for In_2O_3, SnO_2, and ZnO on the other hand, do not seem to fit the model. In particular, the facts that the resistivities neither change monotonically, nor stabilize at any ultimate value does not seem to fit with the idea of the CNL position being a reliable predictor of the outcome of a low temperature ion irradiation experiment in general. An underlying assumption of the charge neutrality model is that the stability and probability of formation of a given defect species is determined by its formation energy. Although the introduction of a specific species is easily accommodated in theoretical computations, and despite its appealing simplicity, we

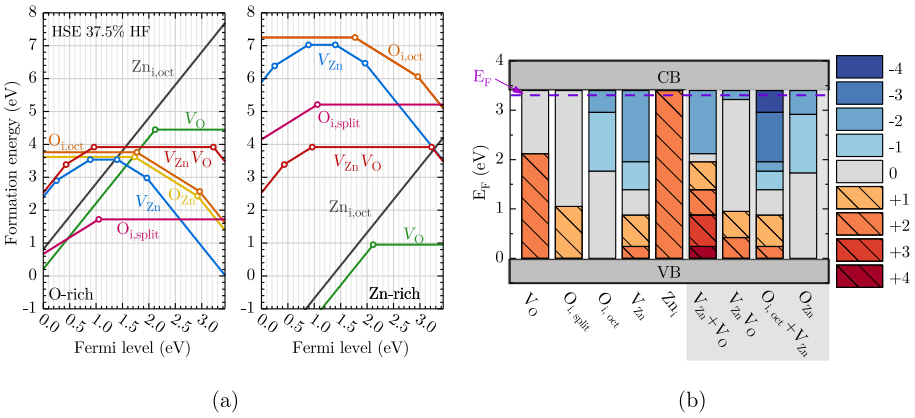

(a) (b)

Figure 4. Thermodynamic defect charge state transition levels in ZnO. In (a) plotted in the conventional fashion as function of formation energy. The calculations for the zinc and oxygen vacancies were first published in [52], while the data for the $V_{Zn}V_O$ divacancy are published in [30]. Panel (b) shows the same dataset, but plotted in a more suitable way for the following discussion. Here, VB and CB refers to the valence- and conduction band minima, respectively, and the purple dashed line below the CB represents the calculated Fermi level of the as-deposited sample, as given in table 2. The columns labelled $V_{Zn}+V_O$ and $O_{i,oct}+V_{Zn}$ show the sum of the charge states of the individual point defects, while the columns $V_{Zn}V_O$ and O_{Zn} show the states for the complexes as calculated by DFT. The data for V_{Zn} and V_O, and $V_{Zn}V_O$ are reused from [30, 52], respectively, with permission.

question whether such a model is generally capable of describing the outcome of an ion irradiation experiment.

In order to understand the detailed process of defect introduction, a short review of the ion irradiation process is relevant. When a primary ion hits an atom in the sample, the atom may be ejected from its lattice site into an interstitial position, thus creating a Frenkel pair. During irradiation, this Frenkel pair generation takes place on each of the sublattices of the sample in a random process [51]. The defect generation mainly depends on the energy of the ion beam, mass of the ion species and the displacement energies of the different sublattices of the sample. Due to the high energy of the incident ion, the formation energies of the individual defects are expected to play only a negligible role in their formation probability, but may still be relevant for their thermal stability. Although they may, in principle, be formed in any allowed charge state, each defect will quickly accept or donate electrons until it is in the most favourable charge state, as governed by the Fermi level.

To explain the observed dose dependence of the resistivity shown in figure 3, we assume that the primary 3 MeV Si^{2+} ions are sufficiently energetic to produce Frenkel pairs at both the cation and anion sublattices. As our experiments are performed at low temperatures, clustering of the primary defects due to diffusion and defect reactions are expected to be suppressed for low irradiation doses. In the following the details of the defect generation will be discussed for each material separately, starting with ZnO.

3.1. ZnO

Thermodynamic charge states and transition levels for the intrinsic point defects in ZnO, as calculated by hybrid functional DFT, are illustrated in figure 4. Panel (a) is a conventional formation energy diagram showing the favoured charge state and formation energy of the defects. In panel (b) the formation energy is discarded to highlight the information needed for the following discussion, namely the charge states as functions of Fermi level position. In addition to the point defects, two small complexes, the divacancy ($V_{Zn}V_O$) [30] and the oxygen antisite (O_{Zn}), are shown. The shaded regions represent the valence- (VB) and conduction bands (CB), and the estimated Fermi level before irradiation is indicated by the dashed line. Based on these predictions, introducing a Frenkel pair on the zinc sublattice in *n*-type ZnO will not yield any net change in the carrier concentration as the zinc vacancy is doubly negative for Fermi level positions >2 eV above the valence band, while the interstitial is doubly positive throughout the bandgap. It should be noted that the interstitial is known to be mobile at temperatures above 65 K. On the oxygen sublattice on the other hand, the vacancy is a deep double donor and thus in its neutral charge state in *n*-type material (above 2.1 eV) while the interstitial can be either neutral ($O_{i,\,split}$) or doubly negative ($O_{i,\,oct}$). When treating defect generation as a ballistic process and neglecting transitions between the two, the formation of $O_{i,\,oct}$ and $O_{i,\,split}$ will be random and thus the concentration of the two configurations will be equal. Hence, for the indicated E_F the average net effect of a Frenkel pair on the oxygen sublattice is to trap one electron.

Randomly generating Frenkel pairs on both sublattices will thus compensate *n*-type material until the Fermi level crosses the (+2/0) transition of the oxygen vacancy (2.1 eV above the valence band maximum) at which point no further change in the carrier concentration will take place. This is qualitatively consistent with the observed increase in resistivity seen for ZnO in figure 3 for displacement damage doses between 6×10^{14} MeV g^{-1} and $\sim 6 \times 10^{16}$ MeV g^{-1}.

As the dose is increased above 1.8×10^{17} MeV g^{-1}, figure 3 shows that the resistivity of ZnO starts decreasing. Employing

only the isolated intrinsic defects, as discussed above, there should be no driving force towards a lower resistivity as the Fermi level will be pinned at the deep transition level of the oxygen vacancy. However, as the dose is increased the distance between individual defects is reduced, and even though diffusion is suppressed at low temperature, the initial assumption of not forming defect complexes does no longer apply. As an example, assuming uniformly distributed point defects at a concentration of 10^{19} cm^{-3}, the average distance between each defect is on the order of 5 nm. Hence, if such concentrations of Frenkel pairs are introduced, the probability of one defect being generated in the immediate vicinity of another is high, and thus complexes can form virtually without the need for diffusion. The process behind the decreasing resistance at displacement damage doses greater than 3×10^{17} MeV g^{-1} for ZnO is thus believed to be the same as that responsible for the increasing resistance at lower doses, generation of Frenkel pairs. The only difference being the concentration of defects already present in the sample when a new Frenkel pair is formed. Threshold values for when the isolated point defects and complexes start to dominate the electrical characteristics of the ZnO sample are roughly 5×10^{14} and 10^{16}–10^{17} MeV g^{-1}, respectively, as seen in figure 3.

In principle, the following complexes between intrinsic point defects could be considered: $V_{Zn}V_O$, O_{Zn}, Zn_O and Zn_iO_i, in addition to larger clusters. Zn_iO_i would be a ZnO positioned interstitially which, although observed in pelletized ZnO powders [53], is not expected to be stable in thin films and is disregarded. To the best of our knowledge, no hybrid DFT data exists for the Zn antisite, Zn_O, hence this complex is also disregarded in the following. Furthermore, complexes involving one or more impurity atoms are also possible.

The $V_{Zn}V_O$ divacancy has been both theoretically and experimentally found to be stable, at least at temperatures below 200 °C [30, 54]. This divacancy was found to be electrically neutral in a neutron irradiated ZnO crystal, but could be excited to the +1 charge state by laser illumination at low temperatures [54]. From hybrid DFT calculations it is suggested that both the −2 and +2 states can also be stabilized [30]. By correlating positron annihilation spectroscopy (PAS) and *IV* measurements on oxygen irradiated ZnO thin films, Zubiaga *et al* have shown that the introduction of zinc vacancies increases the resistivity of the film [55]. They also found that, under their irradiation conditions using O-ions with an energy of 2 MeV, a maximum V_{Zn} concentration of about 2–5×10^{18} cm^{-3} could be obtained before the formation of vacancy complexes started. Increasing the dose further did not significantly change the resistivity, from which it was tentatively concluded that the vacancy complexes were electrically inactive. The details of the complexes were not discussed, but results from electron irradiation experiments of ZnO indicate that the V_{Zn} takes part in more than one type of complex [56, 57]. The onset of cluster formation as a function of dose, depends on the energy and mass of the irradiated ion, and although the exact position of the resistance peak as function of irradiation dose cannot be directly observed (due to the high resistance in the range 6×10^{15}–1.8×10^{17} MeV g^{-1}), our results qualitatively agree with those of Zubiaga *et al* [55]. In the grey shaded region towards the right of figure 4 we show the effect of two complexes involving V_{Zn} on the net charge state of the material. The column labelled $V_{Zn} + V_O$ shows the sum of the charge states of the two defects, while the column $V_{Zn}V_O$ shows the charge states of the divacancy complex as computed by DFT in [30]. It is found that for Fermi levels between 2.09 and 3.2 eV above the VBM the divacancy has a higher charge state than the sum of the constituents. Hence, forming the complex can increase the carrier concentration and pull E_F up to VBM + 3.2 eV, thus explaining the decreasing resistivity at higher doses. This complex alone will, however, not increase the carrier concentration beyond that of the as-deposited material, and other complexes are needed. The oxygen antisite O_{Zn} shown to the far right of figure 4 will not contribute since, even though it has a higher charge state than the constituent point defects throughout the band gap, it is still an acceptor, hence some other, unknown, complex must come into play.

The remaining, unexplained, feature of the ZnO curve of figure 3 is the initial decrease in resistivity at low doses. Although several studies of the dose dependent resistivity of ZnO have been made in the past [20, 49, 53, 55] this has, to the best of our knowledge, not previously been observed in this material. A possible reason is that our irradiation and *IV* measurements are performed at low temperature, while the cited works have all been performed at room temperature or above. The detailed mechanism behind this resistance drop, observed also for In_2O_3 and SnO_2, is not clear and warrants further, dedicated, studies.

3.2. In_2O_3

The atomic structure of In_2O_3 consists of two inequivalent In sites and two different interstitial positions, thus this consequently increases the complexity of the defect structure. As a result, computing defect charge state transition levels have proven challenging and the results are heavily dependent on the details of the computation. Even qualitatively determining whether the oxygen vacancy is a deep or shallow donor is not straightforward [58], but several recent hybrid functional DFT computations have agreed that it is in fact shallow [38, 59, 60]. Due to the excellent agreement between the computed value and the experimental band gap, we will in the following refer to the defect levels found in [38], illustrated in figure 5, as the basis for discussing the In_2O_3 curve of figure 3.

For the Fermi level indicated in figure 5, a Frenkel pair on the oxygen sublattice can have a net charge state of -1, 0 or +1 depending on the position of the oxygen interstitial. Assuming that the positions have equal probabilities of occupation, the averaged charge of the oxygen Frenkel pairs is thus zero. For a Frenkel pair on the indium sublattice the net charge state is negative as long as the Fermi level is higher than 0.21 eV below the CBM. Random introduction of Frenkel pairs can thus qualitatively explain the increase in resistance seen at displacement damage doses in the range 4.9×10^{14}–2.5×10^{16} MeV g^{-1}. As for ZnO, we argue that the decreasing resistivity at higher doses is caused by formation of defect complexes. For instance figure 5 shows that, for Fermi levels in the vicinity of the CBM, the defect reaction $V_{In}^{b} + O_i^{c} \rightarrow O_{In}^{b}$ will transform

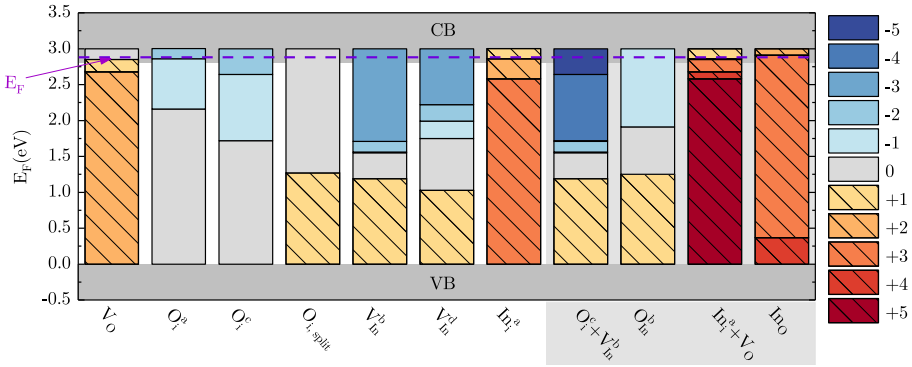

Figure 5. Thermodynamic charge states and transition levels for intrinsic defects in In_2O_3. The estimated Fermi level before irradiation is represented by the dashed purple line 2.88 eV above the VBM. For the antisites towards the right of the figure, we show also the arithmetic sums of the charges of the constituent point defects to highlight the effect of complex formation. All the transition levels were extracted from [38] with permission.

two defects with a total charge of −3, −4 or −5 to a complex of charge −1, thus releasing 2, 3 or 4 electrons to the conduction band. This complex is still an acceptor, however, and does not explain why the carrier concentration after the final irradiation dose is higher than in the as-deposited sample. The indium antisite (In_O) formed by combining one In_i^a and one oxygen vacancy, on the other hand, is a donor which, for Fermi levels within the conduction band, has a higher charge state than the constituents. This intrinsic complex could thus contribute to pushing the Fermi level deeper into the conduction band.

3.3. Ga_2O_3 *and* SnO_2

As seen in figure 3, the dose dependence of the resistances of Ga_2O_3 and SnO_2 behaves qualitatively different from those of In_2O_3 and ZnO. Nevertheless, if we postulate that the complexes forming at higher doses do not release the electrons trapped by the constituent point defects but rather retain their acceptor character throughout the dose range, the same general model as used above can be applied to these materials as well.

In [48], a thorough search for defects responsible for the irradiation induced resistivity in Ga_2O_3 was undertaken by deep level transient- and optical spectroscopy and DFT calculations. Their results suggest that a combination of V_{Ga}, Ga_i and Ga_O pins the Fermi level at least 0.5 eV below the CBM, thus causing its high resistivity. Positron annihilation spectroscopy has shown that isolated gallium vacancies can be formed in concentrations greater than 5×10^{18} cm^{-3} during film growth [61], and V_{Ga} generated from ion irradiation has also been evidenced [62]. In the latter reference it is found, however, that the V_{Ga} concentration alone is too low to account for the observed charge carrier removal rate, and it is argued that the main cause of increased resistivity is that the irradiation induced defects form neutral complexes with shallow donors. The details of these complexes are still unknown, but neutron irradiation experiments followed by deep level spectroscopy shows both a considerably increased concentration of a defect level situated 2.00 eV below the conduction band minimum, and the introduction of a new state at 1.29 eV below the CBM [63]. These defects are correlated with a reduction in the electron concentration from $\sim 1.2 \times 10^{17}$ cm^{-3} to $\sim 4.0 \times 10^{16}$ cm^{-3} after irradiation to an 1 MeV equivalent dose of 1.7×10^{15} cm^{-2}.

Figure 6 shows the defect levels calculated in [48], with the Fermi level of the as-deposited sample superimposed. If a Frenkel pair is generated on the Ga sublattice for the given Fermi level, the net charge state will be −1, while for the oxygen sublattice it will be either 0 or −2 depending on the details of the oxygen interstitial. Assuming again equal probability of the interstitial sites, the average charge state will be −1 and thus random generation of Frenkel pairs on both sublattices is expected to reduce the carrier concentration and increase the resistivity of the sample. Comparing the charge states of individual gallium interstitials, oxygen vacancies and gallium antisites, it is found that the formation of a gallium antisite from its constituent point defects decreases its charge state for all the oxygen sites. Hence, this particular complex will not reduce the resistance if formed at high doses, and unless other, donor like, complexes form the carrier concentration will remain low and the resistivity high as observed in figure 3.

For SnO_2 it has been suggested that removal of substitutional hydrogen as well as introduction of intrinsic acceptors, e.g. V_{Sn}, O_i or O_{Sn}, is responsible for the dose dependent increase in resistivity [64]. Like for ZnO, DFT calculations predict a deep (+2/0) transition level for V_O, while tin interstitials and antisites are expected to be positively ionized throughout the band gap [65]. Based on this, Frenkel pairs on the tin sublattice are expected to give zero net contribution to the carrier concentration. On the oxygen sublattice, the deep V_O means that Fermi levels close to the CBM will cause a surplus of electrically active acceptors to form, hence explaining the increasing resistivity at doses greater than 1.5×10^{15} MeV g^{-1}. In addition, the dual valency of Sn can possibly also play a role. If the irradiation somehow induces a reduction of Sn^{4+} to Sn^{2+} this will trap two electrons and contribute to the observed increase in resistivity.

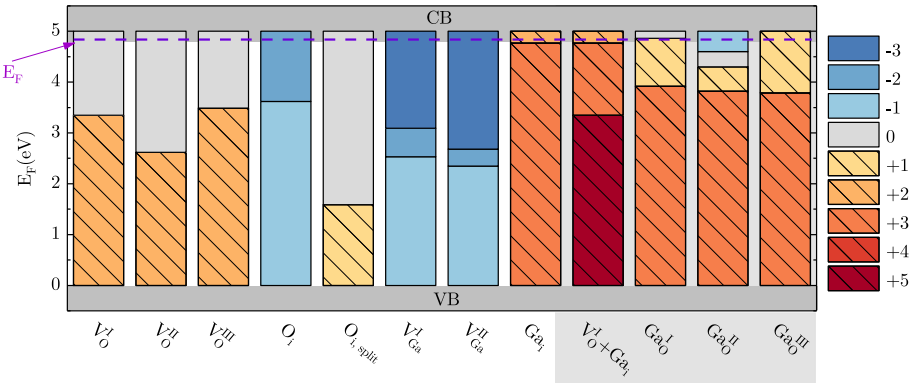

Figure 6. Thermodynamic charge states and their transition levels for intrinsic defects in Ga_2O_3. The estimated Fermi level before irradiation is represented by the dashed purple line 4.85 eV above the VBM. For the Ga_O^I antisite towards the right of the figure, we show also the arithmetic sum of the constituent V_O^I and Ga_i point defects. All the transition levels were sourced from [48] (licensed under a Creative Commons Attribution (CC BY) license).

As Ga_2O_3 and SnO_2 have a markedly different dose dependent resistance behaviour from the other three materials studied in this paper it is interesting to note another feature where they are different. Unlike most other metal oxides, Ga_2O_3 and SnO_2 have two possible positions for the hydrogen interstitial. One position disrupts the anion-cation bonds of the host material, and gives the H(+/−) level associated with the CNL, as found in other materials as well [13]. The other configuration places the hydrogen on an oxygen lone-pair and may give an energetically favourable donor state well within the conduction band [66]. As discussed in [64] it is possible that removal of such pre-existing hydrogen donors contribute to the increasing resistance with irradiation.

3.4. CdO

For CdO only a minor change in the resistivity is observed across the dose range. This can possibly be explained by hybrid-DFT calculations, which indicate that all the intrinsic defects, as well as interstitial and substitutional hydrogen, will be either neutral or in a positive charge state until the Fermi level is about 0.6 eV above the CBM [67]. A likely reason why the introduction of such positively charged defects does not considerably decrease the resistivity could be a simultaneous, comparable decrease in mobility. The Hall effect results indeed show that irradiation to a displacement damage dose of 1.7×10^{18} MeV g^{-1} yields an increase in electron concentration from 1.34×10^{19} to 1.65×10^{20} cm^{-3} and a decrease in mobility from 285 to 22.9 cm^2 (V s)$^{-1}$ at a temperature of 70 K, as illustrated in figure 2. It should be noted that the sample was stored at room temperature for approximately two weeks between the *IV*- and Hall effect measurements. Diffusion and/or defect reactions may in principle have taken place during this time, hence the carrier concentration and mobility measured by the Hall effect may differ somewhat from their values during the *IV* measurements. Nevertheless, these values seem to explain the observation that the resistance is close to constant as a function of irradiation dose for CdO in figure 3.

To summarize, for displacement damage doses greater than approximately 5×10^{14} MeV g^{-1} three types of behaviour are possible. (i) If the net charge state of the point defects and their complexes is positive the carrier concentration will increase. This tends to reduce the resistivity, with a magnitude dependent on the evolution of the mobility. If the mobility decreases comparably to the increase in carrier concentration, the resistivity will remain constant, as seen for CdO. (ii) If the net charge state of the point defects is negative, while that of their complexes is positive, the resistivity will initially increase followed by a decrease as the dose is increased further, resulting in a peak behaviour. This is seen for In_2O_3 and ZnO. (iii) If the net charge state of the point defects and their complexes is negative, the resistivity will increase and remain high for arbitrarily high doses, as observed for Ga_2O_3 and SnO_2.

This model assumes that the irradiation forms Frenkel pairs on all sublattices of the sample and that, at low doses, the point defects do not agglomerate into complexes. Further, we assume that complexes are able to form as the dose, and consequently the point defect concentration, increases above a threshold value. Depending on the charge states of the defects and their complexes, this can result in a 2-stage behaviour of the defect concentration dependent Fermi level. In cases (i) and (iii) above, the Fermi level will change monotonically with defect concentration towards the CNL, and in these cases our model is identical to the ADM. In case (ii), as we observe for materials ZnO, In_2O_3 and CdO, a more involved defect/complex balance is observed. This behavior is found when the overall charge balance is changed when going from isolated defects towards the formation of defect complexes. We believe the model to be general and applicable to any semiconducting material. At present it cannot explain the decreasing resistivity seen for In_2O_3, SnO_2 and ZnO at the lowest doses, and investigating this requires further studies outside the scope of this work.

4. Conclusions

In conclusion, it has been found that some materials can be made heavily *n*-type by introducing intrinsic defects, whereas others become highly resistive. The evolution of sample resistance with dose has been found to proceed along one of three possible routes. Ga_2O_3 and SnO_2 irradiated to displacement damage doses of 5.6×10^{18} or 1.6×10^{18} MeV g^{-1}, respectively, were found to be highly resistive. For In_2O_3 and ZnO the irradiation ultimately turned the samples less resistive than in their respective as-deposited states, but a more resistive state is observed at intermediate doses. The resistance of CdO changes only weakly with irradiation, probably caused by complementary changes in carrier concentration and mobility. For CdO, In_2O_3 and ZnO, the irradiation was found to increase the carrier concentration, and for In_2O_3 the mobility was increased as well. This work shows that the combined charge state of randomly introduced Frenkel pairs can explain the evolution of the charge carrier concentration as function of ion irradiation dose. For all the samples except SnO_2 the change in carrier concentration after irradiation is qualitatively in accordance with the respective charge neutrality levels [66].

Furthermore, the formation of defect complexes is found to be important in order to understand the behaviour at displacement damage doses exceeding about 10^{16} MeV g^{-1}, even in low temperature experiments due to the high density of generated defects. Thus, this work contributes as a further development of the amphoteric defect model for defect evolution in irradiated samples. Finally, it should be noted that the differing behaviour between the various materials is expected to be caused by differences in their thermodynamic defect charge state transitions. In particular, the position of the oxygen vacancy relative to the divacancy or other small complexes is believed to play a major role, thus showing both the importance of defect complexes in general and also the potential for using hybrid DFT calculations to explain the defect evolution in a range of wide band-gap oxides.

Acknowledgments

The authors acknowledge Holger Hochmuth of the University of Leipzig for growing the Ga_2O_3 and In_2O_3 films, Rodrigo Martinez Gazoni and Roger J Reeves of the University of Canterbury for the growth of the SnO_2 films, and Viktor Bobal of the University of Oslo for operating the ion implanter. The Research Council of Norway is acknowledged for the support to the Norwegian Micro- and Nano-Fabrication Facility, NorFab, project number 245963, and the FOXHOUND project. The Norwegian Nano Network and UiO:Energy are gratefully acknowledged for travel and conference support.

ORCID iDs

J Borgersen https://orcid.org/0000-0002-4350-2233
L Vines https://orcid.org/0000-0001-5759-7192
Y K Frodason https://orcid.org/0000-0001-9151-2084
A Kuznetsov https://orcid.org/0000-0003-1822-9850
H von Wenckstern https://orcid.org/0000-0002-3936-275X
M Grundmann https://orcid.org/0000-0001-7554-182X
M Allen https://orcid.org/0000-0001-8786-6429
J Zúñiga-Pérez https://orcid.org/0000-0002-7154-641X
K M Johansen https://orcid.org/0000-0002-6268-1740

References

[1] Özgür Ü, Alivov Y I, Liu C, Teke A, Reshchikov M A, Doğan S, Avrutin V, Cho S-J and Morkoç H 2005 A comprehensive review of ZnO materials and devices *J. Appl. Phys.* **98** 041301
[2] Bierwagen O 2015 Indium oxide–a transparent, wide-band gap semiconductor for (opto)electronic applications *Semicond. Sci. Technol.* **30** 024001
[3] Chandiramouli R and Jeyaprakash B G 2013 Review of CdO thin films *Solid State Sci.* **16** 102–10
[4] Das S and Jayaraman V 2014 SnO_2: a comprehensive review on structures and gas sensors *Prog. Mater. Sci.* **66** 112–255
[5] von Wenckstern H 2017 Group-III sesquioxides: growth, physical properties and devices *Adv. Electron. Mater.* **3** 1600350
[6] Alkauskas A, McCluskey M D and Van de Walle C G 2016 Tutorial: defects in semiconductors—Combining experiment and theory *J. Appl. Phys.* **119** 181101
[7] Walukiewicz W 1988 Fermi level dependent native defect formation: consequences for metal–semiconductor and semiconductor–semiconductor interfaces *J. Vac. Sci. Technol. B: Microelectron. Process. Phenom.* **6** 1257–62
[8] Walukiewicz W 1987 Mechanism of Schottky barrier formation: the role of amphoteric native defects *J. Vac. Sci. Technol. B: Microelectron. Process. Phenom.* **5** 1062–7
[9] King P D C, Veal T D, Jefferson P H, Zúñiga-Pérez J, Muñoz-Sanjosé V and McConville C F 2009 Unification of the electrical behavior of defects, impurities, and surface states in semiconductors: virtual gap states in CdO *Phys. Rev.* B **79** 035203
[10] King P D C, Veal T D, Payne D J, Bourlange A, Egdell R G and McConville C F 2008 Surface electron accumulation and the charge neutrality level in In_2O_3 *Phys. Rev. Lett.* **101** 116808
[11] Mönch W 1996 Empirical tight-binding calculation of the branch-point energy of the continuum of interface-induced gap states *J. Appl. Phys.* **80** 5076–82
[12] Schleife A, Fuchs F, Rödl C, Furthmüller J and Bechstedt F 2009 Branch-point energies and band discontinuities of III-nitrides and III-/II-oxides from quasiparticle band-structure calculations *Appl. Phys. Lett.* **94** 012104
[13] Van de Walle C G and Neugebauer J 2003 Universal alignment of hydrogen levels in semiconductors, insulators and solutions *Nature* **423** 626–8
[14] Tersoff J 1984 Theory of semiconductor heterojunctions: the role of quantum dipoles *Phys. Rev.* B **30** 4874–7
[15] Brudnyi V N, Grinyaev S N and Kolin N G 2003 Electronic properties of irradiated semiconductors. a model of the Fermi level pinning *Semiconductors* **37** 537–45
[16] Falabretti B and Robertson J 2007 Electronic structures and doping of SnO_2, $CuAlO_2$, and $CuInO_2$ *J. Appl. Phys.* **102** 123703
[17] Amini M N, Saniz R, Lamoen D and Partoens B 2011 Hydrogen impurities and native defects in CdO *J. Appl. Phys.* **110** 063521
[18] Speaks D T, Mayer M A, Yu K M, Mao S S, Haller E E and Walukiewicz W 2010 Fermi level stabilization energy in cadmium oxide *J. Appl. Phys.* **107** 113706
[19] Vines L, Bhoodoo C, von Wenckstern H and Grundmann M 2018 Electrical conductivity of In_2O_3 and Ga_2O_3 after low temperature ion irradiation; implications for instrinsic defect

formation and charge neutrality level *J. Phys.: Condens. Matter.* **30** 025502
[20] Kucheyev S O, Deenapanray P N K, Jagadish C, Williams J S, Yano M, Koike K, Sasa S, Inoue M and Ogata K-i 2002 Electrical isolation of ZnO by ion bombardment *Appl. Phys. Lett.* **81** 3350–2
[21] Kucheyev S O, Williams J S, Jagadish C, Zou J, Evans C, Nelson A J and Hamza A V 2003 Ion-beam-produced structural defects in ZnO *Phys. Rev.* B **67** 094115
[22] Ziegler J F, Biersack J P and Littmark U 1985 *The Stopping and Range of Ions in Solids* (New York: Pergamon)
[23] Krukau A V, Vydrov O A, Izmaylov A F and Scuseria G E 2006 Influence of the exchange screening parameter on the performance of screened hybrid functionals *J. Chem. Phys.* **125** 224106
[24] Blöchl P E 1994 Projector augmented-wave method *Phys. Rev.* B **50** 17953–79
[25] Kresse G and Furthmüller J 1996 Efficient iterative schemes for *ab initio* total-energy calculations using a plane-wave basis set *Phys. Rev.* B **54** 11169–86
[26] Oba F, Togo A, Tanaka I, Paier J and Kresse G 2008 Defect energetics in ZnO: a hybrid Hartree–Fock density functional study *Phys. Rev.* B **77** 245202
[27] Freysoldt C, Grabowski B, Hickel T, Neugebauer J, Kresse G, Janotti A and Van de Walle C G 2014 First-principles calculations for point defects in solids *Rev. Mod. Phys.* **86** 253–305
[28] Kumagai Y and Oba F 2014 Electrostatics-based finite-size corrections for first-principles point defect calculations *Phys. Rev.* B **89** 195205
[29] Lyons J L, Varley J B, Steiauf D, Janotti A and Van de Walle C G 2017 First-principles characterization of native-defect-related optical transitions in ZnO *J. Appl. Phys.* **122** 035704
[30] Frodason Y K, Johansen K M, Alkauskas A and Vines L 2019 Negative-*u* and polaronic behavior of the Zn–O divacancy in ZnO *Phys. Rev.* B **99** 174106
[31] Look D C 1989 *Electrical Characterization of GaAs Materials and Devices* (New York: Wiley)
[32] Farahani S K V, Muñoz-Sanjosé V, Zúñiga-Pérez J, McConville C F and Veal T D 2013 Temperature dependence of the direct bandgap and transport properties of CdO *Appl. Phys. Lett.* **102** 022102
[33] Look D C, Mosbacker H L, Strzhemechny Y M and Brillson L J 2005 Effects of surface conduction on Hall-effect measurements in ZnO *Superlattices Microstruct.* **38** 406–12 E-MRS 2005 Symp. G: ZnO and Related Materials
[34] Roro K T, Kassier G H, Dangbegnon J K, Sivaraya S, Westraadt J E, Neethling J H, Leitch A W R and Botha J R 2008 Temperature-dependent Hall effect studies of ZnO thin films grown by metalorganic chemical vapour deposition *Semicond. Sci. Technol.* **23** 055021
[35] Karsthof R, von Wenckstern H, Zúñiga-Pérez J, Deparis C and Grundmann M 2020 Nickel oxide–based heterostructures with large band offsets *Phys. Status Solidi b* **257** 1900639
[36] Farahani S K V, Veal T D, King P D C, Zúñiga-Pérez J, Muñoz-Sanjosé V and McConville C F 2011 Electron mobility in CdO films *J. Appl. Phys.* **109** 073712
[37] Kim R, Wang X and Lundstrom M 2008 *Notes on Fermi-Dirac Integrals* (https://arxiv.org/ftp/arxiv/papers/0811/0811.0116.pdf)
[38] Chatratin I, Sabino F P, Reunchan P, Limpijumnong S, Varley J B, Van de Walle C G and Janotti A 2019 Role of point defects in the electrical and optical properties of In_2O_3 *Phys. Rev. Mater.* **3** 074604
[39] Farahani S K V, Veal T D, Mudd J J, Scanlon D O, Watson G W, Bierwagen O, White M E, Speck J S and McConville C F 2014 Valence-band density of states and surface electron accumulation in epitaxial SnO_2 films *Phys. Rev.* B **90** 155413
[40] Peelaers H and Van de Walle C G 2015 Brillouin zone and band structure of β-Ga_2O_3 *Phys. Status Solidi b* **252** 828–32
[41] Feneberg M, Nixdorf J, Lidig C, Goldhahn R, Galazka Z, Bierwagen O and Speck J S 2016 Many-electron effects on the dielectric function of cubic In_2O_3: effective electron mass, band nonparabolicity, band gap renormalization, and Burstein–Moss shift *Phys. Rev.* B **93** 045203
[42] Fuchs F and Bechstedt F 2008 Indium-oxide polymorphs from first principles: quasiparticle electronic states *Phys. Rev.* B **77** 155107
[43] Look D C, Farlow G C, Reunchan P, Limpijumnong S, Zhang S B and Nordlund K 2005 Evidence for native-defect donors in *n*-type ZnO *Phys. Rev. Lett.* **95** 225502
[44] Hupfer A, Bhoodoo C, Vines L and Svensson B G 2016 Formation and annihilation of E4 centers in ZnO: influence of hydrogen *J. Appl. Phys.* **119** 181506
[45] Messenger S R, Burke E A, Summers G P, Xapsos M A, Walters R J, Jackson E M and Weaver B D 1999 Nonionizing energy loss (NIEL) for heavy ions *IEEE Trans. Nucl. Sci.* **46** 1595–602
[46] Loferski J J and Rappaport P 1958 Radiation damage in Ge and Si detected by carrier lifetime changes: damage thresholds *Phys. Rev.* **111** 432–9
[47] Svensson B G, Jagadish C, Hallén A and Lalita J 1997 Generation of vacancy-type point defects in single collision cascades during swift-ion bombardment of silicon *Phys. Rev.* B **55** 10498–507
[48] Ingebrigtsen M E, Kuznetsov A Y, Svensson B G, Alfieri G, Mihaila A, Badstübner U, Perron A, Vines L and Varley J B 2019 Impact of proton irradiation on conductivity and deep level defects in β-Ga_2O_3 *APL Mater.* **7** 022510
[49] Kucheyev S O, Jagadish C, Williams J S, Deenapanray P N K, Yano M, Koike K, Sasa S, Inoue M and Ogata K-i 2003 Implant isolation of ZnO *J. Appl. Phys.* **93** 2972–6
[50] Kato Y, Shimada T, Shiraki Y and Komatsubara K F 1974 Electrical conductivity of disordered layers in GaAs crystal produced by ion implantation *J. Appl. Phys.* **45** 1044–9
[51] Wendler E and Wesch W 2016 Primary processes of damage formation in semiconductors *Ion Beam Modification of Solids: Ion-Solid Interaction and Radiation Damage* ed W Wesch and E Wendler (Berlin: Springer International Publishing) pp 189–241 ch 5
[52] Frodason Y K, Johansen K M, Bjørheim T S, Svensson B G and Alkauskas A 2017 Zn vacancy as a polaronic hole trap in ZnO *Phys. Rev.* B **95** 094105
[53] Pal S *et al* 2018 Clustered vacancies in ZnO: chemical aspects and consequences on physical properties *J. Phys. D: Appl. Phys.* **51** 105107
[54] Holston M S, Golden E M, Kananen B E, McClory J W, Giles N C and Halliburton L E 2016 Identification of the zinc–oxygen divacancy in ZnO crystals *J. Appl. Phys.* **119** 145701
[55] Zubiaga A, Tuomisto F, Coleman V A, Tan H H, Jagadish C, Koike K, Sasa S, Inoue M and Yano M 2008 Mechanisms of electrical isolation in O^+-irradiated ZnO *Phys. Rev.* B **78** 035125
[56] Tuomisto F, Saarinen K, Look D C and Farlow G C 2005 Introduction and recovery of point defects in electron-irradiated ZnO *Phys. Rev.* B **72** 085206
[57] Johansen K M, Tuomisto F, Makkonen I and Vines L 2017 Formation of Zn- and O-vacancy clusters in ZnO through deuterium annealing *Mater. Sci. Semicond. Process.* **69** 23–7 ZnO-based materials and applications
[58] Reunchan P, Zhou X, Limpijumnong S, Janotti A and Van de Walle C G 2011 Vacancy defects in indium oxide: an *ab initio* study *Curr. Appl. Phys.* **11** S296–300
[59] Ágoston P, Albe K, Nieminen R M and Puska M J 2009 Intrinsic *n*-type behavior in transparent conducting oxides: a comparative hybrid-functional study of In_2O_3, SnO_2, and ZnO *Phys. Rev. Lett.* **103** 245501

[60] Buckeridge J *et al* 2018 Deep vs shallow nature of oxygen vacancies and consequent *n*-type carrier concentrations in transparent conducting oxides *Phys. Rev. Mater.* **2** 054604

[61] Korhonen E, Tuomisto F, Gogova D, Wagner G, Baldini M, Galazka Z, Schewski R and Albrecht M 2015 Electrical compensation by Ga vacancies in Ga_2O_3 thin films *Appl. Phys. Lett.* **106** 242103

[62] Polyakov A Y *et al* 2018 Defects responsible for charge carrier removal and correlation with deep level introduction in irradiated β-Ga_2O_3 *Appl. Phys. Lett.* **113** 092102

[63] Farzana E, Chaiken M F, Blue T E, Arehart A R and Ringel S A 2019 Impact of deep level defects induced by high energy neutron radiation in β-Ga_2O_3 *APL Mater.* **7** 022502

[64] Gupta S, Singh F, Lalla N P and Das B 2017 Swift heavy ion irradiation induced modifications in structural, microstructural, electrical and magnetic properties of Mn doped SnO_2 thin films *Nucl. Instrum. Methods Phys. Res. Sect. B: Beam Interact. Mater. Atoms* **400** 37–57

[65] Janotti A and Van de Walle C G 2011 LDA + U and hybrid functional calculations for defects in ZnO, SnO_2, and TiO_2 *Phys. Status Solidi b* **248** 799–804

[66] Swallow J E N, Varley J B, Jones L A H, Gibbon J T, Piper L F J, Dhanak V R and Veal T D 2019 Transition from electron accumulation to depletion at β-Ga_2O_3 surfaces: the role of hydrogen and the charge neutrality level *APL Mater.* **7** 022528

[67] Burbano M, Scanlon D O and Watson G W 2011 Sources of conductivity and doping limits in CdO from hybrid density functional theory *J. Am. Chem. Soc.* **133** 15065–72

Paper II

Fermi level controlled point defect balance in ion irradiated indium oxide

II

Journal of Applied Physics ARTICLE scitation.org/journal/jap

Fermi level controlled point defect balance in ion irradiated indium oxide

Cite as: J. Appl. Phys. **130**, 085703 (2021); doi: 10.1063/5.0062135
Submitted: 2 August 2021 · Accepted: 7 August 2021 ·
Published Online: 24 August 2021

Jon Borgersen,[1,a)] Klaus Magnus Johansen,[1] Lasse Vines,[1] Holger von Wenckstern,[1,2] Marius Grundmann,[2] and Andrej Yu. Kuznetsov[1,b)]

AFFILIATIONS

[1]Department of Physics and Centre for Materials Science and Nanotechnology, University of Oslo, Oslo, Norway
[2]Felix Bloch Institute for Solid State Physics, Universität Leipzig, Leipzig, Germany

[a)]**Author to whom correspondence should be addressed:** jonborg@fys.uio.no
[b)]andrej.kuznetsov@fys.uio.no

ABSTRACT

Fermi level controlled point defect balance is demonstrated in ion irradiated indium oxide (In_2O_3). Specifically, our observations can be sub-divided into the formation of isolated Frenkel pairs and secondary defects, correlated with an increase and decrease in resistance, respectively. Importantly, by considering the net charge contribution from the most energetically stable Frenkel pair configurations, we explain the data trends for low doses and determine an upper limit for the Fermi level pinning. Moreover, by comparing the corresponding number of generated carriers with the ballistic defect generation rates, we estimate the dynamic annealing efficiency. Further irradiation toward higher doses is consistent with the buildup of secondary defects. As such, the present data may be of practical use in a variety of In_2O_3 device applications requiring predictions of its radiation tolerance. In a broader perspective, the present methodology may be valuable for benchmarking defect simulation data in semiconductors in general.

I. INTRODUCTION

Intrinsic point defects and their complexes are of paramount importance for functionalization of materials.[1] In semiconductors, the formation energy of a given defect depends on its charge state, which is in turn governed by the position of the Fermi level (E_F).[2] Moreover, the charge transition levels of the defects determine the energy position of the corresponding carrier traps in the bandgap.[2] These effects are very prominent in compound semiconductors in general and is an active research topic in the semiconducting oxides. The intrinsic defects are known to exhibit donor and acceptor behavior, significantly affecting the free carrier concentration in oxides,[2] e.g., In_2O_3.[3] Changes in the intrinsic defect balance can thus shift the E_F and, with sufficiently high defect concentrations, E_F can be pinned at a material dependent energy position often referred to as the charge neutrality level.[4–6] All these aspects are of paramount importance in applications, in particular, considering the radiation tolerance of the corresponding components.

Recent progress in defect modeling has enabled instructive theoretical predictions of the E_F-control of defect charge states.[7] Corresponding experimental discriminations are, however, complicated by collective contributions from intrinsic defects, impurities, and defect complexes. Meanwhile, electron- or ion irradiation is an excellent methodology to manipulate the intrinsic point defect balance in a controlled manner.[8] If samples are irradiated at sufficiently low temperatures and characterization performed *in situ*, the primary recoils, i.e., vacancies and self-interstitials, can be probed as individual species in the lattice as a function of the irradiation parameters since annealing is significantly suppressed.[9] In this context, *in situ* resistance measurements as a function of the irradiation dose have recently unveiled interesting correlations in oxide semiconductors.[10,11] However, even though Refs. 10 and 11 have investigated a range of different materials (ZnO, CdO, SnO_2, Ga_2O_3 and In_2O_3), a direct unambiguous demonstration of the dynamic E_F-control over the point defect balance is missing.

To address the challenge, we fabricated a set of In_2O_3 samples with initial resistances ranging from insulating to highly conductive, implying E_F-variations in an otherwise identical matrix. Defects were introduced by silicon ion irradiations at 50 K, and *in situ* resistance measurements as a function of the accumulated ion

dose were performed. The resistance evolution exhibited systematic trends, interpreted in terms of the E_F-effect governing the point defect balance, consistently with theoretical predictions from the literature.[12] Our interpretations were consistent with these theoretical predictions both for the low and high dose ranges, associated with the formation of isolated Frenkel pairs and secondary defects, respectively. Moreover, we used the data to calculate the dynamic annealing rate for Frenkel pairs in In_2O_3. As such, the present data may be of practical use in a variety of In_2O_3 device applications requiring predictions for the radiation tolerance.[13] Concurrently, in a more general perspective, these data provide an example of direct verification of the theoretical defect simulation data, and this methodology may be applicable for a wide range of semiconductors on demand.

II. EXPERIMENTS

Nominally undoped, as well as 1% Mg, 0.5% Mg, and 1% Sn doped In_2O_3 films were grown on c-plane sapphire substrates by pulsed laser deposition applying high purity targets. Additionally, a commercial 10% Sn doped In_2O_3 film deposited on a glass substrate was obtained. The samples were labeled A–E; see Table I. Before and after irradiation, all samples were measured in the van der Pauw geometry using a Lake Shore 7604 temperature dependent Hall (TDH) effect setup. The applied magnetic field was 1 T, and all samples were measured over a temperature range from 20 to 300 K in steps of 10 K (see Sec. I in the supplementary material). The 50 K electron concentrations n are listed in Table I together with corresponding E_F-values calculated using a standard formalism (see Sec. II in the supplementary material).

The samples were irradiated using 3 MeV Si^{2+} ions in an NEC tandem ion accelerator. Silicon ions were employed as they are reasonably heavy, thereby generating a large number of defects per ion, and as they allow high dose rates to be obtained. The SRIM code[14] was used to calculate both the projected range of the ions and the total number of generated Frenkel pairs. The displacement energy of both indium and oxygen was set to 15 eV,[10,15,16] yielding a projected range of ~1.5 μm, i.e., well within the substrate, confirmed by secondary ion mass spectrometry (SIMS) profiling. The changes occurring in the In_2O_3 films are thus attributed to the radiation induced intrinsic defects, excluding chemical or structural effects of the implanted silicon ions. Examples of SRIM simulations and SIMS profiles are included in Sec. III of the supplementary material.

Resistance data were collected by *in situ* current–voltage (IV) measurements at 50 K using a Keithley 6487 voltage source/picoammeter. For samples A–D, the voltage was swept from −2 to +2 V at each data point while, in order to limit the current through the highly conductive sample E, this sample was measured over a reduced voltage range of −1 to +1 V. At each voltage step, the current was recorded and the resistance calculated from the slope of the current–voltage curve. No sign of non-ohmic behavior was observed at any data point. After the as-grown data point, these measurements were performed starting at a dose of 10^{12} cm^{-2}, with gradually increasing dose intervals up to the maximum dose of 10^{17} cm^{-2}. In order to correlate the data with the charge states of the generated intrinsic defects, the resistance values were first converted to carrier concentrations by assuming constant mobility. For samples C–E, the corresponding as-grown mobility was used. For samples A and B, the as-grown mobility was unknown; hence, the corresponding mobility measured after irradiation was utilized for these samples. We justify the constant-mobility approximation by the observation that the resistance varies over orders of magnitude, i.e., far more than what could be expected from changing the mobility (see Sec. I in the supplementary material). Orders of magnitude changes are, however, realistic for the carrier concentration. The carrier concentration after each dose n_d was calculated by scaling the product of the as-grown carrier concentration $n_{as-grown}$ and resistance $R_{as-grown}$ by the measured resistance R_d,

$$n_d = n_{as-grown}\frac{R_{as-grown}}{R_d}.$$

Subsequently, the corresponding Fermi levels were calculated from the carrier concentrations by a standard formalism.[17]

III. RESULTS AND DISCUSSION

Figure 1 summarizes the resistance data as a function of the accumulated irradiation dose, where the top horizontal axis depicts the corresponding vacancy concentration calculated from SRIM. The first data point for each sample shows the resistance measured *in situ* before irradiation. The initial resistance decreased with increasing Sn content [samples C–E in Fig. 1(a)]. Samples doped with Mg (A and B) initially exhibited resistances outside the measurement range of our instrument, and these values are plotted as 3×10^{10} Ω as a lower limit. Irradiating samples A and B to doses of 10^{15} and 3×10^{14} cm^{-2}, respectively, enabled measurement of their

TABLE I. Sample labels, corresponding dopants as well as 50 K carrier concentrations (n) and Fermi levels (E_F) in three characteristic states: as-grown, at R_{max}, and after the final irradiation. For samples A and B, R_{max} refers to the first data point within the measurement range.

No.	Size (mm × mm × nm)	Dopant	As-grown		At R_{max}		After irradiation	
			n (cm^{-3})	E_F (eV)	n (cm^{-3})	E_F (eV)	n (cm^{-3})	E_F (eV)
A	5 × 5 × 1100	1% Mg	…	…	3.6×10^{12}	−0.05	2.8×10^{18}	0.04
B	5 × 5 × 220	0.5% Mg	…	…	2.9×10^{13}	−0.04	6.5×10^{19}	0.28
C	10 × 10 × 800	None	1.3×10^{19}	0.11	9.2×10^{17}	0.02	5.0×10^{19}	0.24
D	5 × 5 × 500	1% Sn	9.0×10^{19}	0.34	7.8×10^{18}	0.08	7.7×10^{19}	0.31
E	5 × 5 × 50	10% Sn	1.6×10^{21}	1.34	4.8×10^{20}	0.81	1.3×10^{21}	1.26

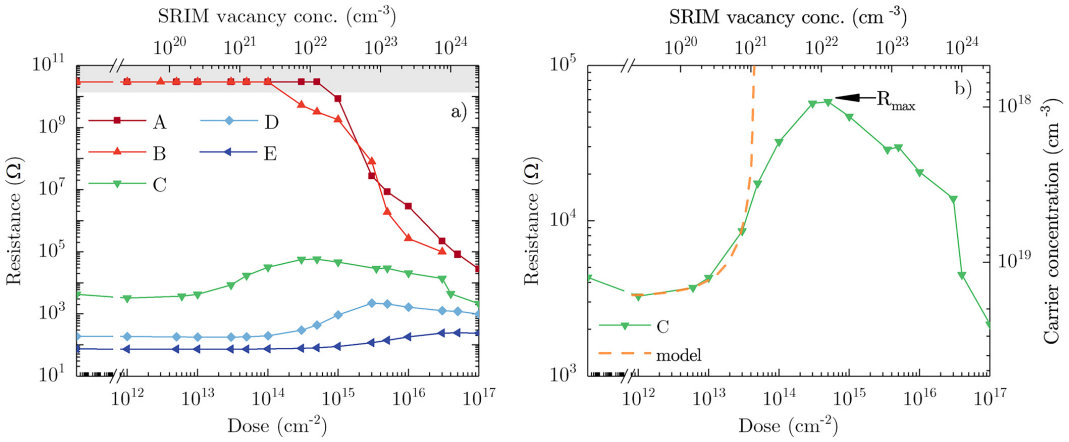

FIG. 1. (a) Resistance evolution as a function of the accumulated ion dose. All measurements were performed *in situ* at 50 K with the ion beam blanked. (b) Magnified view of sample C along with predicted values from the model. The top horizontal axes show simulated vacancy concentrations from SRIM.

first experimental resistance points, adopted as maximum resistance values (R_{max}) for these samples. Subsequent irradiation resulted in a continuously decreasing resistance, clearly indicating the accumulation of donor-like intrinsic defects.

Samples C–E demonstrated qualitatively common trends in the resistance evolution. For these samples, Fig. 1(a) shows that the resistance initially increases up to a maximum value (R_{max}), followed by a decrease. This trend is clear for samples C and D and emerging for sample E. Since the trend is most evident for sample C, we will focus on this sample in the following. The corresponding data are shown on a magnified scale in Fig. 1(b), where the left and right vertical axes plot the resistance and the calculated carrier concentration, respectively. Figure 1(b) also contains a plot of the predicted resistance values for the low-dose region under the assumption of no E_F pinning or complex formation.

Already, qualitative consideration of the non-monotonic dose dependence in Fig. 1(b) suggests an interesting scenario, subdividing the defect accumulation into the distinct low- and high dose ranges. At low doses, it is reasonable to assume that the irradiation ballistically generates primary defects on both the In- and O-sublattices, i.e., Frenkel pairs of indium vacancies (V_{In}), interstitials (In_i), oxygen vacancies (V_O), and interstitials (O_i). Moreover, due to the low temperature and limited concentration, these defects do not build secondary defect complexes at low doses. In contrast, at high doses, the increased primary defect concentration enables the formation of secondary defects, e.g., indium and oxygen antisites (In_O and O_{In}, respectively).

Accounting for the fact that intrinsic defects in oxides act as donors or acceptors, qualitative scenarios explaining the data in Fig. 1 may be readily proposed.[11] Importantly, by comparing samples exhibiting different E_F-values selected for the present study, we go beyond such qualitative analysis and unveil interesting correlations. Guided by theory,[12] we illustrate our analysis for the defect accumulation in the low-dose regime by Fig. 2. Panel (a) shows the theoretical E_F as a function of carrier concentration in In_2O_3 at 50K (solid line) as well as E_F-values calculated from our resistance data, while panel (b) illustrates charge transition levels for the generally most energetically stable configurations of primary defects in In_2O_3 as a function of E_F [12,18] relative to the conduction band minimum E_c. Notably, $O_{i,\,split}$ refers to the oxygen split interstitial, while the superscripts a and b on In_i and V_{In} refer to the corresponding inequivalent sites in the indium sublattice. It should be noted that the O_i, In_i and V_{In} can also exist in other configurations, but for the majority of the considered E_F range, these are less energetically favorable and disregarded in the following. The V_O has both the 0/+ and +/++ charge transitions in the relevant E_F-interval, whereas In_i^a has the +/++ transition. For $O_{i,\,split}$ and V_{In}^b there are no charge transitions in the E_F-range probed in our experiments; hence, these defects remain in their respective neutral and triply negative states for the considered E_F-values. The arrow in Fig. 2 highlights the logic of our analysis for sample C. It can be seen that the initial $n = 1.3 \times 10^{19}$ cm^{-3} corresponds to $E_F = E_c + 110$ meV. For this E_F Fig. 2(b) shows that both V_O and $O_{i,\,split}$ are neutral, and generation of these defects does not change the carrier concentration. On the indium sublattice, the In_i and V_{In} have charges +1 and −3, respectively. Hence, introducing both one indium- and one oxygen Frenkel pair results in trapping of two electrons from the conduction band. As the dose is increased, this process will cause a decrease of E_F, as illustrated by the vertical color graded arrow, corresponding with the increasing resistance observed in Fig. 1. Furthermore, upon reaching $E_F = E_c + 60$ meV, corresponding to the 0/+ charge transition for V_O, the net charge of one indium- and one oxygen Frenkel pair together becomes neutral,

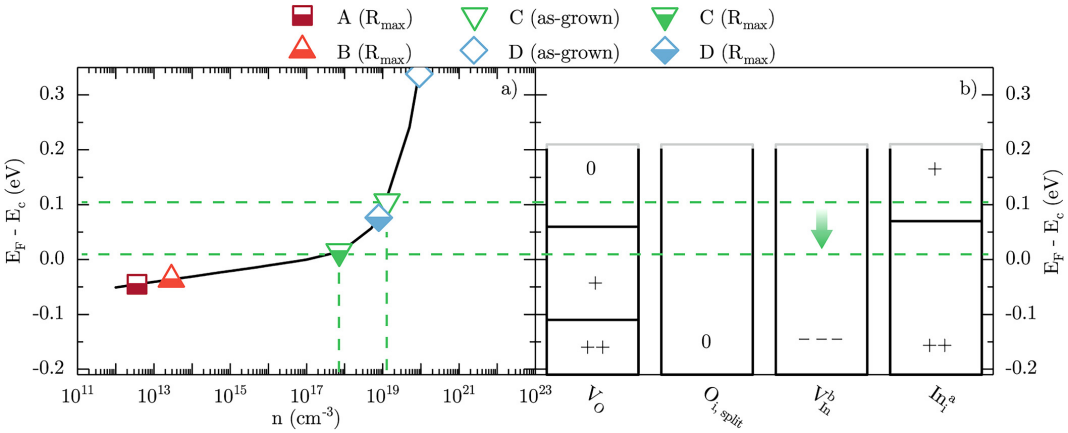

FIG. 2. (a) Fermi levels relative to the conduction band minimum for samples A–D at 50 K. The line represents the model for the Fermi levels as given in the supplementary material. (b) Thermodynamic charge states and their transition levels for selected primary defects in In_2O_3 as calculated by hybrid DFT in Ref. 12. The dashed lines serve as guides to the eye for important Fermi levels and carrier concentrations, while the arrow indicates the change in E_F with irradiation of sample C. The gray lines at the top of each column in panel (b) illustrate that charge states at higher Fermi levels are unknown.

associated with the E_F pinning at this energy. However, R_{max} for sample C corresponds to a lower E_F of $E_c + 20$ meV, reached at a dose of 5×10^{14} cm^{-2}. Thus, we adopt this as a lower limit of the experimental pinning level.

It may be instructive to consider the same logic for sample D in Fig. 2, following its resistance evolution from the initial state to R_{max} in Fig. 1. For sample D, R_{max} corresponds to $E_F = E_c + 80$ meV, i.e., 20 meV above the theoretical V_O 0/+ position,[12] and occurs at a dose

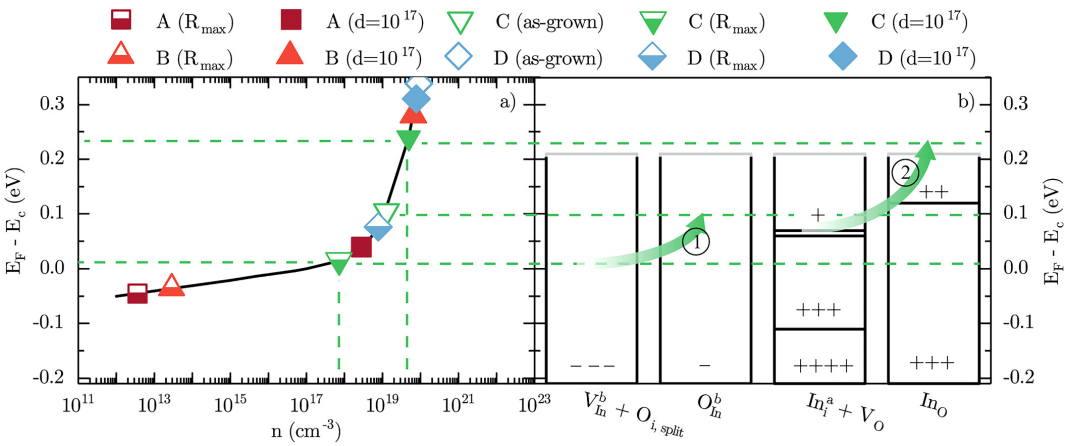

FIG. 3. (a) Fermi levels of samples A–D at important doses. (b) Defect states for antisites and the combination of their constituent primary defects.[12] The arrows indicate the irradiation induced formation of oxygen (1) and indium (2) antisites, while the dashed lines highlight important carrier concentrations and Fermi levels. The gray lines at the top of each column illustrate that charge states at higher Fermi levels are unknown.

of 3×10^{15} cm^{-2}. The discrepancy between these two samples may be attributed to the difference in the antisite concentration at R_{max}. In line with the model, sample E also demonstrated a trend of increasing resistance as a function of accumulated dose.

Although quantitative resistances are not available for samples A and B in the low-dose region, their respective R_{max} values represent a lower limit, and the corresponding Fermi levels are shown in Fig. 2(a). From Fig. 2(b), it is seen that, at these Fermi levels, equal concentrations of indium and oxygen Frenkel pairs have a net neutral charge state. Hence, at low doses, irradiation should not produce any change in the carrier concentration, in qualitative agreement with the data for these two samples presented in Fig. 1.

For the low-dose regime, we have further extracted the survival rate of Frenkel pairs in collision cascades at 50 K. This was performed by making a linear fit of the SRIM vacancy concentration to the rising flank of the resistance curve for sample C, as shown in Fig. 1(b). From the slope of the fit curve, a survival rate of ~1.4% was extracted. Thus, the dynamic annealing rate of 98.6% is in agreement with literature estimates for other radiation hard materials.[19–21]

Extending the approach toward the high dose regime, the decreasing resistance in Fig. 1 is explained by reaching sufficiently high concentrations of Frenkel pairs to enable a buildup of secondary defects. Figure 3 illustrates the analysis taking into account formation of antisites. Specifically, columns 1 and 3 of Fig. 3(b) show the combined charge state of one V_{In}^{b} and one $O_{i,\,split}$ and one In_i^a and one V_O, respectively [i.e., the sums of columns 2 and 3 and 1 and 4 from Fig. 2(b)]. Columns 2 and 4 of Fig. 3(b) show the charge states of the antisites formed from the respective defect combinations. Considering sample C at E_F corresponding to R_{max} it is seen from Fig. 3 that forming O_{In}^{b} from a combination of V_{In}^{b} and $O_{i,\,split}$, as indicated by arrow 1, will change the charge balance of the defect population from 0 to +2 per antisite. This releases two electrons to the conduction band, shifting the Fermi level upward and consequently decreasing the resistance. At $E_F = E_c + 70$ meV, the total charge of the oxygen antisite and the remaining primary defects from the original two Frenkel pairs (one In_i^a and one V_O) are again neutral. Furthermore, forming indium antisites from In_i^a and V_O, as indicated by arrow 2, can continue to shift the Fermi level up to at least $E_c + 210$ meV. Above this level, no theoretical data exist for the charge states, but assuming the states to be constant, this can explain the resistance decrease to the final dose point. The same reasoning holds in full also for samples A, B, and D.

IV. CONCLUSIONS

In conclusion, we report compelling experimental evidence of the E_F-controlled point defect balance in In_2O_3 subjected to ion irradiation. The observations, sub-divided into two regions of monotonically increasing and decreasing resistance, were correlated with the formation of individual Frenkel pairs and antisites, respectively. Importantly, by considering the net charge contribution from the most energetically stable Frenkel pair configurations, the data trends at low doses were explained. In particular, an upper limit for the E_F-pinning was determined and correlated with the V_O 0/+ transition level predicted from the literature. Moreover, by fitting the experimental results with the ballistic defect generation rate, a dynamic annealing rate of 98.6% was estimated. Further irradiation toward higher doses leads to a buildup of donor-like secondary defects lowering the resistance. As such, the presented data may be of practical use in a variety of In_2O_3 device applications where predictions of the radiation tolerance are required. Concurrently, in a more general perspective, we demonstrated the use of *in situ* resistance monitoring as a valuable methodology for benchmarking semiconductor defect simulation data.

SUPPLEMENTARY MATERIAL

See the supplementary material that contains results from secondary ion mass spectrometry and temperature dependent Hall effect measurements, as well as simulated depth profiles of vacancies and implanted ions and the procedure used for calculating carrier concentrations from the resistance measurements.

ACKNOWLEDGMENTS

Helge Kristiansen at Conpart AS is acknowledged for supplying sample E. The Research Council of Norway is acknowledged for the support to the Norwegian Micro- and Nano-Fabrication Facility, NorFab, Project No. 295864. The University of Oslo FOXHOUND project, the Norwegian Nano Network, and the UiO: Energy are gratefully acknowledged for financial support.

DATA AVAILABILITY

The data that support the findings of this study are available from the corresponding author on reasonable request.

REFERENCES

[1]F. C.-C. Ling, S. Zhou, and A. Kuznetsov, *Defects in Functional Materials* (World Scientific, 2020).
[2]M. D. McCluskey and E. E. Haller, *Dopants and Defects in Semiconductors*, 2nd ed. (CRC Press, 2018).
[3]T. Tomita, K. Yamashita, Y. Hayafuji, and H. Adachi, "The origin of n-type conductivity in undoped In_2O_3," Appl. Phys. Lett. **87**(5), 051911 (2005).
[4]P. D. C. King, T. D. Veal, D. J. Payne, A. Bourlange, R. G. Egdell, and C. F. McConville, "Surface electron accumulation and the charge neutrality level in In_2O_3," Phys. Rev. Lett. **101**, 116808 (2008).
[5]C. G. Van de Walle and J. Neugebauer, "Universal alignment of hydrogen levels in semiconductors, insulators and solutions," Nature **423**, 626–628 (2003).
[6]A. Zunger, "Practical doping principles," Appl. Phys. Lett. **83**, 57–59 (2003).
[7]C. Freysoldt, B. Grabowski, T. Hickel, J. Neugebauer, G. Kresse, A. Janotti, and C. G. Van de Walle, "First-principles calculations for point defects in solids," Rev. Mod. Phys. **86**, 253–305 (2014).
[8]P. T. Neuvonen, L. Vines, B. G. Svensson, and A. Y. Kuznetsov, "Intrinsic point-defect balance in self-ion-implanted ZnO," Phys. Rev. Lett. **110**, 015501 (2013).
[9]G. D. Watkins, "EPR studies of lattice defects in semiconductors," in *Defects and Their Structure in Nonmetallic Solids*, 1st ed., edited by B. Henderson (Springer US, 1976), Chap. 7, pp. 203–220.
[10]L. Vines, C. Bhoodoo, H. von Wenckstern, and M. Grundmann, "Electrical conductivity of In_2O_3 and Ga_2O_3 after low temperature ion irradiation; implications for instrinsic defect formation and charge neutrality level," J. Phys.: Condens. Matter **30**(2), 025502 (2018).
[11]J. Borgersen, L. Vines, Y. K. Frodason, A. Kuznetsov, H. von Wenckstern, M. Grundmann, M. Allen, J. Zúñiga-Pérez, and K. M. Johansen, "Experimental exploration of the amphoteric defect model by cryogenic ion

irradiation of a range of wide band gap oxide materials," J. Phys.: Condens. Matter **32**, 415704 (2020).
[12]I. Chatratin, F. P. Sabino, P. Reunchan, S. Limpijumnong, J. B. Varley, C. G. Van de Walle, and A. Janotti, "Role of point defects in the electrical and optical properties of In_2O_3," Phys. Rev. Mater. **3**, 074604 (2019).
[13]H. von Wenckstern, "Group-III sesquioxides: Growth, physical properties and devices," Adv. Electron. Mater. **3**(9), 1600350 (2017).
[14]J. F. Ziegler, J. P. Biersack, and U. Littmark, *The Stopping and Range of Ions in Solids* (Pergamon Press, New York, 1985).
[15]J. J. Loferski and P. Rappaport, "Radiation damage in Ge and Si detected by carrier lifetime changes: Damage thresholds," Phys. Rev. **111**, 432–439 (1958).
[16]B. G. Svensson, C. Jagadish, A. Hallén, and J. Lalita, "Generation of vacancy-type point defects in single collision cascades during swift-ion bombardment of silicon," Phys. Rev. B **55**, 10498–10507 (1997).
[17]R. Kim and M. Lundstrom, "Notes on Fermi-Dirac integrals," 3rd ed., arXiv:0811.0116v4 (2011).
[18]Defect charge states for Fermi levels above $E_c + 210$ meV have not been calculated theoretically, and, for simplicity, we assume no new transitions to occur above this energy.
[19]S. O. Kucheyev, J. S. Williams, C. Jagadish, J. Zou, C. Evans, A. J. Nelson, and A. V. Hamza, "Ion-beam-produced structural defects in ZnO," Phys. Rev. B **67**, 094115 (2003).
[20]A. Hupfer, C. Bhoodoo, L. Vines, and B. G. Svensson, "Formation and annihilation of E4 centers in ZnO: Influence of hydrogen," J. Appl. Phys. **119**(18), 181506 (2016).
[21]B. G. Svensson, C. Jagadish, and J. S. Williams, "Generation rate of point defects in silicon irradiated by MeV ions," Nucl. Instrum. Methods Phys. Res., Sect. B **80-81**, 583–586 (1993).

Paper III

Origin of enhanced conductivity in low dose ion irradiated oxides

III

Origin of enhanced conductivity in low dose ion irradiated oxides

Cite as: AIP Advances 13, 015211 (2023); doi: 10.1063/5.0134699
Submitted: 26 November 2022 • Accepted: 22 December 2022 •
Published Online: 12 January 2023

View Online Export Citation CrossMark

Jon Borgersen,[1,a)] Robert Karsthof,[1] Vegard Rønning,[1] Lasse Vines,[1] Holger von Wenckstern,[1,2] Marius Grundmann,[2] Andrej Yu Kuznetsov,[1] and Klaus Magnus Johansen[1]

AFFILIATIONS

[1]Department of Physics and Centre for Materials Science and Nanotechnology, University of Oslo, Oslo, Norway
[2]Felix Bloch Institute for Solid State Physics, Universität Leipzig, Leipzig, Germany

[a)]Author to whom correspondence should be addressed: jonborg@fys.uio.no

ABSTRACT

Significant resistivity variations have previously been observed in oxides subjected to relatively low ion irradiation doses, nominally insufficient to generate the amount of bulk defects needed to explain the phenomena. In an effort to unveil the underlying mechanisms, we performed a systematic comparative study of the resistivity evolution in In_2O_3-based oxides as a function of low ion doses and ultraviolet (UV) illumination, observing striking correlations. Specifically, we found that irradiation with ~3×10^{12} Si/cm^2 and ~18 h UV exposure result in similar resistivity drops, interpreted in terms of irradiation/illumination assisted desorption of oxygen containing species from the surface. This was further proven by post-irradiation exposure of one of the samples to an oxygen atmosphere partially restoring the resistivity. Combining the present results with literature data, we conclude that the radiation tolerance of In_2O_3-based and similar oxides depends on the surface charge modifications, individual defect contributions, and contributions from defect complexes at low, intermediate, and high doses, respectively.

I. INTRODUCTION

An intriguing property of certain wide bandgap semiconductors, such as InAs, InN, In_2O_3, SnO_2, and ZnO, is the accumulation of electrons at the surface,[1–4] in the form of a so-called surface electron accumulation layer (SEAL). While the surface of most other semiconductor materials tends to be electron deficient with respect to the bulk,[5] the SEAL results from a downward bending of the conduction band edge toward the surface. In ZnO, adsorbed hydrogen,[6] oxygen,[7,8] and OH groups[6] have all been found to correlate with a downward band bending, and for this specific material, the surface polarization also comes into play.[6] For In_2O_3, theoretical calculations have shown that an oxygen vacancy situated at the surface of the material may act as a shallow donor and could be the reason for the downward band bending.[9] In other words, there is currently no consensus of the source of the band bending, and the formation of the SEAL is not necessarily explained by one single model. However, it is clear that oxygen species adsorbing to the surface, e.g., from exposure to oxygen gas, ozone, or oxygen plasma, can remove the downward band bending and even bend the conduction band upward, effectively removing the SEAL.[10–12] Interestingly, this effect can be reversed by exposure to ultraviolet (UV) light[12,13] or thermal annealing in vacuum,[14] which restores the downward surface band bending through desorption of the adsorbed molecules. These processes form the working principle of conductometric gas sensors.[10,15] Acceptor doping has been shown to be beneficial in increasing the sensitivity of a gas sensor through reducing the bulk contribution to the conductivity.[10] However, at a given acceptor concentration, the Fermi level is shifted below the surface conduction band and effectively drains the surface of electrons, thereby removing the SEAL as a conduction channel.[10]

The downward band bending and the resulting SEAL for InAs, InN, In_2O_3, SnO_2, and ZnO, is often explained in terms of the unusually high bulk material charge neutrality level (CNL) in these materials.[5] In two recent studies, we utilized ion irradiation to study the evolution of the electrical properties of several wide bandgap oxide semiconductors as a function of increasing defect concentration, i.e., irradiation dose.[16,17] Interestingly, we found that, e.g.,

in In_2O_3, where the CNL is commonly assumed to be positioned above the conduction band minimum (CBM),[18] the introduction of a low concentration of Frenkel pairs on both sub-lattices increases the acceptor concentration in the material. This was interpreted in terms of the charge state imbalance of the In vacancy and In interstitial. It was found that the effective acceptor doping increases the resistance of the material by more than an order of magnitude. However, as the irradiation dose is increased the formation probability of defect complexes also increases. Specifically, the formation of indium- and oxygen antisites[19] changes the charge balance, resulting in the recovery of the highly conducting n-type material.

In general, it was found that the resistance increase observed at doses between 10^{13} and 5×10^{14} cm^{-2}, and the subsequent decrease at doses exceeding ~10^{15} cm^{-2} is controlled by the positions of the charge transition levels for the intrinsic primary defects and intrinsic defect complexes, respectively. Interestingly, when irradiating ZnO, SnO_2, In_2O_3, In_2O_3:Sn, or $(InGa)_2O_3$:Mg with ion doses <10^{13} cm^{-2}, an initial reduction of the resistance is observed. This reduction cannot be explained in terms of defect interaction in the bulk of the material because (i) the introduced defect concentration is much lower than the background doping and (ii) the introduced Frenkel pairs are net acceptors, which would lead to an increase, rather than a decrease, of the resistance.

In this work, we have studied the resistivity evolution in In_2O_3 when irradiated with low ion doses. We propose that the ion irradiation, similar to UV illumination, interacts with the surface and leads to the formation of a surface electron accumulation layer (SEAL). The SEAL acts as an additional conduction channel, resulting in a reduced resistance.

II. EXPERIMENTS

$(In_{1-x}Ga_x)_2O_3$:Mg with $x = 17\%$ and 1% Mg doping was deposited on a single 10×10 mm^2 electrically insulating c-plane sapphire substrate using pulsed laser deposition (PLD). This composition was selected as it has a high, but still measurable, resistivity in the as-grown state. After growth, the sample was laser cut into two nominally identical 5×10 mm^2 samples labeled A and C, having resistances of 5.72×10^8 and 6.22×10^8 Ω, respectively. The relatively small difference in resistance was attributed to minor variations in the sample dimensions and the sizes and positions of the contacts. In addition, an In_2O_3:Mg sample with 0.5% Mg doping was deposited by PLD in the same chamber on a nominally identical substrate and is labeled sample B.

Contacts were formed by soldering silver wires to each end of the samples using indium as solder metal, and Ohmic behavior was confirmed through current–voltage measurements from −1 to 1 V.

The subsequent experiments were carried out at a pressure on the order of 10^{-6} Torr in a vacuum chamber connected to an NEC tandem ion implanter. As the three samples would undergo different experiments, only a single sample was present in the chamber at any given time.

Before ion irradiation, samples A and B were exposed to 250 nm ultraviolet (UV) illumination for ~18 h in order to remove adsorbed atoms and molecules from the surface. Sample C acted as a reference sample and was held under the same vacuum conditions as samples A and B for a similar time, but was not exposed to the UV light. Each sample was then irradiated with 3 MeV Si^{2+} ions in several stages, and between each irradiation exposure, the resistance was measured *in situ* on a Keithley 6487 voltage source/picoammeter.

Following the irradiation of sample B to an accumulated dose of 5×10^{13} cm^{-2}, the surface was re-populated with adsorbates by exposure to 99.999% pure O_2 gas while monitoring its resistance.

III. RESULTS AND DISCUSSION

Figure 1 shows the resistance of samples A and B as function of time during 250 nm UV light illumination in high vacuum. Following an initial rapid decrease, the resistance of sample A is approaching a stable value of ~3.4×10^4 Ω. Relative to the initial value, this corresponds to a decrease of nearly four orders of magnitude over the course of the exposure, and is attributed to the removal of adsorbed atoms from the surface. These data are consistent with a downward surface band bending, as illustrated in Fig. 2, resulting in the formation of a SEAL through the release of electrons to the conduction band at, or close to, the surface. Sample B shows qualitatively similar behavior as sample A. Keeping sample C under the same conditions as samples A and B, but without the UV light exposure, causes its resistance to drop by a factor 2. That is, the vacuum has a far weaker effect on the resistance than the UV illumination that, following the above reasoning, shows that the UV light strongly promotes the desorption of surface adsorbates.

The resistance evolutions of samples A, B, and C as functions of irradiation dose are plotted in Fig. 3. Interestingly, for the illuminated samples (A and B), the ion irradiation has only a weak influence on the resistance in the measured dose range. Sample C, on the other hand, shows a dramatically different response to the ion irradiation. Irradiating this sample rapidly decreases its resistance, already from the first exposure. At a dose of ~3×10^{12} cm^{-2}, the resistance has dropped by 4 orders of magnitude from its as-grown value, consistent with In_2O_3 and ZnO samples reported in previous publications.[16,17] At these low doses, the bulk defect concentration introduced by the irradiation is too low to explain such a dramatic

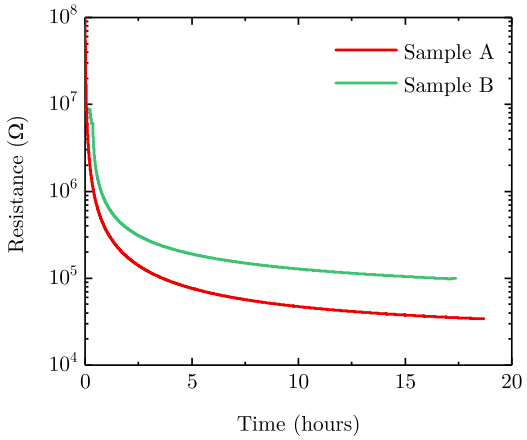

FIG. 1. The resistance evolution of samples A and B during 250 nm UV illumination.

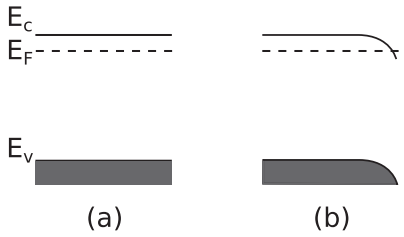

FIG. 2. Simplified illustration of the bulk and surface contributions to the band structure. (a) Flat band situation with surface saturated with adsorbates. (b) Removal of adsorbates by either UV-illumination or ion irradiation results in downward band bending at the surface.

resistivity drop. In Ref. 17, a concentration of 3.5×10^{17} cm^{-3} electrically active Frenkel pairs was estimated to have formed in In_2O_3 at a dose of 10^{12} cm^{-2}, i.e., more than one order of magnitude lower than the observed change in carrier concentration at this dose. Moreover, density functional theory (DFT)[19] proposes that the net charge state of Frenkel pairs forming in In_2O_3 at these Fermi levels is negative, i.e., the net generated defect population acts as acceptors, apparently contradicting the observed decrease in resistance. To reconcile the formation of bulk acceptor defects with the observed decrease in resistance, we look to the sample surface and its electron accumulation layer.[2] Comparing samples A and C, the similar response to overnight UV illumination and 3 MeV Si^{2+} irradiation may indicate that the effect originates from a common mechanism. In particular, removal of surface adsorbates is well established as the cause of the resistance decrease under UV illumination in the literature (see, e.g., Refs. 7 and 8 and references therein). Thus, we propose that a similar mechanism occurs also during ion irradiation.

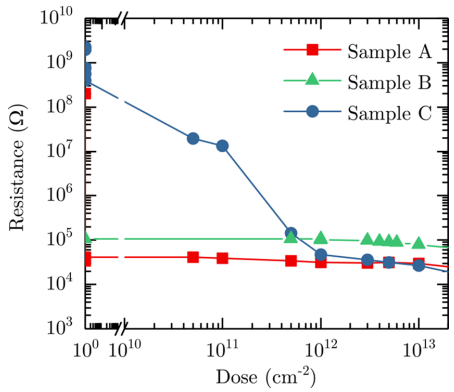

FIG. 3. Resistance of each sample as function of irradiation dose.

To further investigate the effect of surface adsorbates on the electrical properties of ion irradiated samples, the resistance of sample B was measured as a function of time during exposure to O_2 gas after ion irradiation to a dose of 5×10^{13} cm^{-2}. As shown in Fig. 4, the resistance initially increases rapidly when the gas is introduced, followed by a saturation stage. After 10 h the resistance has increased by a factor 5, and asymptotically approaches a stable value. This value is, however, still about a factor 30 lower than the original resistance of this sample, indicating either (a) that pure oxygen adsorbates are weaker electron traps than the species present on the surface during the original measurement or (b) that the ion irradiation has generated bulk donors. For pure indium oxide, the latter interpretation would be in conflict with our findings reported in Refs. 16 and 17, where the defects generated at a dose of 5×10^{13} cm^{-2} were found to be acceptors. However, the low Fermi level induced by the Mg doping of sample B could possibly make donor formation favorable already at this low dose.

The presented results show that the resistivity of In_2O_3 can be decreased both by UV illumination and ion irradiation, and subsequently increased by exposure to oxygen gas. Thus, we extend the model of defect concentration dependent resistivity presented in Refs. 16 and 17 by proposing that the resistivity reduction observed at ion doses $<10^{13}$ Si/cm^2 results from an irradiation induced downward surface band bending. Starting from a state where the surface is saturated with adsorbates and the valence-, conduction-, and Fermi levels are all flat, as illustrated schematically in Fig. 2(a), the downward band bending caused by removal of adsorbates is shown in Fig. 2(b).

With the addition of this analysis, our model for the defect concentration dependent resistance in oxides then contains three separate contributions: (i) an initial resistance decrease caused by surface modifications at low doses, (ii) a subsequent increase in

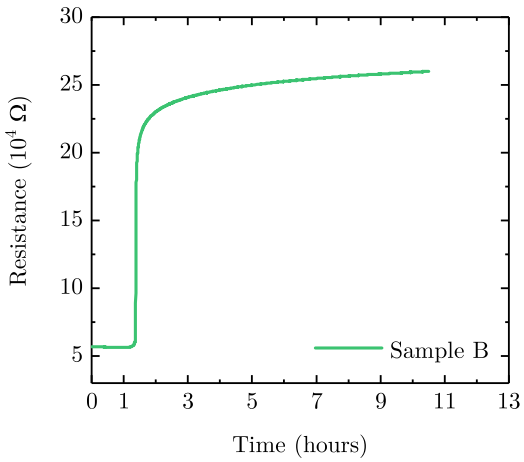

FIG. 4. Resistance of sample B during exposure to O_2 gas after irradiation. As the gas is introduced to the chamber between the 1 and 2 h marks the resistance initially increases sharply, before approaching a stable value.

resistance caused by individual point defects at intermediate doses, and (iii) a second resistance decrease due to the formation of defect complexes at high doses.

IV. CONCLUSIONS

Comparing the defect concentration dependent resistivity of In_2O_3 samples irradiated with and without prior UV illumination, the response to low dose irradiation is found to correlate with modifications of the surface properties of the samples. Specifically, the reduction in resistance at doses $\leq 10^{13}$ cm^{-2}, observed also in SnO_2 and ZnO,[16] can be explained by a downward band bending at the surface, enabling the establishment of a surface electron accumulation layer exhibiting a higher conductivity compared to that in the bulk.

The surface electron accumulation layer (SEAL) can be depleted by exposing the sample to O_2 gas, suggesting that adsorbed atoms or molecules flatten the bands and trap the delocalized conduction electrons.

The presented results complements the data on defect dependent resistivity collected in Refs. 16 and 17. The corresponding model then comprises three components, each with the possibility of affecting the resistivity, (i) modification of surface states at doses $\leq 10^{13}$ cm^{-2}, (ii) generation of individual bulk point defects at doses $\leq 10^{14}$ cm^{-2}, and (iii) agglomeration of point defects into complexes at higher doses. Depending on the net charge state of the defect population, each stage can increase or decrease the sample resistivity.

ACKNOWLEDGMENTS

The authors express their gratitude to Professor Terje G. Finstad and Dr. Simon Cooil for useful discussions. The Research Council of Norway is acknowledged for the support to the Norwegian Micro- and Nano-Fabrication Facility, NorFab, Project No. 295864, and the FOXHOUND project. The Norwegian Nano Network and UiO:Energy are gratefully acknowledged for financial support.

AUTHOR DECLARATIONS

Conflict of Interest

The authors have no conflicts to disclose.

Author Contributions

Jon Borgersen: Conceptualization (equal); Data curation (equal); Formal analysis (equal); Investigation (equal); Methodology (equal); Validation (equal); Visualization (equal); Writing – original draft (lead); Writing – review & editing (equal). **Robert Karsthof**: Data curation (equal); Formal analysis (equal); Investigation (equal); Methodology (equal); Validation (equal); Writing – review & editing (equal). **Vegard Rønning**: Data curation (equal); Investigation (equal); Methodology (equal); Writing – review & editing (equal). **Lasse Vines**: Conceptualization (equal); Formal analysis (equal); Supervision (equal); Validation (equal); Writing – review & editing (equal). **Holger von Wenckstern**: Conceptualization (equal); Writing – review & editing (equal). **Marius Grundmann**: Funding acquisition (equal); Writing – review & editing (equal). **Andrej Yu. Kuznetsov**: Conceptualization (equal); Formal analysis (equal); Project administration (equal); Supervision (equal); Writing – review & editing (equal). **Klaus Magnus Johansen**: Conceptualization (equal); Data curation (equal); Project administration (equal); Supervision (equal); Visualization (equal); Writing – review & editing (equal).

DATA AVAILABILITY

The data that support the findings of this study are available from the corresponding author upon reasonable request.

REFERENCES

[1] A. Papadogianni, J. Rombach, T. Berthold, V. Polyakov, S. Krischok, M. Himmerlich, and O. Bierwagen, "Two-dimensional electron gas of the In_2O_3 surface: Enhanced thermopower, electrical transport properties, and reduction by adsorbates or compensating acceptor doping," Phys. Rev. B **102**, 075301 (2020).
[2] P. D. C. King, T. D. Veal, D. J. Payne, A. Bourlange, R. G. Egdell, and C. F. McConville, "Surface electron accumulation and the charge neutrality level in In_2O_3," Phys. Rev. Lett. **101**, 116808 (2008).
[3] M. Noguchi, K. Hirakawa, and T. Ikoma, "Intrinsic electron accumulation layers on reconstructed clean InAs(100) surfaces," Phys. Rev. Lett. **66**, 2243–2246 (1991).
[4] I. Mahboob, T. D. Veal, C. F. McConville, H. Lu, and W. J. Schaff, "Intrinsic electron accumulation at clean InN surfaces," Phys. Rev. Lett. **92**, 036804 (2004).
[5] P. D. C. King and T. D. Veal, "Conductivity in transparent oxide semiconductors," J. Phys.: Condens. Matter **23**(33), 334214 (2011).
[6] R. Heinhold, G. T. Williams, S. P. Cooil, D. A. Evans, and M. W. Allen, "Influence of polarity and hydroxyl termination on the band bending at ZnO surfaces," Phys. Rev. B **88**, 235315 (2013).
[7] J. Bao, I. Shalish, Z. Su, R. Gurwitz, F. Capasso, X. Wang, and Z. Ren, "Photoinduced oxygen release and persistent photoconductivity in ZnO nanowires," Nanoscale Res. Lett. **6**(1), 404 (2011).
[8] M. Madel, F. Huber, R. Mueller, B. Amann, M. Dickel, Y. Xie, and K. Thonke, "Persistent photoconductivity in ZnO nanowires: Influence of oxygen and argon ambient," J. Appl. Phys. **121**, 124301 (2017).
[9] K. H. L. Zhang, R. G. Egdell, F. Offi, S. Iacobucci, L. Petaccia, S. Gorovikov, and P. D. C. King, "Microscopic origin of electron accumulation in In_2O_3," Phys. Rev. Lett. **110**, 056803 (2013).
[10] J. Rombach, O. Bierwagen, A. Papadogianni, M. Mischo, V. Cimalla, T. Berthold, S. Krischok, and M. Himmerlich, "Electrical conductivity and gas-sensing properties of Mg-doped and undoped single-crystalline In_2O_3 thin films: Bulk vs. surface," Procedia Eng. **120**, 79–82 (2015); part of Special Issue: Eurosensors 2015.
[11] C. Wang, L. Yin, L. Zhang, D. Xiang, and R. Gao, "Metal oxide gas sensors: Sensitivity and influencing factors," Sensors **10**(3), 2088–2106 (2010).
[12] J. Rombach, A. Papadogianni, M. Mischo, V. Cimalla, L. Kirste, O. Ambacher, T. Berthold, S. Krischok, M. Himmerlich, S. Selve, and O. Bierwagen, "The role of surface electron accumulation and bulk doping for gas-sensing explored with single-crystalline In_2O_3 thin films," Sens. Actuators, B **236**, 909–916 (2016).
[13] M. Bender, N. Katsarakis, E. Gagaoudakis, E. Hourdakis, E. Douloufakis, V. Cimalla, and G. Kiriakidis, "Dependence of the photoreduction and oxidation behavior of indium oxide films on substrate temperature and film thickness," J. Appl. Phys. **90**(10), 5382–5387 (2001).
[14] T. Berthold, J. Rombach, T. Stauden, V. Polyakov, V. Cimalla, S. Krischok, O. Bierwagen, and M. Himmerlich, "Consequences of plasma oxidation and vacuum annealing on the chemical properties and electron accumulation of In_2O_3 surfaces," J. Appl. Phys. **120**(24), 245301 (2016).
[15] M. Batzill and U. Diebold, "The surface and materials science of tin oxide," Prog. Surf. Sci. **79**(2–4), 47–154 (2005).
[16] J. Borgersen, L. Vines, Y. K. Frodason, A. Kuznetsov, H. von Wenckstern, M. Grundmann, M. Allen, J. Zúñiga-Pérez, and K. M. Johansen, "Experimental exploration of the amphoteric defect model by cryogenic ion irradiation of a range of wide band gap oxide materials," J. Phys.: Condens. Matter **32**, 415704 (2020).

[17]J. Borgersen, K. M. Johansen, L. Vines, H. von Wenckstern, M. Grundmann, and A. Y. Kuznetsov, "Fermi level controlled point defect balance in ion irradiated indium oxide," J. Appl. Phys. **130**, 085703 (2021).
[18]A. Schleife, F. Fuchs, C. Rödl, J. Furthmüller, and F. Bechstedt, "Branch-point energies and band discontinuities of III-nitrides and III-/II-oxides from quasiparticle band-structure calculations," Appl. Phys. Lett. **94**, 012104 (2009).
[19]I. Chatratin, F. P. Sabino, P. Reunchan, S. Limpijumnong, J. B. Varley, C. G. Van de Walle, and A. Janotti, "Role of point defects in the electrical and optical properties of In_2O_3," Phys. Rev. Mater. **3**, 074604 (2019).

Paper IV

Effect of the Ga concentration on the defect concentration dependent resistivity in ion irradiated $(InGa)_2O_3$ alloys